Radiation Damage in Proton - Irradiated Epitaxial Silicon Detectors

Physikalische Diplomarbeit
von

Jörn Lange

Universität Hamburg
Institut für Experimentalphysik
Gruppe Teilchenphysik und Detektorentwicklung

Oktober 2008

Radiation Damage in Proton-Irradiated Epitaxial Silicon Detectors
-
Strahlenschäden in Protonen-bestrahlten epitaktischen Siliziumdetektoren

Physikalische Diplomarbeit
eingereicht von

Jörn Lange

Matrikelnummer: 5573320

Universität Hamburg
Fachbereich Physik
Institut für Experimentalphysik

Erstgutachter: Prof. Dr. Robert Klanner
Zweitgutachterin: Prof. Dr. Caren Hagner

Abstract

In this work radiation hardness of $75\mu m$, $100\mu m$ and $150\mu m$ thick epitaxial silicon pad diodes of both standard and oxygenated material was investigated. Damage after $24GeV/c$ proton irradiation in a $1MeV$ neutron equivalent fluence range between $10^{14}cm^{-2}$ and $10^{16}cm^{-2}$ was studied and isothermal annealing experiments at 80°C were carried out. Standard CV/IV measurements could be performed up to $4\times10^{15}cm^{-2}$. The volume-normalised reverse current was found to increase linearly with fluence with a slope independent of the thickness and impurity concentration. However, due to large fluctuations the fluences had to be renormalised using the current-related damage parameter α. Concerning the depletion voltage, nearly all materials remained at a moderate level up to $4 \times 10^{15}cm^{-2}$. During short-term annealing acceptors annealed out, whereas others were introduced during the long-term annealing. The stable damage was characterised by donor removal at low fluences and fluence-proportional predominant donor introduction for highly irradiated diodes, depending on the oxygen level. No type inversion was observed. Time-resolved measurements with a new $670nm$ laser-TCT setup made the determination of the trapping time constant with the charge correction method possible. The results agreed with expectations and showed a linear increase of trapping probability with fluence. The electric field exhibited a double peak structure in highly irradiated diodes. Charge collection efficiency measurements with α-particles were independent of oxygen concentration, but showed an improved efficiency for thinner diodes. A comparison to simulation revealed systematic discrepancies. A non-constant trapping time parameter was proposed as possible solution.

Zusammenfassung

Im Rahmen dieser Diplomarbeit wurde die Strahlenhärte von $75\mu m$, $100\mu m$ und $150\mu m$ dicken epitaktischen Silizium Pad-Dioden untersucht, wobei sowohl Standard- als auch sauerstoffangereichertes Material zur Verfügung stand. Dabei standen Schäden nach $24GeV/c$ Protonenbestrahlung in einem $1MeV$ Neutronen äquivalentem Fluenzbereich von $10^{14}cm^{-2}$ bis $10^{16}cm^{-2}$ im Mittelpunkt. Isothermale Ausheilexperimente bei 80°C wurden durchgeführt. Standard-CV/IV-Messungen konnten bis $4 \times 10^{15}cm^{-2}$ gemacht werden. Der auf das Detektorvolumen normierte Sperrstrom zeigte eine lineare Abhängigkeit von der Fluenz mit der gleichen Steigung für alle Dicken und Sauerstoffkonzentrationen. Auf Grund von großen Abweichungen einzelner Messpunkte mussten die Fluenzen mit Hilfe des Sperrstrom-Schadensparameters α neu normiert werden. Alle Materialien zeigten nur einen moderaten Anstieg der Verarmungsspannung bis $4 \times 10^{15}cm^{-2}$. Das kurzzeitige Ausheilverhalten war dominiert durch einen Akzeptorrückgang, während die langzeitige Komponente durch Akzeptorerzeugung geprägt war. Die konstante Schädigung zeigte eine Abnahme der ursprünglichen Dotierungskonzentration (*Donor Removal*) bei kleinen Fluenzen und war bei hochbestrahlten Dioden dominiert durch Fluenz-proportionale Donatorerzeugung, die von der Sauerstoffkonzentration abhing. Ein neuer TCT-Aufbau mit einem $670nm$ Laser ermöglichte zeitaufgelöste Signalmessungen, auf die die Ladungskorrekturmethode zur Bestimmung der effektiven Ladungseinfangzeit angewandt werden konnte. Die Ergebnisse zeigten wie erwartet einen Fluenz-proportionalen Anstieg der Ladungseinfangwahrscheinlichkeit. Die elektrische Feldverteilung wies zwei Maxima bei hochbestrahlten Dioden auf. Mit α-Teilchen wurde die Ladungssammlungseffizienz gemessen, die sich als unabhängig von der Sauerstoffkonzentration erwies, aber größer für dünnere Detektoren war. Im Vergleich mit Simulationen zeigten sich systematische Abweichungen, die mit einem nicht-konstanten Einfangzeit-Parameter erklärt werden könnten.

Contents

1 Introduction **1**

2 Basics of Silicon Detectors **4**

2.1 Overview 4

2.2 Electrical Properties of Silicon Diodes 5

2.2.1 Intrinsic and Extrinsic Semiconductors 5

2.2.2 p-n Junction 5

2.2.3 Capacitance 8

2.2.4 Reverse Current 8

2.2.5 Signal Formation and Charge Collection 9

2.3 Silicon Crystal Production Methods 11

2.3.1 Czochralski Material 11

2.3.2 Float Zone Material 11

2.3.3 Epitaxial Material 12

3 Defects in Silicon and Radiation Damage **13**

3.1 Damage Mechanism 13

3.2 Comparing Different Radiation Types - NIEL Hypothesis 14

3.3 Classification of Defects 16

3.3.1 Clusters 16

3.3.2 Point Defects 16

3.4 Influence of the Defects on Detector Properties 16

3.4.1 Overview on Identified Point Defects in Si 19

3.5 Defect Annealing 20

3.5.1 Defect Kinetics 20

3.6 Improving Radiation Hardness 22

3.6.1 Choice of Material - Defect Engineering 22

3.6.2 Thin Detectors - Device Engineering 23

4 Material and Experimental Methods **24**
4.1 Diode Samples 24
4.1.1 Material 24
4.1.2 Devices 25
4.2 Irradiation 26
4.3 Annealing Experiments 26
4.4 CV and IV Measurements 27
4.5 Transient Current Technique 30
4.5.1 TCT with α-Particles 31
4.5.2 TCT with a 670nm Laser 33

5 Experimental Results **38**
5.1 CV and IV Characteristics 38
5.2 Reverse Current 39
5.2.1 Fluence Dependence of the Reverse Current 39
5.2.2 Annealing Behaviour 41
5.3 Development of U_{dep} and N_{eff} 45
5.3.1 Overview 45
5.3.2 ΔN_{eff} at 8min - Stable Damage 48
5.3.3 Full Annealing Analysis according to the Hamburg Model for $75\mu m$ Diodes 51
5.3.4 Consequences for Radiation Hardness 55
5.4 TCT Results 58
5.4.1 Time-Resolved Current Signals with $670nm$ Laser-TCT 58
5.4.2 CCE Measurements with α-TCT 65
5.4.3 Simulation of Charge Collection 68

6 Summary and Conclusions **75**

A Investigated Detectors **79**

List of Figures **81**

List of Tables **83**

Bibiliography **84**

Chapter 1

Introduction

After more than two decades of preparation, these days witness the startup of the *Large Hadron Collider (LHC)* at the European Laboratory for Particle Physics CERN in Geneva. Its scientific aim is the investigation of the microscopic structure of matter and its interactions. By studying nature at the smallest and most fundamental scales, it is also hoped to gain a deeper understanding of the largest structure, namely the universe. Particle collisions at high energies are capable of simulating the conditions shortly after the big bang. Up to now, the *standard model* of particle physics describes all experimental data very accurately. However, there is a missing link in the theory, which is the outstanding discovery of the Higgs boson that is vital for endowing particles with mass. Moreover, there is a number of further open questions that cannot be explained by the standard model, e.g. dark matter and energy, matter-antimatter asymmetry or the nature of gravity. Possible extensions of the standard model include supersymmetry and extra-dimensions.

In order to tackle these questions, collisions at unprecedented energies are necessary. The LHC will provide proton-proton interactions at a centre-of-mass energy of $14TeV$ with $25ns$ bunch-crossing time. As many of the most interesting physics reactions are expected to be very rare, a high luminosity of $10^{34}cm^{-2}s^{-1}$ is envisaged.

The collision reactions will be studied by several experiments, among which *CMS*[1] and *ATLAS*[2] are two general-purpose detectors. Besides hadronic and electromagnetic calorimeters and a muon system, the tracker is one of the most important detector components. Its task is to trace the tracks of traversing charged particles in a magnetic field with high precision in order to determine their momentum, charge and possible displaced vertices accurately. The latter topic is especially important for the identification of short-lived particles that decay only micrometres away from the primary collision vertex such as τ and b-containing particles (also known as τ and *b tagging*). This is of special concern as such particles can be signatures for interesting decay channels of already known particles on the one hand and for the discovery of new particles on the other hand.

Position-sensitive silicon detectors meet all the requirements for high-performance tracking and are widely used in present-day experiments. Due to their fine segmentation a position resolution of a few micrometres can be achieved, as well as a good two-particle separation. A fast signal response in the order of $10ns$ can cope with the short bunch-crossing time. A low ionisation energy enables a high signal-to-noise ratio also for thicknesses of typically $300\mu m$,

[1] Compact Muon Solenoid.
[2] A Toroidal Lhc ApparatuS.

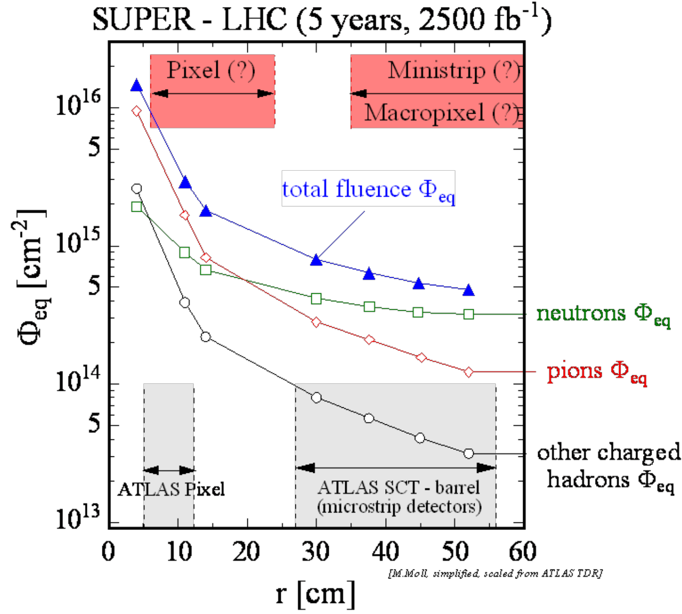

Figure 1.1: Simulation of equivalent fluences for the different radiation types as a function of distance to the beam line after 5 years of SLHC operation at a luminosity of $10^{35}cm^{-2}s^{-1}$ [Lin06c].

which represents a radiation length of only about 0.3%, thereby reducing the material budget. Another advantage is the large-scale availability at relatively low cost due to industrial mass market production. This enabled the use of an all-silicon tracker for CMS with a total silicon area of $205m^2$.

However, due to a high event rate, the radiation environment is very hostile, especially for the innermost pixel layer very close to the beam line. Irradiation can cause dislocations of silicon atoms, resulting in lattice distortions and the formation of complex defects with other impurities. This gives rise to the introduction of defect levels in the energy band gap. Their effects on the macroscopic detector performance are an increased leakage current, a change in depletion voltage and trapping of signal charge carriers leading to a degradation of charge collection efficiency. To conclude, the signal-to-noise ratio declines dramatically.

At a radius of $r = 4cm$ a $1MeV$ neutron equivalent fluence of $\Phi_{eq} = 3 \times 10^{14}cm^{-2}$ is expected for the envisaged 10 years operation. Already this has pushed the present day silicon tracking detectors to the very edge of the current technology, the pixel detectors are even planned to be exchanged after 5 years. However, the planned *Super-LHC (SLHC)* luminosity upgrade by a factor of 10 to $10^{35}cm^{-2}s^{-1}$ leads to even higher radiation levels of up to $\Phi_{eq} = 1.6 \times 10^{16}cm^{-2}$ at $r = 4cm$ during 5 years operation (see Fig. 1.1) [Gia02]. In order to tackle this unprecedented challenge of developing radiation hard semiconductor detectors capable of withstanding such levels, the CERN-RD50 research programme *Development of Radiation Hard Semiconductor Devices for Very High Luminosity Colliders* was initiated in 2002 [RD50], in the frame of which this work was carried out.

There are different approaches of how to improve the radiation tolerance of silicon [Fre05]. One of them is called *defect engineering*, i.e. the deliberate tailoring of impurity concentrations during crystal growth and processing. For example it was found that an enhanced oxygen

concentration in float zone silicon reduces the increase of the depletion voltage at high fluences substantially, but there was no success so far in lowering the leakage current and trapping. Another approach is *device engineering* that mainly focuses on the geometry of the detector and its electrodes. One example is the development of thin detectors. This has the potential to decrease the leakage current which is proportional to the thickness, the depletion voltage that is even proportional to the squared thickness, and the trapping because the drift distance is smaller and the electric field higher. However, a reduction of the thickness means also a loss in the originally deposited charge so that an optimum thickness has to be determined carefully.

In this work, the radiation damage in epitaxial silicon detectors was investigated, which can be regarded as a combined approach of both defect engineering and device engineering. On the one hand epitaxial silicon naturally exhibits a higher oxygen concentration, which can be even further enhanced by additional oxygen enrichment during processing. On the other hand, epitaxial layers can be grown very thin. Here, medium thick epitaxial silicon diodes of $75\mu m$, $100\mu m$ and $150\mu m$ of both standard and oxygenated material were studied. The development of the leakage current and the depletion voltage was investigated with the CV/IV method as a function of fluence, annealing time, thickness and impurity concentration. Special emphasis was laid on the study of trapping effects and charge collection efficiency with TCT[3] because this issue might be the ultimate limit for the application of silicon detectors in high energy physics experiments. The measurements were performed after irradiation with $24 GeV/c$ protons because charged hadrons like pions, which behave similarly, constitute the dominant contribution in the regions with highest radiation levels (see Fig. 1.1).

In the first part of this work, an overview on the basics of silicon detectors (Chapter 2) and radiation damage in silicon (Chapter 3) will be given. Subsequently, the material and the experimental methods will be explained in detail in Chapter 4. A presentation and discussion of the experimental results obtained with the CV/IV method and TCT follows in Chapter 5, before a summary with some conclusions will be finally given in Chapter 6.

[3]Transient Current Technique.

Chapter 2

Basics of Silicon Detectors

2.1 Overview

Semiconductor detectors are basically solid state ionisation chambers as illustrated in Fig. 2.1. An incident particle liberates e-h pairs[1] inside the semiconductor bulk. The average number of e-h pairs is the absorbed energy E_{abs} divided by the mean ionisation energy E_i. The charge carriers move under the influence of an applied electric field to the respective electrodes and induce a measurable current in the external electrical circuit.

In energy spectroscopy measurements, the particle is stopped inside the detector so that the signal is proportional to its initial energy. In high energy tracking experiments, the particle traverses a detector with finely segmented electrodes (strip or pixel detectors), which yields a high resolution position information ($\approx 10\mu m$). Multiple layers of detectors make a track reconstruction possible, which can be used for momentum and charge analysis of the traversing particle.

Compared to other detectors like gas ionisation chambers, the advantages of semiconductors are the low ionisation energy ($3.6eV$ for Si, $>30eV$ for gas) and the large density, which result in a high number of created charge carriers per traversed distance (≈ 100 e-h pairs/μm in Si for a mip[2]). Thus only a small thickness ($d \approx 100\mu m$) is required for a sufficiently large signal. This and the large mobility of charge carriers in semiconductors lead to short charge collection times ($t_C \approx 1 - 10ns$) and consequently to a fast readout.

Silicon (Si) in particular is a very suitable material and is widely used in semiconductor industries so that the detector manufacturers can profit from the highly developed technologies and the great experience gained from mass market production. This ensures also low costs of Si detectors compared to competing semiconductor materials.

One of the most important parameters for the detector performance is the signal-to-noise ratio (SNR). It should be as large as possible and must exceed a specific limit under which the detection of a particle is not guaranteed anymore. The signal is mainly determined by the thickness of the sensitive detector region and the charge collection efficiency (CCE) of the detector. For minimising the noise, a low capacitance and low quiescent detector current are required.

However, the resistivity of commercially available Si material is limited to $\approx 15k\Omega cm$,

[1] Electron-Hole pairs.

[2] Minimum Ionising Particle.

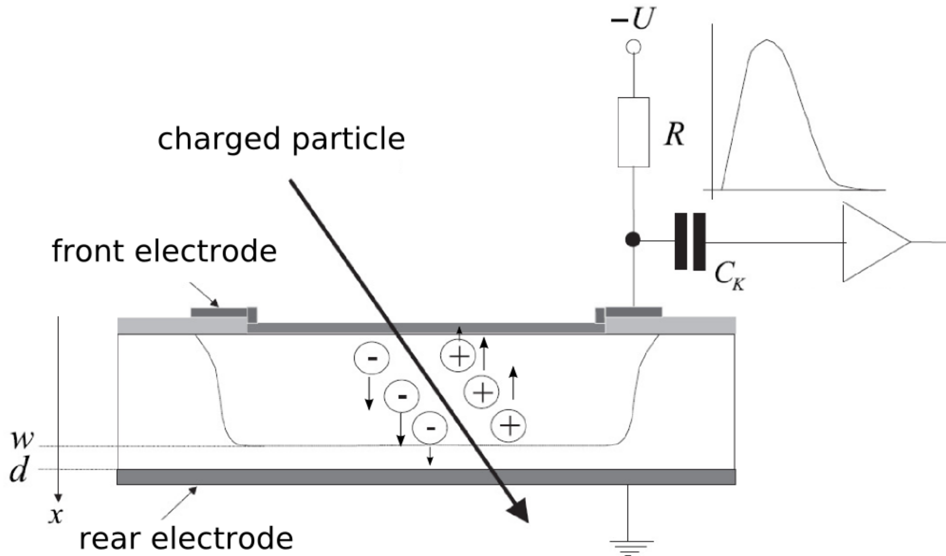

Figure 2.1: Principle of a semiconductor detector.

which would lead to a much too high detector current. The solution is to use Si diode structures with large sensitive detector regions depleted from free charge carriers. This is established by a reverse-biased p-n junction.

2.2 Electrical Properties of Silicon Diodes

2.2.1 Intrinsic and Extrinsic Semiconductors

Semiconductors are characterised by their forbidden energy gap between valence band and conduction band ($E_g = 1.12eV$ for Si). In intrinsic Si, only few electrons are thermally excited from the valence into the conduction band at room temperature so that there are only few free charge carriers. The big benefit of semiconductors is the possibility of tailoring the conductivity by deliberately introducing impurities into the Si lattice. This procedure is called doping. If a Si atom is replaced by a so-called shallow donor with five valence electrons such as phosphorus (P) or antimony (Sb), four of these will form the covalent bonding with the neighbouring Si atoms. The remaining electron is only loosely bound ($\approx$ 45 meV ionisation energy for P) so that it can be easily excited into the conduction band at room temperature. In this way, both a positively charged P ion and a free negative charge carrier are created, so the material is called n-type. In a similar manner, material with free positive charge carriers (p-type) can be produced by adding shallow acceptors with only three valence electrons, e.g. boron (B).

2.2.2 p-n Junction

Fig. 2.2 shows a separated p-type and n-type material with their respective energy band diagrams (left-hand side). If these two materials are joined together (right-hand side), there

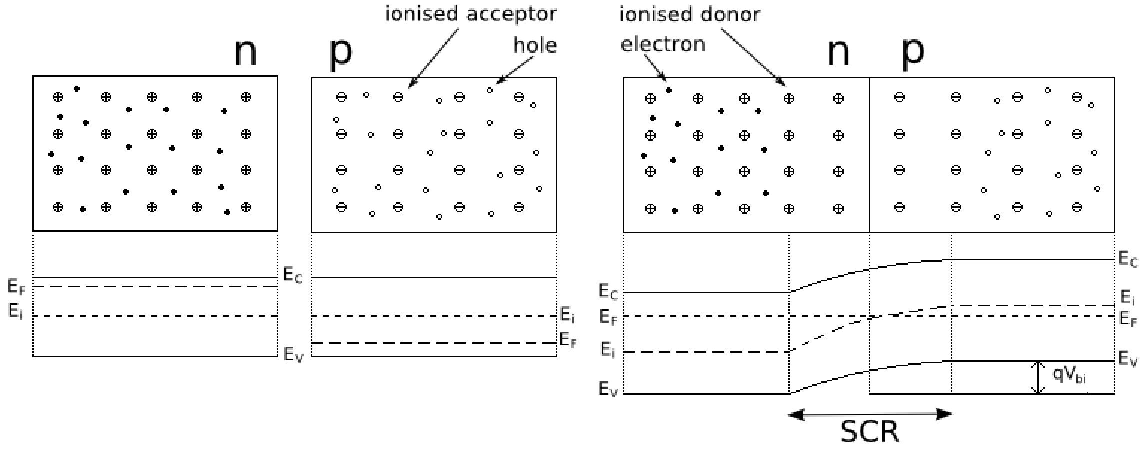

Figure 2.2: Schematic figure of the formation of a p-n junction. Left: An n-type and p-type semiconductor separately with their respective energy band diagrams. Right: The p-n junction with the space charge region (SCR).

will be a charge carrier concentration gradient due to the different doping types. As a result, the free electrons from the n-side in the junction region will diffuse to the p-side and recombine, and vice versa for the holes from the p-side. The non-mobile positively ionised donors, however, are left on the n-side and the negatively-ionised acceptors on the p-side. An electric field builds up which acts against the diffusion. Eventually, an equilibrium between the diffusion current and the drift current is reached. In this way, a bipolar space charge region depleted from free charge carriers is formed around the junction. The potential difference is called built-in voltage U_{bi} and corresponds to the difference between the fermi level on the n-side and the one on the p-side. The electric field strength E and the electric potential Φ can be obtained from solving Poisson's equation. For Si detectors, one usually uses a one-sided abrupt p^+-n junction where the p^+ denotes that the p-side is much more heavily doped than the n-side (see Fig. 2.3 a)). It follows from charge neutrality that in this case, the depleted region of thickness W extends much further into the less heavily doped n-side of the diode. If one assumes the free charge carrier density to be zero and the space charge density ρ_{el} to be homogeneous, Poisson's equation reads

$$-\frac{d^2\Phi(x)}{dx^2} = \frac{\rho_{el}}{\epsilon\epsilon_0} = \frac{q_0 N_{eff}}{\epsilon\epsilon_0}, \tag{2.1}$$

where $N_{eff} = N_D - N_A$ is the effective doping concentration, i.e. the difference between the ionised donor and acceptor concentration in the n-type space charge region, $\epsilon\epsilon_0$ the dielectric constant ($\epsilon = 11.9$ for Si) and q_0 the elementary charge.

By integrating Eq. 2.1 with the boundary condition $E(x = W) = -\frac{d}{dx}\Phi(x = W) = 0$, one obtains an expression for the electric field distribution which develops linearly inside the space charge region from its maximum absolute value at $x = 0$ to 0 at $x = W$ (see Fig. 2.3 b)):

$$E(x) = \frac{q_0 N_{eff}}{\epsilon\epsilon_0}(x - W), \qquad 0 \le x \le W \text{ and } W \le d. \tag{2.2}$$

A second integration with the boundary condition $\Phi(x = W) = 0$ gives a parabolic behaviour of the potential:

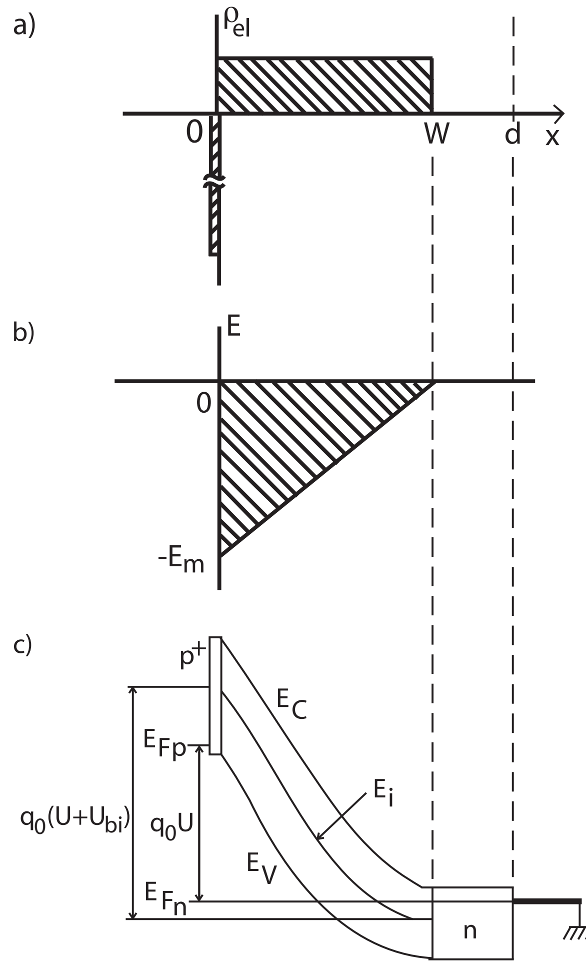

Figure 2.3: Schematic figure of a one-sided abrupt p$^+$-n junction:
a) electric charge density,
b) electric field strength,
c) electron potential energy.

$$\Phi(x) = -\frac{1}{2}\frac{q_0 N_{eff}}{\epsilon\epsilon_0}(x-W)^2, \qquad 0 \leq x \leq W \text{ and } W \leq d. \tag{2.3}$$

Fig. 2.3 c) shows the corresponding electron potential energy $-q_0\Phi$. For no applied external bias voltage, $\Phi(x=0)$ corresponds to U_{bi}. In the case of an applied reverse bias U one has to set $\Phi(x=0) = U_{bi} + U$ so that the width of the space charge region as a function of bias voltage is given by

$$W(U) = \sqrt{\frac{2\epsilon\epsilon_0}{q_0\,|N_{eff}|}(U+U_{bi})}, \qquad W \leq d. \tag{2.4}$$

As one can see, with increasing reverse bias the electric field and the space charge region extend further into the detector until the back contact is reached. The voltage necessary for a full depletion of the whole detector depth is called *depletion voltage* U_{dep}. With the

approximation $U_{dep} >> U_{bi} \approx 0.5V$, which will be always assumed in the following, one gets the following linear relation between U_{dep} and $|N_{eff}|$:

$$U_{dep} = \frac{q_0}{2\epsilon\epsilon_0}|N_{eff}|d^2. \tag{2.5}$$

If the applied voltage is larger than the depletion voltage[3], the part of U which exceeds U_{dep} creates a homogeneous field $E = -\frac{(U-U_{dep})}{d}$ in addition to the field $E(x)|_{W=d}$ from Eq. 2.2:

$$E(x) = \frac{1}{d}\left[U_{dep}\left(\frac{2x}{d} - 1\right) - U\right], \qquad U \geq U_{dep}. \tag{2.6}$$

2.2.3 Capacitance

The *depletion layer capacitance* or *dynamic junction capacitance* C is defined as the incremental change of the depletion layer charge dQ on each side of the junction upon an incremental change of the applied voltage dU:

$$C = \frac{dQ}{dU}. \tag{2.7}$$

For abrupt junctions the space charge Q can be written $Q = q_0|N_{eff}|AW$ where A denotes the effective area of the diode. So its incremental change is given by $dQ = q_0|N_{eff}|AdW$. Together with the derivative of Eq. 2.4, this gives

$$C = \frac{dQ}{dU} = \frac{dQ}{dW}\frac{dW}{dU} = A\sqrt{\frac{\epsilon\epsilon_0 q_0|N_{eff}|}{2U}} = \epsilon\epsilon_0\frac{A}{W(U)}, \qquad U \leq U_{dep}. \tag{2.8}$$

This results in the following capacitance-voltage (CV) characteristic: For $U \leq U_{dep}$, the capacitance decreases as $C \propto 1/\sqrt{U}$. If the applied bias exceeds the depletion voltage, C reaches a constant final value

$$C_{end} = \epsilon\epsilon_0\frac{A}{d}, \tag{2.9}$$

which is also called the *end capacitance* or *geometrical capacitance* since it is only dependent on the detector geometry and not on the voltage. Due to this specific CV characteristic, it is possible to obtain the depletion voltage from the kink in the doubly logarithmic CV plot (see Sec. 4.4).

2.2.4 Reverse Current

The *reverse current* or *leakage current* denotes the current of a reverse-biased diode and is an important parameter as it highly influences the noise and the power consumption of a detector. In an ideal diode, the reverse current is only determined by diffusion of charge carriers from the non-depleted region into the space charge zone (saturation current $I_S \approx pA$). However, in real diodes the dominant contribution comes from charge carriers thermally generated by process- and radiation-induced defects near the middle of the band gap and interface or surface states. In the following, the surface effects are neglected and only the bulk generation current is taken

[3]So-called *overdepletion*.

into account. As it arises only from defects in the space charge region, $I_{bulk} \propto W \propto \sqrt{U}$ for $U \leq U_{dep}$ and it saturates if the applied reverse bias is larger than the depletion voltage. Furthermore, it is determined by the generation life time τ_g whose reciprocal is a measure for the temperature-dependent probability of e-h pair emission. All in all, the reverse current can be written

$$I_{rev} \approx I_{bulk} = \frac{q_0 n_i W(U) A}{\tau_g}, \tag{2.10}$$

where n_i is the intrinsic charge carrier concentration. In order to account for the strong temperature dependence of the reverse current, all current measurements in this work have been normalised to a reference temperature of $T_R = 293.15K$ via

$$I(T_R) = I(T) \cdot \left(\frac{T_R}{T}\right)^2 \exp\left(-\frac{E_g}{2k_B}\left[\frac{1}{T_R} - \frac{1}{T}\right]\right), \tag{2.11}$$

where k_B is Boltzmann's constant [Sze85].

Because of this high temperature dependence, the reverse current can be reduced significantly by cooling. Therefore, the Si detectors at the LHC will be operated around -10°C in order to reduce the power consumption and the noise.

2.2.5 Signal Formation and Charge Collection

As already pointed out in Sec. 2.1, a Si detector works as a solid state ionisation chamber: An ionising particle creates e-h pairs along its path. If an electric field E is applied, the electrons and holes drift with velocity $v_{dr_{e,h}}(E)$ to the positive and negative electrode, respectively. In the case of a simple, non-segmented diode (a so-called *pad detector*), one can assume a one-dimensional approximation because the thickness is much smaller than the lateral extension. According to *Ramo's theorem*[4], the induced current of $N_{e,h}$ electrons or holes due to their drift can be calculated as

$$I_{e,h}(t) = \pm \frac{q_0 N_{e,h}(t)}{d} v_{dr_{e,h}}(t), \tag{2.12}$$

where the upper sign refers to electrons, the lower sign to holes[5].

Drift Velocity

However, the drift velocity is only an implicit function of time. In reality it is a function of the electric field that in turn depends on the position of the charge inside the detector: $v_{dr}\left(E\left(x\left(t\right)\right)\right)$. Hence, the trajectory $x(t)$ of the particle must be known, which can be obtained via the solution of its inverse $t(x)$:

$$v_{dr} = \frac{dx}{dt} \qquad \Rightarrow \qquad t(x) = \int_{x_0}^{x} \frac{1}{v_{dr}\left(E\left(x'\right)\right)} dx', \tag{2.13}$$

[4] Ramo's theorem describes in general, i.e. for an arbitrary electrode configuration, the current induced on the ith electrode as $I_i(t) = q_0 \vec{v}_{dr}(\vec{E}(\vec{r}(t))) \cdot \vec{E}_{i,w}(\vec{r}(t))$ where $\vec{E}(\vec{r}(t))$ is the electric field at point $\vec{r}$ and $\vec{E}_{i,w}(\vec{r}(t))$ the so-called weighting field of the ith electrode at the same point (for more details see [Spi05]).

[5] As both their respective charge and drift velocity signs are opposite, the electric currents of electrons and holes have the same direction.

with x_0 being the the position where the charge carrier has been created. The charge collection time after which electrons and holes reach their respective electrode is obtained by $t_{C_e} = t(d)$ and $t_{C_h} = t(0)$, respectively.

The drift velocity is due to different scattering mechanisms (impurities, phonons etc.) a non-trivial function of the electric field. For low field values it is $v_{dr} = \mu_0 E$, i.e. the velocity depends linearly on the field via the low-field mobility μ_0, whereas for high-field values, the velocity saturates: $v_{dr} = v_{sat} = const.$ A parameterisation of this behaviour is presented in Sec. 5.4.3.

Charge Collection Efficiency

In practice, one is usually not so much interested in the instantaneous current, but rather in the *collected charge* Q, i.e. the integrated current:

$$Q = \int_0^{t_{C_e}} I_e(t)dt + \int_0^{t_{C_h}} I_h(t)dt = \int_{x_0}^{d} \frac{q_0 N_e(t(x))}{d} dx + \int_{x_0}^{0} -\frac{q_0 N_h(t(x))}{d} dx. \tag{2.14}$$

After the second equal sign the integration variable dt has been substituted by $\frac{dx}{v_{dr}}$, assuming that all e-h pairs have been created at position x_0 at $t = 0$.

If the number of charge carriers stays constant during the drift, i.e. $N_e(t) = N_h(t) = N_0$, it follows from the above equation that the collected charge is the same as the deposited one: $Q = Q_0 = q_0 N_0$.

However, if parts of the charge carriers are trapped by defects during their drift, which can occur especially after strong irradiation (see Sec. 3.4), $N(t)$ is not constant anymore but decreasing. The probability to get trapped is proportional to the traversed path length. So after a distance dl, the loss in the number of charge carriers is given by

$$dN = -N \frac{dl}{\lambda_{eff_{e,h}}}, \tag{2.15}$$

where $\lambda_{eff_{e,h}}$ is the *effective carrier trapping distance.* Under the assumption that the drift velocity is much smaller than the thermal velocity $v_{th_{e,h}}$, the trapping distance $\lambda_{eff_{e,h}}$ can be expressed by an *effective carrier trapping time* $\tau_{eff_{e,h}}$:

$$\begin{array}{rclcl} dl & = & v_{th_{e,h}} dt & \text{if} & v_{dr_{e,h}} << v_{th_{e,h}} \\ \Rightarrow \; dN & = & -N \frac{dt}{\tau_{eff e,h}} & \text{where} & \tau_{eff e,h} = \frac{\lambda_{eff_{e,h}}}{v_{th_{e,h}}}. \end{array} \tag{2.16}$$

If τ_{eff} is constant the solution of the last differential equation reads

$$N(t) = N_0 \exp\left(-\frac{t}{\tau_{eff_{e,h}}}\right). \tag{2.17}$$

The loss of charge carriers during their drift modifies the induced current so that the collected charge decreases. The ratio between collected charge Q and deposited charge Q_0 is called the *charge collection efficiency (CCE)*:

$$CCE = \frac{Q}{Q_0}. \tag{2.18}$$

The CCE is 1 for no trapping, e.g. in the case of an unirradiated detector, and decreases the more trapping occurs.

2.3 Silicon Crystal Production Methods

There are three main growing techniques of Si, which will be explained in the following: the *Czochralski (Cz)*, *Float Zone (FZ)* and *epitaxial (EPI)* process [Sze85]. Special emphasis is laid on the different amounts of process-induced impurities, especially oxygen, as they play a decisive role in the creation of radiation damage, as shown in the next chapter.

2.3.1 Czochralski Material

The Czochralski method begins with polysilicon that is melted in a rotating quartz crucible. A monocrystalline seed crystal is placed on the surface and slowly drawn upwards while being rotated. At the interface between crystal and melt, the Si solidifies in a single crystal with the same crystal orientation as the seed. By varying the draw speed and temperature the diameter is controlled.

The drawback of the Czochralski method is the high amount of impurities, especially O, C, P, B and Al. During the process, molecules from the crucible and the graphite susceptor dissolve into the melt and lead to an enrichment of the Si with impurities. For a long time it was impossible to produce detector grade Cz Si with resistivities $> 100\Omega cm$. However, this is now achieved by applying a magnetic field in vertical or horizontal direction. This can improve the situation by preventing convection and thus avoiding a mixing of the dirty melt near the crucible with the purer Si in the centre. This method is called *magnetic Czochralski (MCz)*. But the concentrations of impurities are still high compared to other materials ($[O] \approx (7-8) \times 10^{17} cm^{-3}$, $[C] \leq 2 \times 10^{16} cm^{-3}$ [Mol99]). A certain fraction of the oxygen exists not as a single atom O but as a dimer O_2.

However, especially the high concentration of oxygen can be also advantageous due to the *oxygen effect* (see Sec. 3.6.1). Moreover, MCz material is available at low cost and widely used in microelectronics.

2.3.2 Float Zone Material

The float zone method is based on the zone-melting principle and takes place either under vacuum or in an inert gaseous atmosphere. A high-purity polycristalline rod and a single crystal seed are brought into close contact in a vertical position and rotated. With a radio frequency field the region around the contact is melted (*floating zone*). Slowly the melted zone is shifted away from the contact so that the Si can solidify gradually in a single crystal from the seed as a starting point.

Contrary to the Cz method, there is no contact to other materials than ambient gas so that a higher purity and consequently resistivity is achieved ($[O] \approx 10^{16} cm^{-3}$, $[C] \approx 5 \times 10^{15} cm^{-3}$).

However, as it turned out that a high oxygen concentration is beneficial in terms of radiation hardness, a deliberate adding of oxygen to standard float zone material *(STFZ)* is

preferred. This oxygen enrichment can be done by a diffusion process at 1150°C that lasts between 24h and 72h, resulting in an oxygen concentration up to a level of $10^{17}cm^{-3}$. This material is called *diffusion oxygenated float zone (DOFZ)* and is one of the best examples of defect engineering (see Sec. 3.6.1).

2.3.3 Epitaxial Material

As epitaxial Si detectors are the main subject of this work, they will be explained in detail. Epitaxy denotes the growing of a thin layer on a single crystal substrate. The epitaxial layer adopts the crystal orientation of the substrate and is therefore also monocrystalline. If the layer and the substrate are of the same semiconductor material, it is called homoepitaxy, if they are different the process is called heteroepitaxy.

There are different epitaxial growing methods, but the most relevant with respect to detector grade Si is the *vapour phase epitaxy (VPE)*, sometimes also called *chemical vapour deposition (CVD)*, that has also been used by the manufacturer ITME [ITME] for the material in this work. At temperatures around 1200°C Si is obtained by decomposition of a gaseous compound (most commonly *silicon tetrachloride* $SiCl_4$) with the help of hydrogen and arranges itself on the crystal substrate:

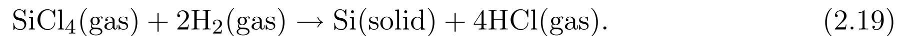

$$\mathrm{SiCl_4(gas) + 2H_2(gas) \rightarrow Si(solid) + 4HCl(gas).} \quad (2.19)$$

As there are also competing reactions with $SiCl_4$ that etch the Si away, the growth rate is reduced and the $SiCl_4$ concentration has to be chosen carefully. A typical growth rate is approximately $1\mu m/min$. The doping of the layer is done by introducing gaseous compounds such as diborane (B_2H_6) or phosphine (PH_3) for p-type and n-type material, respectively.

As a substrate, usually highly-doped Cz material is chosen for the following reasons: The high doping guarantees a low resistivity so that the serial resistance of the substrate can be neglected and the sensitive region is determined by the epitaxial layer alone. During the crystal growth impurities can out-diffuse from the substrate into the EPI layer. While the diffusion of unwanted impurities remains on a moderate level, especially oxygen (O and also a large amount of O_2) with its high diffusion constant is introduced in the layer in a high concentration as Cz material is very oxygen-rich. So naturally, the oxygen concentration of EPI material is higher than the one of STFZ. However, the distribution of oxygen is very inhomogeneous throughout the layer (see Fig. 4.1). In order to improve the homogeneity and to increase the average oxygen density, oxygenation can be performed also for epitaxial material in a similar way as for FZ: The diffusion of oxygen from the Cz substrate on the one side and from the SiO_2 at the surface on the other side is stimulated at about 1100°C, thereby transforming *standard epitaxial material (EPI-ST)* into *diffusion oxygenated epitaxial material (EPI-DO)*.

Chapter 3

Defects in Silicon and Radiation Damage

In the last section, the macroscopic parameters that determine the detector performance like capacitance, depletion voltage, reverse current and charge collection efficiency were introduced. Energy levels in the forbidden band gap arising from microscopic defects like impurities or lattice distortions can have large effects on those macroscopic parameters. Some of the defects are inherent as even today's purest Si contains a considerable amount of impurities like e.g. oxygen or carbon, which is sometimes even desired as in the case of gettering or deliberate doping with phosphorus and boron. Normally, this can be well controlled and many of the defects are not even electrically active. However, in the case of the application in high luminosity colliders as the LHC, radiation damage can occur, i.e. the introduction of new defects which pose a considerable threat on the detector performance.

Radiation damage can be divided into surface and bulk damage. As the latter one is the limiting factor for the use of Si detectors close to the interaction point in colliders, this work focuses on bulk damage.

3.1 Damage Mechanism

The interaction of hadronic and higher energetic leptonic particles with the Si lattice atoms can cause such a high energy transfer from the incoming particle to a so-called *primary knock on atom (PKA)* that the latter one can be displaced from its lattice site. For an incoming particle of energy E and mass m, the maximal transferable energy can be calculated in a nonrelativistic approach as

$$E_R^{max} = 4E\frac{m \cdot m_{Si}}{(m + m_{Si})^2}, \tag{3.1}$$

where m_{Si} is the mass of a Si atom. The minimum energy that needs to be imparted to the PKA in order to cause a displacement is $E_d \approx 25eV$ [Lin80]. In this way a Si interstitial (I) and a left-over vacancy (V) are created (*Frenkel pair*). If the recoil energy of the PKA is large enough, it can knock out further Si atoms and thus create cascades of defects as illustrated in Fig. 3.1. At the end of the path of a heavy recoil atom, the cross section for elastic scattering increases as the velocity decreases, resulting in a dense agglomeration of defects (*clusters*). The threshold recoil energy required for cluster generation is approximately $5keV$.

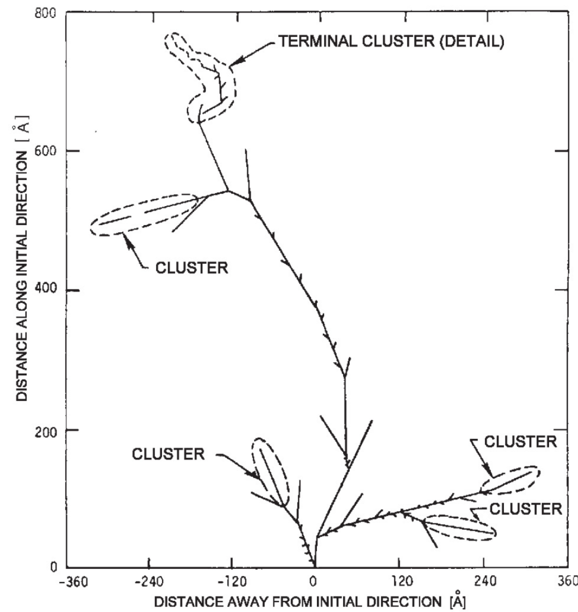

Figure 3.1: Monte Carlo simulation of a cascade caused by a recoil atom with a primary energy of $E_R = 50keV$. This energy corresponds to the average kinetic energy that a $1MeV$ neutron transfers to a PKA [Lin80].

The damage process, however, continues as the Si interstitials and vacancies are highly mobile at temperatures above $150K$. On the one hand, damage is reduced as a large fraction of the produced Frenkel pairs recombine, e.g. approximately 60% of the overall produced pairs and even $75 - 95\%$ in cluster regions [Shi90]. On the other hand, the remaining interstitials and vacancies migrate through the lattice and many of them perform further reactions both with each other and with impurities in the Si crystal. In this way, defects are formed that constitute the real radiation damage because many of them are electrically active and therefore responsible for altering the macroscopic detector parameters.

3.2 Comparing Different Radiation Types - NIEL Hypothesis

The question arises how the damage effects of irradiation with different particle types and energies can be compared. This is a difficult task because depending on the irradiation type and energy, there are different interactions with the Si atoms. Charged hadrons interact primarily via ionisation which is a fully reversible process in the Si bulk[1]. The part of the interaction that does result in displacement damage in the lattice is called *non-ionising energy loss (NIEL)*. For low energetic protons (e.g. $10MeV$), this is mostly due to Coulomb interactions which impart the energy in small fractions so that mainly point defects are created. On the contrary, neutrons as non-charged particles interact only with the nucleus via elastic scattering and above $1.8MeV$ also via nuclear reactions [Lin80]. The damage after neutron irradiation is dominated by cluster effects. High energetic protons, e.g. the $24GeV/c$ protons used in this work, cause both point defects and cluster damage.

The NIEL hypothesis assumes that any displacement-damage induced change in the mate-

[1]However, ionisation can cause radiation-induced surface damage, but this is not considered in this work.

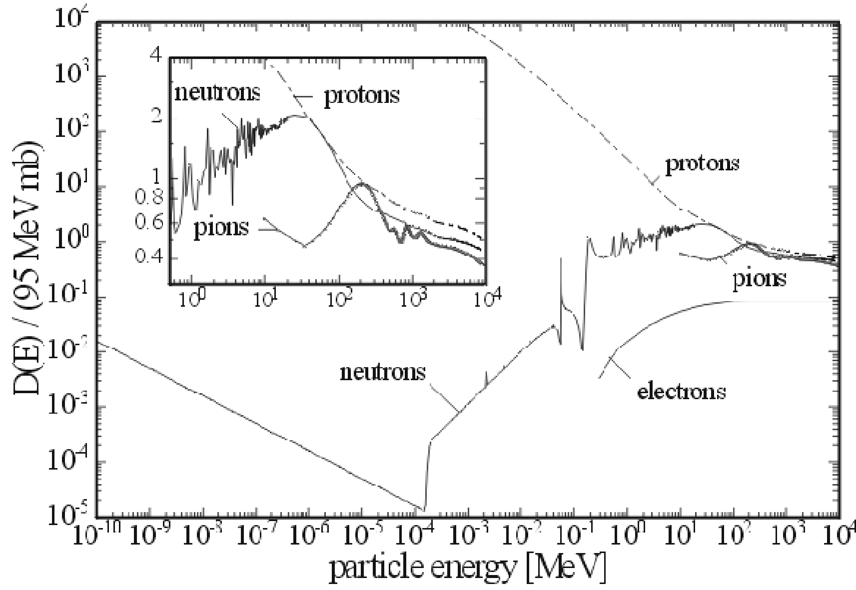

Figure 3.2: Displacement energy cross section for different particle types as a function of energy, normalised to $1MeV$ neutrons [Mol99].

rial properties scales with the energy imparted in displacing collisions. This can be expressed by the *displacement damage cross section* or *damage function*

$$D(E) = \sum_{\nu} \sigma_{\nu}(E) \cdot \int_{E_d}^{E_R^{max}} f_{\nu}(E, E_R) P(E_R) dE_R. \tag{3.2}$$

The index ν runs over all possible reactions with cross section σ_{ν} between the impinging particle of energy E and the Si atoms, which can lead to displacements in the lattice. $f_{\nu}(E, E_R)$ is the probability for the generation of a PKA with recoil energy E_R by a particle with energy E in the reaction with index ν. The so-called Lindhard partition function $P(E_R)$ gives the portion of energy available for displacement damage by a PKA with recoil energy E_R and can be calculated analytically [Laz87]. The integration is done over all possible recoil energies ranging from the displacement threshold E_d to the maximum transferable energy E_R^{max}. With the help of $D(E)$ it is now possible to compare the displacement damage for different particle types and energies as shown in Fig. 3.2.

As one is usually dealing with different irradiation sources with continuous energy spectra $\Phi(E)$, it is convenient to define a so-called *hardness factor* κ that integrates $D(E)$ over the energy spectrum and scales it to the equivalent displacement damage cross section of mono-energetic $1MeV$ neutrons:

$$\kappa = \frac{\int D(E)\Phi(E)dE}{D(E_n = 1MeV) \cdot \int \Phi(E)dE}. \tag{3.3}$$

Hence it is possible to calculate the *equivalent* $1MeV$ *neutron fluence*[2], i.e. the fluence of $1MeV$ neutrons which would have created the same displacement damage, as

[2]In the following simply referred to as *equivalent fluence*.

$$\Phi_{eq} = \kappa\Phi = \kappa \int \Phi(E)dE. \tag{3.4}$$

3.3 Classification of Defects

3.3.1 Clusters

As already noted, clusters are regions with a high defect density which emerge after fast hadron irradiation. They are able to change the local band structure in the cluster region. The exact nature of the defects inside a cluster are still not very well known and therefore neither their electrical properties. According to the model proposed by Gossick [Gos59] a large number of Frenkel pairs is produced in the cluster region by a PKA. Due to their higher mobility, the Si interstitials diffuse fast out of this region, leaving a conglomeration of vacancies that form higher-order complex defects such as V_2, V_3 etc. Those are stable at room temperature and constitute the core of the cluster with a radius of $r_1 \approx 5 - 15nm$. The out-diffusing interstitials interact with impurities so that a kind of shell with complex defects and a radius of $r_2 \approx 100nm$ develops around the core. According to [Smi83] the defects in the cluster shell act as recombination and generation centres.

3.3.2 Point Defects

As already described in Sec. 3.1, the primary defects, i.e. interstitials and vacancies, are mobile and react with each other or with impurities in the Si lattice, thus creating secondary defects or complex defects. Fig. 3.3 shows an overview on possible defect configurations. Vacancies, interstitials and complex defects are denoted as point defects. Some of them may have discrete energy levels E_t in the Si band gap and therefore be electrically active, whereas others are not.

The defect states can be acceptor- or donor-like. Acceptors are negatively charged if occupied by an electron and neutral otherwise, whereas donors are neutral if occupied by an electron and positively charged if not occupied. Defects also can have more than one energy level in the band gap and there are even some which have both an acceptor and a donor state, being called amphoteric. Whether the states are occupied or not is determined in thermal equilibrium by the relative position of the energy level compared to the Fermi level E_F[3].

The defects can be divided in shallow and deep levels. Lacking an exact definition, defects are commonly called shallow if they are close to one of the band edges so that they are ionised at room temperature, e.g. the dopants P and B. Deep defects are closer to the middle of the band gap.

3.4 Influence of the Defects on Detector Properties

The effect of defects with energy levels in the band gap on the electrical properties of a semiconductor are shown schematically in Fig. 3.4. The most important mechanisms are the

[3] The Fermi level E_F is the energy level with occupation probability 1/2 in thermal equilibrium. Hence an energy level is more likely to be occupied by an electron if the Fermi level is above it and to be not occupied if $E_F < E_t$.

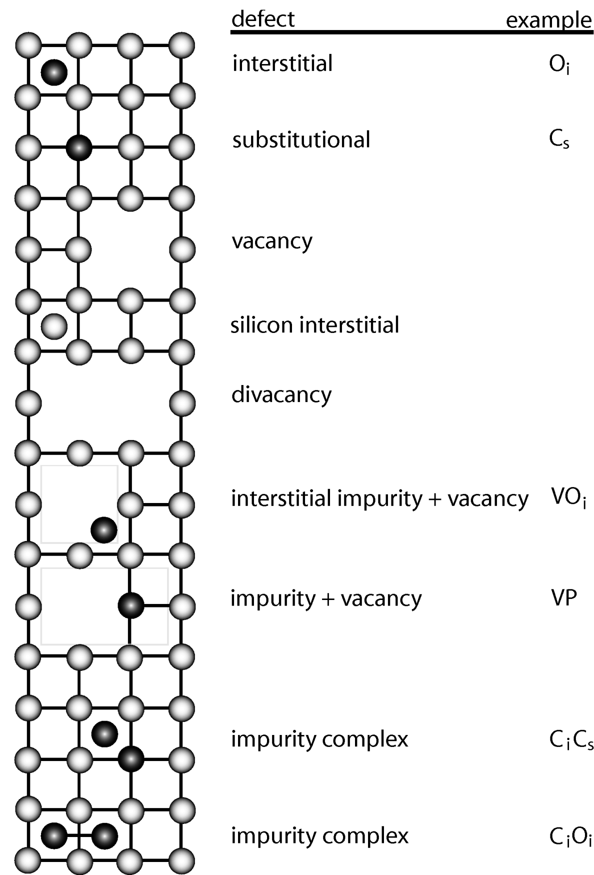

Figure 3.3: Schematic representation of some point defects. The index i stands for *interstitial*, the index s for *substitutional*.

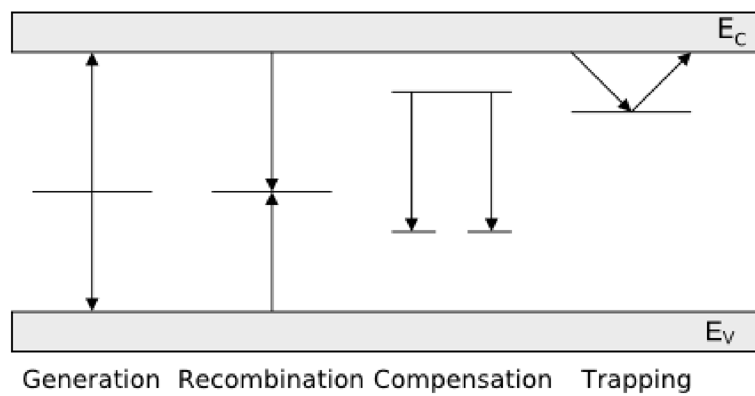

Figure 3.4: Effects of defect levels in the band gap on electrical properties.

following:

- *Generation*
  Defects with energy levels close to the middle of the band gap act as generation centres for e-h pairs.
- *Recombination*
  This is the opposite process of generation and means the simultaneous capture of an electron and a hole, which leads to a reduction of free charge carriers.
- *Compensation*
  Defect levels can act as acceptors or donors and thereby compensate the effect of the doping.
- *Trapping*
  In principle, all kind of defects can be called trapping centres as they can catch charge carriers for a short time and re-emit them later. Especially harmful are those defects which have a high capture cross section and whose emission or detrapping time constant is large with respect to the charge collection time resulting in charge carrier loss.

The probabilities of these processes and of the occupation of defects can be calculated with the help of Fermi-Dirac statistics in thermal equilibrium or Shockley-Read-Hall statistics (for further details see [Mol99]).

The above-mentioned processes caused by defects in the band gap result in the following radiation-induced change of the macroscopic detector parameters:

- *Reverse Current*
  According to Eq. 2.10 the reverse current is inversely proportional to the generation lifetime, $I_{rev} \propto \frac{1}{\tau_g}$, because generation centres in the middle of the band gap are responsible for the reverse current. As the number of generation centres increases during irradiation, the reverse current also rises. Earlier investigations have shown that the change in reverse current $\Delta I = I_{irr} - I_0$ normalised to the sensitive detector volume V is linear to the equivalent fluence, irrespective of irradiation type, energy and Si material [Mol99]:

  $$\Delta I(\Phi_{eq}) = \alpha \Phi_{eq} V, \tag{3.5}$$

  with the *current damage parameter* α. The validity of this relation is believed to be so precise that it is in turn often used to determine or control the fluence of an irradiated sample via the current.
- *Depletion Voltage*
  As shown by Eq. 2.5 the depletion voltage is proportional to the effective doping concentration: $U_{dep} \propto |N_{eff}| = |N_D - N_A|$. The effective space charge is altered in two ways by radiation-induced defects: On the one hand dopant removal can occur if the doping atom forms a new complex defect with another radiation defect and is thereby electrically inactivated. On the other hand ionised defects can contribute to the effective doping concentration as ionised donors create positive and ionised acceptors negative space charge.

- *Doping Type*
  The above-mentioned change in N_{eff} can go so far that the initial doping type can change. For example if in an initially n-type diode so many acceptors are induced by irradation that they exceed the donors, this material changes to p-type. This phenomenon is called *type inversion* or *space charge sign inversion (SCSI)* and can occur at high fluences, depending on material and irradiation type. After type inversion the junction changes from one contact to the other with possible adverse effects on the position resolution, which has to be taken into account when deciding at which electrode to read out.

- *Charge Collection Efficiency*
  On the one hand the charge collection efficiency is reduced if it is not possible anymore to deplete the whole detector because this means a loss in sensitive volume. On the other hand it was shown in Sec. 2.2.5 how trapping described by an effective trapping time constant τ_{eff} reduces the charge collection efficiency. As mentioned above, radiation-induced defects act as trapping centres where the charge is captured with the probability $\frac{1}{\tau}$, depending on their concentration N_t, electron or hole capture cross section $\sigma_{e,h}$ and electron occupation probability f_t:

$$\begin{aligned} \frac{1}{\tau_{e,i}} &= N_{t,i} \cdot (1 - f_{t,i}) \cdot \sigma_{e,i} \cdot v_{th,e} && \text{for electrons and} \\ \frac{1}{\tau_{h,i}} &= N_{t,i} \cdot f_{t,i} \cdot \sigma_{h,i} \cdot v_{th,h} && \text{for holes.} \end{aligned} \tag{3.6}$$

  The overall effective trapping probability is the sum over the probability of individual traps: $\frac{1}{\tau_{eff,e,h}} = \sum_i \frac{1}{\tau_{i,e,h}}$. It has been shown experimentally by [Kra01] that the radiation-induced trapping probability is proportional to the equivalent fluence:

$$\frac{1}{\tau_{eff,e,h}} = \beta_{e,h}\Phi_{eq} \tag{3.7}$$

  with another damage parameter $\beta_{e,h}$, in this case related to trapping.

3.4.1 Overview on Identified Point Defects in Si

The most important known point defects that have an effect on detector parameters are listed below.

- *VP_s defect (E-centre)*: The combination of a vacancy with a phosphorus atom plays an important role in irradiated Si detectors because the phosphorus atoms are originally intended as shallow donors for obtaining n-type material. On the contrary, the VP_s defect has a level near the midgap which is usually neutral at room temperature. Thus after irradiation, the doping concentration reduces as P is transformed into VP_s (*donor removal*).

- *VO_i defect (A-centre)*: Oxygen exists in the Si crystal as electrically inactive interstitial atom. Together with a vacancy it forms a complex defect with an energy level $170meV$ below the conduction band, but has no influence on the electrical properties of the material. However, this defect is an interim step towards the creation of the V_2O_i defect that may alter the effective doping of the material (see below).

- *V_2O_i defect*: This acceptor-like defect is created by the second-order reaction of a V with a VO_i. According to [Pin03] this defect is identical with the I-centre that has a near-midgap level and is therefore very harmful regarding the effective doping concentration and the generation current.
- *Thermal donors*: After heat treatment in oxygen-rich material and after irradiation the creation of oxygen complexes, so-called thermal donors, is possible. They are able to influence the effective doping concentration. There are two types of thermal donors. On the one hand the single positively charged TDs, on the other hand the thermal double donors (TDD) which have double positive charge.

3.5 Defect Annealing

As already emphasised, many defects are mobile at room temperature and the above-described radiation damage only develops because the primary vacancies and interstitials form new complex defects with each other or other impurities. However, this is not the end of the story as these secondary defects are mobile as well so that they can migrate, form other complex defects or dissociate. Hence, also after irradiation the radiation damage develops further as a function of time and defect concentrations can change, a process called *annealing*.

Annealing studies are important because of two reasons. On the one hand, the annealing behaviour of defects can provide further information besides the caracterisation of electrical properties, which might help in identifying the microscopic nature of a defect. On the other hand, depending on the process and its time constant, the reactions can develop slowly so that even years after irradiation still changes may occur. Especially for detectors in particle colliders this is a factor limiting their application and has to be well-understood.

Three processes may happen during annealing:

- *Migration*
  Depending on temperature, defects become mobile and migrate through the Si lattice until trapped by sinks (e.g. surface, dislocations, etc.).
- *Complex Formation*
  Migrating defects can react with other defects or impurities. Some of them can recombine (e.g. $V + Si_i \rightarrow Si_s$), others form new complex defects (e.g. $V + O_i \rightarrow VO_i$).
- *Dissociation*
  A defect complex consisting of more than one component can dissociate into its single constituents if the energy of the absorbing phonon is larger than the binding energy of the complex. The new fragments in turn can migrate, recombine or build other defects.

3.5.1 Defect Kinetics

The change of the defect concentration can be described with the help of differential equations. Most of the processes follow the general rate equation

$$\frac{dN_X}{dt} = \pm k_\gamma N_X^\gamma, \tag{3.8}$$

where γ denotes the order of the process and is commonly but not necessarily an integer number, N_X is the concentration of defect X and k_γ is the rate constant. The sign depends on whether the reaction produces or destroys the respective defect. As an example, only the latter case is referred to in the further considerations. The rate constant is dependent on the temperature via an Arrhenius relation

$$k_\gamma = k_{\gamma,0} \exp\left(-\frac{E_A}{k_B T}\right), \tag{3.9}$$

where E_A is the activation energy of the reaction and k_B Boltzmann's constant.

- *First-Order Reactions ($\gamma = 1$)*
  Simple processes like migration of defects into sinks or dissociation can be described by a first-order process $X \rightarrow Y$ because the change of concentration dN_X only depends on their own concentration N_X, independently of other defects: $-\frac{dN_X}{dt} = k_1 N_X$. The solution is given by

$$N_X(t) = N_{X,0} \exp(-k_1 t) \qquad \text{with half life}^4\ \tau_{1/2} = \frac{\ln 2}{k_1}. \tag{3.10}$$

- *Second-Order Reactions ($\gamma = 2$)*
  The complex formation of a new defect out of two existing ones, on the contrary, is described by a second-order reaction $X_1 + X_2 = X_1 X_2$. To be precise, the change of the concentration of the initial defects depends on both N_{X1} and N_{X2}:

$$-\frac{dN_{X1}}{dt} = -\frac{dN_{X2}}{dt} = k_{X1,X2} N_{X1} N_{X2}, \tag{3.11}$$

  with a rate constant $k_{X1,X2}$ that depends on the capture radius and the diffusion coefficient. But for two cases simpler approximations can be made that can be related to Eq. 3.8.

  If one of the reaction partners has a much higher concentration than the other one (e.g. $N_{X1} >> N_{X2}$), the concentration of the first one can be assumed to be constant. The remaining rate equation is thus only dependent on the second (lower) concentration, which results in a first-order equation that can be solved as described above.

  On the other hand, if one assumes the concentrations of the initial reaction partners to be approximately equal, i.e. $N_{X1} \approx N_{X2} = N_X$, one obtains the simplified second-order equation $-\frac{N_X}{dt} = k_2 N_X^2$ like in Eq. 3.8 with $\gamma = 2$. This has the solution

$$N_X(t) = N_{X,0} \frac{1}{1 + k_2 N_{X,0} t} \qquad \text{with half life } \tau_{1/2} = \frac{1}{k_2 N_{X,0}}. \tag{3.12}$$

The most important difference between first- and second-order reactions can be seen from the half life: The annealing behaviour of first-order processes is independent of the defect concentration, whereas second-order reactions depend on N_X. In the latter case, a higher defect concentration results in a lower half life.

[4] The half life is defined as the time after which the concentration is reduced to half of the original concentration: $N(\tau_{1/2}) = N_0/2$.

3.6 Improving Radiation Hardness

The last sections showed how the detector parameters are affected after particle irradiation. To summarise the effect of radiation damage, one can say that there is a strong degradation of the signal-to-noise ratio as the leakage current and depletion voltage go up and charge collection efficiency decreases. At a certain point there is a limit after which the detector cannot be used anymore. The LHC with an expected equivalent fluence of $3 \times 10^{15} cm^{-2}$ in the innermost vertex layer over a time of 10 years has presented already an unprecedented challenge on the radiation hardness and the planned SLHC upgrade will even result in an about one order of magnitude higher fluence ($\approx 1.6 \times 10^{16} cm^{-2}$ over 5 years). Thus, an effective R&D programme is needed in order to develop detectors that are able to survive in such harsh radiation environments. This section presents some strategies of how to improve the radiation hardness.

3.6.1 Choice of Material - Defect Engineering

As described in the last sections, the types and concentrations of existing impurities play an important role in defect generation. So it is very important to understand the underlying microscopic mechanisms of radiation damage in order to tailor the material and its concentration of impurities in such a way that radiation damage is minimised. This approch is called *defect engineering* and has already proven to be successful in the case of oxygen enrichment of Si. Furthermore, other strategies like hydrogenation, p-type Si or completely different materials are investigated, but this is not subject of this work.

The Oxygen Effect

In the past, mainly high resistivity, oxygen-lean, n-type STFZ material had been used for detector applications. The radiation-induced change of the effective doping concentration in this material is dominated by donor removal (VP formation) and acceptor creation (supposedly V_2O) increasing with fluence. Thus, after relatively low fluences the material changes from n- to p-type and later on the depletion voltage rises to non-operable values.

It was found out that oxygen enrichment of the material can improve the situation dramatically for charged hadron and lepton irradiation [Fre05]. The type inversion of oxygenated FZ is significantly delayed and the increase of acceptor concentration at high fluences is not as steep as for STFZ. This effect can be explained either by oxygen-related suppression of acceptor creation or by a simultaneous donor creation that compensates the acceptors. According to [Pin05] it is probably a combination of both: As a radiation-induced deep acceptor V_2O is assumed, being created by the reaction $V + VO \rightarrow V_2O$. This reaction is supposed to be suppressed in the case of high oxygen concentration since the vacancy prefers the reaction $V + O \rightarrow VO$ to the V_2O creation. At the same time bistable donors (BD) and other shallow donors are presumably introduced, further slowing down the increase of $|N_{eff}|$ in DOFZ. BDs have similar properties as TDDs and their radiation-induced creation is probably connected to the concentration of oxygen dimers O_2.

This model is supported by the behaviour of MCz and EPI materials. They usually do not type-invert at all after charged hadron irradiation and at high fluences N_{eff} increases due to the predominant creation of donors instead of acceptors. According to the model this can be explained by an even higher concentration of O and O_2 in MCz and EPI than in DOFZ,

leading to enhanced V_2O suppression and shallow donor creation. Thus MCz and EPI are very interesting materials with respect to radiation hardness and investigated intensely.

3.6.2 Thin Detectors - Device Engineering

Radiation hardness of Si detectors cannot only be improved by the choice of the right material, but also by device optimisation, i.e. for example by changing the geometry of the wafer or the elctrodes. Examples are n-in-n technology, 3D detectors and thin devices. In this work thin detectors are investigated so that in the following a short overview on their properties is given.

Thin Detectors

A detector is called thin if its thickness is considerably smaller than the standard size of about $300\mu m$. There are two approaches to produce them: On the one hand the thinning of processed FZ and MCz wafers down to $50\mu m$, on the other hand the epitaxial growing of a thin Si layer (25 - $150\mu m$) on a thicker Cz substrate.

Nearly all of the most important detector parameters depend on the thickness d of the diode (cf. Sec. 2.2). Thus by using thin detectors it is possible to reduce the leakage current ($I_{rev} \propto d$) and especially the depletion voltage ($U_{dep} \propto N_{eff} \cdot d^2$) significantly. Furthermore this makes it possible to use lower resistivity Si, i.e. Si with a higher initial doping concentration $N_{eff,0}$, which delays the effect of dopant removal and is easier to produce.

Another great advantage of thin detectors is the improved charge collection efficiency, which is especially important because this seems to be the most limiting factor for the SLHC and up to now defect engineering has not provided a solution yet. The improved CCE is due to the shorter charge collection time so that less charge carriers are trapped during the drift. The charge collection time is obviously reduced because of the smaller drifting distance, but also because of a larger velocity as the average electric field is higher at a given voltage ($E \propto U/d$). However, for a minimum ionising particle there is the drawback that the deposited charge Q_0 is also reduced ($Q_0 \propto d$). After all, it is not the efficiency that counts but the overall collected measurable charge $Q = CCE \cdot Q_0$. So the right thickness has to be carefully chosen and optimised.

Another drawback of thin detectors, the increased capacitance ($C \propto A/d$), can be overcome by a smaller sensor cell size which needs to be developed anyway because of the high cell occupancies at SLHC luminosity.

To conclude, epitaxial detectors combine both the approaches of defect engineering (high O and O_2 concentration) and device engineering (thin). The purpose of this work is to study medium thick ($75\mu m$, $100\mu m$, $150\mu m$) standard and oxygen-enriched epitaxial diodes as the optimum thickness for maximum SNR might lie in this range, and to investigate the dependence of their radiation damage on thickness, impurity concentration, fluence and annealing time.

Chapter 4

Material and Experimental Methods

4.1 Diode Samples

In this work standard and oxygen-enriched epitaxial pad diodes of three different thicknesses ($75\mu m, 100\mu m, 150\mu m$) were studied.

4.1.1 Material

The main parameters of the used materials are listed in Tab. 4.1. The epitaxial layers were grown by ITME [ITME] on a Cz substrate of about $500\mu m$ thickness. The substrate is highly doped with antimony (Sb, $0.02\Omega cm$) in order to provide a good ohmic contact and to prevent it from acting as a sensitive detector region. The crystal orientation of EPI $75\mu m$ is <111> and differs from the <100> orientation of EPI $100\mu m$ and EPI $150\mu m$. The initial doping concentration $N_{eff,0}$ with phosphorus is deliberately chosen to vary between $2.6\times10^{13}cm^{-3}$ for $75\mu m$, $1.5\times10^{13}cm^{-3}$ for $100\mu m$ and $8\times10^{12}cm^{-3}$ for $150\mu m$ in order to obtain approximately the same initial depletion voltage $U_{dep,0}$ of about 100 - 150V for all thicknesses.

Fig. 4.1 shows the oxygen concentration depth profile obtained from *secondary ion mass spectrometry (SIMS)* measurements performed by [SIMS]. For EPI-ST it is clearly visible that there is an out-diffusion of oxygen from two sides, mainly from the Cz substrate, but also from the SiO_2 surface layer. This results in an inhomogeneous distribution with a concentration variation of more than one order of magnitude between the minimum and the maximum. The average concentration increases for decreasing thickness ($4.5 \times 10^{16}cm^{-3}$ for $150\mu m$, $9.3 \times 10^{16}cm^{-3}$ for $75\mu m$) because in a thin layer the ratio of diffusion range (if assumed to be constant) and thickness is larger. Homogeneity and average concentration are largely

Material	d [μm]	Wafer	Orien-tation	$N_{eff,0}$ [P] [$10^{12}cm^{-3}$]	ρ [Ωcm]	$U_{dep,0}$ [V]	[O] [$10^{16}cm^{-3}$]	[C] [$10^{15}cm^{-3}$]
EPI-ST 75	74	8364-03	<111>	26	165	110	9.3	<1.9
EPI-DO 75	72	8364-07	<111>	26	167	103	60.0	<1.6
EPI-ST 100	102	261636-05	<100>	15	287	118	5.4	<3.9
EPI-DO 100	99	261636-01	<100>	15	285	113	28.0	<1.7
EPI-ST 150	147	261636-13	<100>	8.8	490	145	4.5	<2.8
EPI-DO 150	152	261636-09	<100>	8	538	140	14.0	<1.6

Table 4.1: Properties of the used materials (average values).

improved for EPI-DO after oxygenation at 1100°C for 24h. For these diodes, the average concentration varies between $1.4 \times 10^{17} cm^{-3}$ for $150\mu m$ and $6.0 \times 10^{17} cm^{-3}$ for $75\mu m$.

The results for the carbon concentration were found to vary between $1.2 \times 10^{15} cm^{-3}$ and $5 \times 10^{15} cm^{-3}$ for the different processing procedures, but such small concentrations are expected to be below the detection limit of the SIMS method [RD50-07].

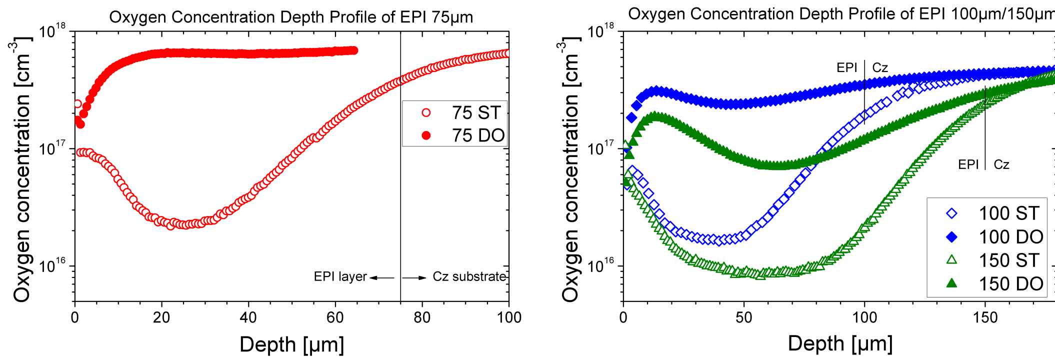

Figure 4.1: Oxygen concentration depth profiles (SIMS measurements).

4.1.2 Devices

The diodes were processed by the company CiS [CiS]. For this work so-called *pad diodes* were used, which are displayed in a top-view and side-view sketch in Fig. 4.2. Pad detectors are large simple planar diodes without segmentation, which are easy to produce and handle so that they are very suitable test structures for material investigations.

The p-n junction is produced by boron implantation that creates a $1\mu m$ thick p^+ layer with a high doping level of about $10^{19} cm^{-3}$ at the front side. The junction is constructed in such a way that there is one central pad diode in the middle of either $0.5 \times 0.5 cm^2$ or $0.25 \times 0.25 cm^2$ size[1] and a guard ring structure surrounding it. The guard ring that has to be kept at the same potential as the pad has two main functions. On the one hand it helps in keeping the area of the central pad and the electric field well-defined, on the other hand it shields the pad from surface and edge leakage currents. The guard ring is $100\mu m$ wide with a distance of $10\mu m$ to the pad. Often there are further smaller potential rings around the main guard ring, which are operated in floating mode to lower the potential difference between the central pad and the edges of the detector.

The metallisation of the front contact is done with aluminium, but leaving a hole of $2mm$ diameter in the middle for optical charge carrier injection. The back side is coated with an aluminium mesh which also allows optical illumination for other materials that do not have a substrate. The parts of the detector that are not metallised are covered with silicon oxide (SiO_2) for passivation and protection.

A list of the devices investigated in this work can be found in Appendix A.

[1] Labelled as *big* and *small*, respectively, in the following.

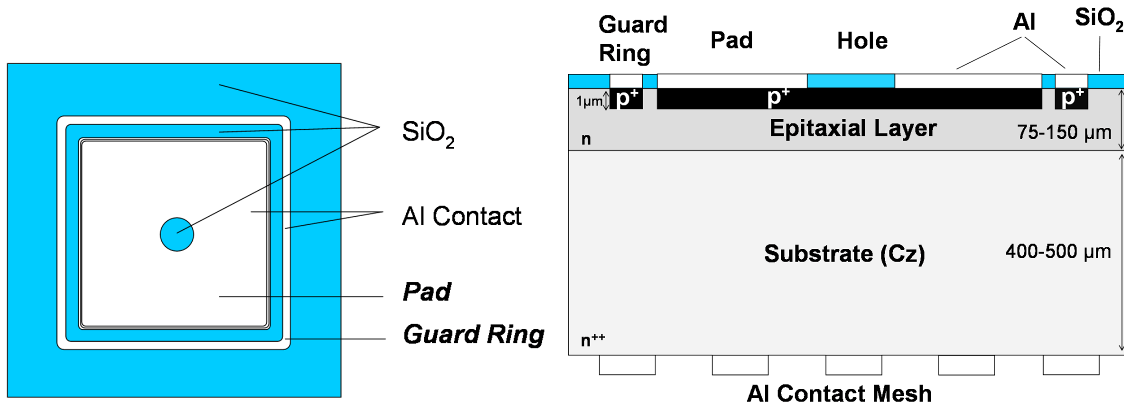

Figure 4.2: Schematic top view (left) and cross section (right) of the used pad diodes (not to scale).

4.2 Irradiation

In the context of this work, diodes irradiated with $24GeV/c$ protons in an equivalent fluence range between $10^{14}cm^{-2}$ and $10^{16}cm^{-2}$ were studied (see Tab. 4.2). The irradiation was performed with the Proton Synchrotron beam (PS) at CERN. The samples were mounted on a cardboard slide and transported automatically by a shuttle into the beam. The beam had a diameter of about $2cm$ and homogeneous irradiation can be achieved by sweeping it in a constant rate over the samples. This results in an average proton flux of about $(3-9)\times 10^9$ p $cm^{-2}s^{-1}$. Thus, for high fluences quite long irradiation times were needed, up to weeks (see Tab. 4.2). As irradiations were performed at about 27 - 29°C, the question of self-annealing already during irradiation has to be considered carefully.

The achieved fluences were measured by aluminium activation. One Al foil of $5\times 5mm^2$ and one of $10\times 10mm^2$ size were placed together with the samples in the beam and activated by the reactions ^{27}Al(p,3pn)^{24}Na and ^{27}Al(p,3p3n)^{22}Na. The half-lives of ^{24}Na and ^{22}Na are 15h and 2.6 years, respectively. The intensity of the gamma emission lines of ^{24}Na ($E_\gamma = 1369keV$) and ^{22}Na ($E_\gamma = 1275keV$) as measured by a NaI or Ge spectrometer can be used to obtain the Al activity. The Al activity is proportional to the received proton fluence if the time between irradiation and activity measurement is taken into account. The systematic error of the measured fluence is reported to be in the order of 10%. However, it turned out that some of the fluences had to be corrected afterwards using the current damage parameter $\alpha = 4\times 10^{-17}Acm^{-1}$ (see Sec. 5.2.1). The equivalent fluence values were obtained using a hardness factor of $\kappa = 0.62$ for the PS $24GeV/c$ proton source. Further information concerning the irradiation can be found in [PIrS].

4.3 Annealing Experiments

Isothermal annealing experiments at 80°C were performed in order to investigate how the radiation damage develops over time. The temperature of 80°C has been chosen in order to speed up the annealing (e.g. for FZ the N_{eff} reverse annealing is accelerated by a factor of 7430 with respect to room temperature, assuming an activation energy of 1.33 eV [Mol99]). But at even higher temperatures there would be the danger of other annealing reactions that

$\Phi_p[cm^{-2}]$	$\Phi_{eq}[cm^{-2}]$	$\Phi_{eq}[cm^{-2}]$ simplified notation	irradiation duration
1.66×10^{14}	1.03×10^{14}	1×10^{14}	5h23min
4.88×10^{14}	3.03×10^{14}	3×10^{14}	18h34min
1.73×10^{15}	1.07×10^{15}	1×10^{15}	8d12h44min
6.25×10^{15}	3.88×10^{15}	4×10^{15}	12d14h34min
1.06×10^{16}	6.57×10^{15}	7×10^{15}	
1.71×10^{16}	1.06×10^{16}	1×10^{16}	

Table 4.2: The denoted proton fluence Φ_p as measured by Al activation, the corresponding equivalent fluence Φ_{eq} using $\kappa = 0.62$, the simplified notation of the equivalent fluence that will be used in the following for fast reference and the irradiation duration.

do not occur at room temperature.

For annealing the test structures were heated up in a circulating air oven from the company *Heraeus*. The temperature stability of the oven was around ±1°C. Between the measurements the irradiated samples were stored at -25°C in order to avoid unwanted annealing.

4.4 CV and IV Measurements

In order to obtain the macroscopic detector parameters depletion voltage (U_{dep}) and reverse current at full depletion (I_{dep}), measurements of the capacitance-voltage (CV) and current-voltage (IV) characteristics of the samples were performed. An equivalent circuit representing a reverse-biased diode is shown in Fig. 4.3. The detector can be described by a capacitor C in parallel with a resistor R_p that accounts for the leakage current. In addition, there is a serial resistor R_s which represents the resistance of the undepleted detector bulk.

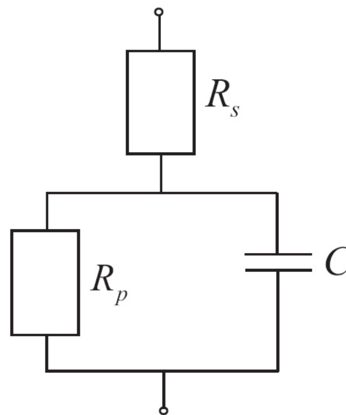

Figure 4.3: Equivalent circuit representing a reverse-biased detector.

However, the used capacitance bridge can only measure two parameters: The real and imaginary part of impedance Z or alternatively admittance $Y = Z^{-1}$. So the model has to be further simplified and one has to choose between either serial mode where the leakage current is neglected ($R_p \to \infty$) so that $Z = R_s - j\frac{1}{\omega C_s}$ or parallel mode where R_s is neglected ($R_s \to 0$) so that $Y = \frac{1}{R_p} + j\omega C_p$. C_s and C_p is the measured detector capacitance as obtained in serial and parallel mode, respectively, j is the imaginary unit and $\omega/2\pi$ the measurement frequency.

It is possible to convert from one mode to another, e.g. from parallel to serial mode via

$$C_s = \frac{1 + \omega^2 R_p^2 C_p^2}{\omega^2 R_p^2 C_p} \qquad \text{and} \qquad R_s = \frac{R_p}{1 + \omega^2 R_p^2 C_p^2}. \tag{4.1}$$

When the detector is unirradiated neither the bulk generates a high leakage current nor the undepleted region is high-resistive. Thus the impedance is mostly dominated by C only so that both modes give comparable results. However, when the detector is irradiated both R_p and R_s would be needed for a correct description as both the undepleted region becomes intrinsic, i.e. highly resistive, and the leakage current increases. For not too high fluences and leakage currents the serial mode has been chosen. But in some cases for extremely high leakage currents the parallel mode becomes a better approximation. Moreover, due to the presence of a large number of deep defects in irradiated detectors, a further frequency and temperature dependence of the capacitance measurement is introduced [Dab89]. For comparison one has agreed on standard measurements at $10kHz$ and room temperature because investigations have shown that the thereby extracted depletion voltage matches the one obtained by charge collection measurements best.

For the measurements the samples were fixed with a vacuum pump on a biased chuck inside a probe station in the dark in order to avoid photo currents. The pad and the guard ring were contacted each with a needle and kept at ground potential. For the CV measurements an HP[2] 4263A or 4263B LCR meter was used which measured the admittance or the impedance by superimposing a small AC voltage with a specific amplitude and frequency on the DC reverse bias voltage. The high bias voltage had to be decoupled from the bridge with the help of an adapter box as it was limited to voltages below $20V$. Usually the LCR meter was run in parallel mode with an amplitude of $0.5V$ and a frequency of $10kHz$ and after performing an open correction. As a bias source and to measure the pad current a Kei[3] 487 (limits: $500V$, $2mA$) or a Kei 6517A ($1000V$, $1mA$) were used. The guard ring current was measured with a Kei 6485 and the temperature with a Pt 100 sensor connected to a Kei 2700.

The evaluation of the characteristics was done using the programme *detwnd*. The CV measurement was usually transformed from parallel to serial mode and the current scaled to 20°C according to Eq. 2.11. The CV curve was plotted in a log-log diagram and the depletion voltage was determined from the intersection of two straight fitted lines near the kink (see Fig. 4.4). I_{dep} is obtained as the corresponding reverse current at U_{dep}.

Problems and Limitations

One of the most important problems was the current limit of $1 - 2mA$ of the used voltage source. The reverse current increases with fluence so that highly irradiated diodes could not be measured anymore. Cooling of the samples can be a solution in order to decrease the current, but in this case also the capacitance measurements are affected due to the mentioned deep-defect related frequency and temperature dependence. Unfortunately a reliable method to transform capacitance measurements from low temperatures to room temperature is not known up to now. However, to improve the situation at least a bit, measurements of diodes with current problems were done on a temperature-controlled cooled chuck at 20°C. On the one hand this is a bit less than the laboratory temperature and even a reduction of only 2°C

[2] *Hewlett Packard.*
[3] *Keithley.*

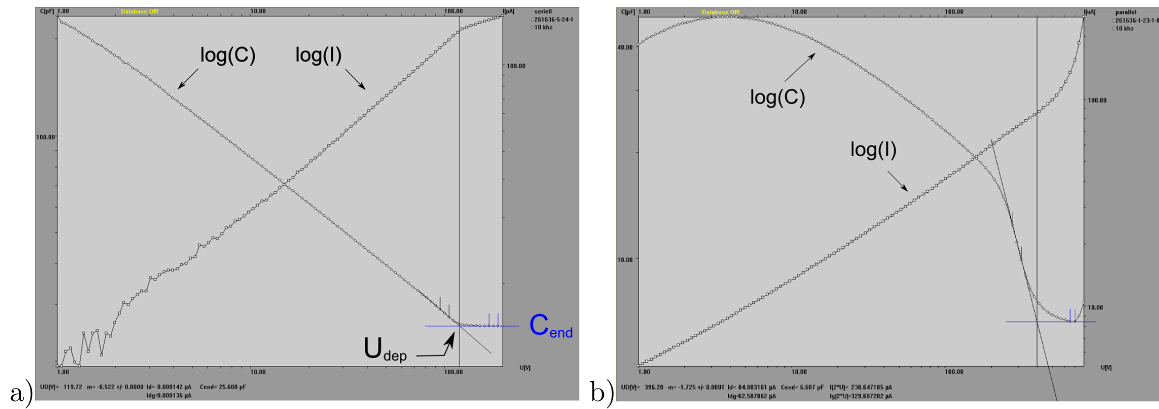

Figure 4.4: a) Example of a CV and an IV characteristic and the determination of U_{dep} and I_{dep} for an unirradiated EPI-ST 100μm detector as displayed in the programme *detwnd*. b) The CV and IV characteristic of a highly irradiated EPI-DO 100μm detector in parallel mode ($\Phi_{eq} = 4 \times 10^{15} cm^{-2}$).

results in a current decrease of 15% according to Eq. 2.11. On the other hand cooling prevents the diode from heating up and suffering from thermal runaway.

But even if the current is not out of limit, there can be nevertheless further complications at high fluences. Ideally both the CV and IV curve saturate after full depletion if the guard ring is connected as was done here, but in reality there are deviations. For the IV characteristic it is visible from Fig. 4.4 a) that even unirradiated diodes do not really saturate, which is not yet understood. But there is at least a clear kink between two obviously straight parts with the gradient of the curve after depletion being significantly less than before depletion. For the IV curve of highly irradiated diodes, however, it can happen that there is no clear distinction possible between under- and overdepletion and sometimes the slope is even increasing instead of decreasing (see Fig. 4.4 b)). Such behaviour might be explained by diode breakthrough, avalanche or thermal runaway effects. In this case a reliable determination of I_{dep} is questionable, especially if the depletion point is near or even after the beginning of the breakthrough. There can be also severe complications for the determination of U_{dep} at high fluences. The most important ones are the failure to reach the expected geometrical end capacitance and the re-increase of the CV curve at high bias voltage. These two phenomena are often but not necessarily linked and probably result from the fact that a reliable capacitance measurement is difficult at high currents. These problems are even more severe if the CV curve is transformed from parallel to serial mode. As at high reverse current the parallel mode becomes a better description close to depletion anyway, the analysis is done using parallel mode for high fluences.

Besides the here mentioned problems with the measurement techniques there are further complications for the analysis of U_{dep} and hence N_{eff} arising from inhomogeneous N_{eff} distributions. This will be discussed further when the experimental results will be presented in Sec. 5.1.

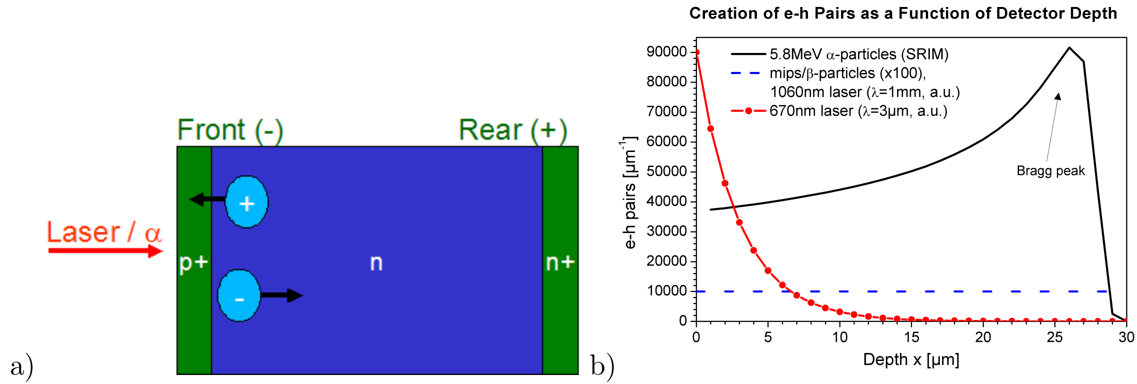

Figure 4.5: a) TCT principle. b) Creation of e-h pairs as a function of detector depth for different TCT methods (mips, β, α, $670nm$ laser). The normalisation of the laser-induced e-h pairs is arbitrary, it depends on the energy and focus of the laser pulse.

4.5 Transient Current Technique

The transient current technique (TCT) is an important tool to study signal formation, charge collection and trapping mechanisms in the detector. The basic principle (see Fig. 4.5 a)) is to generate free charge carriers inside the detector, let the charge drift towards the respective electrodes under the influence of an applied bias voltage and to measure the induced current signal and/or the collected charge. Recall that the induced current is given by Eq. 2.12:

$$I_{e,h}(t) = \frac{q_0 N_{e,h}(t)}{d} v_{dr_{e,h}}(t).$$

There are various TCT methods which can investigate different aspects of charge collection. They mainly differ in the location where the original charge is created inside the detector (cf. Fig. 4.5 b)). What is interesting in the end for the application in particle colliders is the collected charge of a traversing mip that deposits charge continuously throughout the whole detector depth. This can be simulated either by a β-source like ^{90}Sr or by a short ($\approx 1ns$) infrared laser pulse of e.g. $1060nm$ wavelength with $\lambda = 1040\mu m$ absorption length. However, for a detailed investigation of the underlying trapping mechanisms it can be useful to deposit the charge only locally, especially close to one of the surfaces, as e.g. a red laser of $670nm$ wavelength or an α-particle does. In this case only one type of the charge carriers (electrons or holes) drifts through the detector volume whereas the second type is collected immediately by the adjacent electrode and induces hardly any current. Thus the measured current is a clean signal of one carrier type only, one speaks of electron and hole injection, respectively. In this way, the trapping time constant and CCE of the respective carrier type can be obtained. Moreover, the charge carrier acts as a probe for the electric field because according to Eq. 2.12 $I_{e,h}(t) \propto v_{dr_{e,h}}(E(x(t)))$. For constant mobility in the low-field case, the current is even directly proportional to the field strength, otherwise the picture is a bit smeared. So the behaviour of the electric field strength inside the detector can be analysed using the current signal. In particular, the question can be answered whether the detector bulk is n-type or space charge sign inversion to p-type has occurred. An example is shown in

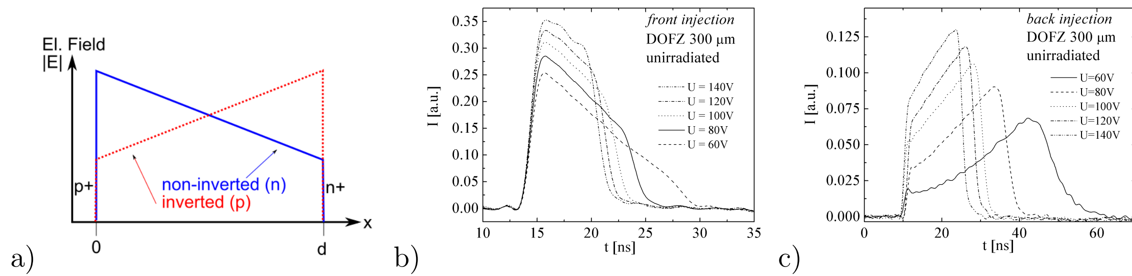

Figure 4.6: a) Electric field distribution (absolute value, linear-field approximation) before and after type inversion. b) Current signal (electrons) for an unirradiated 300μm DOFZ detector after front illumination with a 670nm laser. c) Current signal (holes) for the same detector after back illumination (taken from [Sch03]). Remark: After inversion the electron signal (front illumination) would look like c) and the hole signal (back illumination) like b).

Fig. 4.6 for an unirradiated 300μm DOFZ detector[4]. In non-inverted diodes the field has its maximum absolute value at the p^+ front side (see Fig. 4.6). For front injection the current decreases with time as the electrons drift from the high-field region to the back contact. For back injection the current increases as the holes drift from the low-field region at the back to the front contact. After type inversion the space charge of the bulk changes to negative and the p-n junction together with the maximum of the field is now at the n^+ backside. In this case the behaviour of the electron and hole current is swapped.

In this work TCT with 670nm laser light and α-particles has been used so that these methods and their setups will be described in the following. It has to be noted that for EPI diodes only front injection of the charge carriers is possible because of the thick insensitive Cz substrate at the back side. Therefore only the electron signal can be acquired.

4.5.1 TCT with α-Particles

The advantage of the TCT setup with α-particles[5] is the easy and reliable way to obtain the CCE because the mono-energetic α-particles deposit always the same amount of energy and consequently e-h pairs inside the detector. Thus, the CCE can be determined by normalising the collected charge Q of an irradiated detector to the one of an unirradiated diode Q_0 that is assumed to be identical to the overall deposited charge due to the absence of trapping.

For this work a ^{244}Cm source was used which emits 5.8MeV α-particles. But before these particles deposit charge inside the sensitive detector region they first traverse about 2mm air and a dead layer consisting of approximately 100nm SiO_2 and the 1μm p^+ implantation, where they lose already a small part of their energy. Fig. 4.5 b) shows the created e-h pairs as a function of detector depth as simulated by *SRIM* [SRIM]. Charge is created starting from the p-n junction ($x = 0$) up to 29μm inside the detector with a clear maximum (Bragg peak) at 26μm. This means that charge is not only created directly near the surface, but also in a certain region inside the bulk so that also holes contribute a bit to the current, especially for very thin detectors. The overall deposited ionisation energy inside the sensitive region is simulated to be 5.5MeV corresponding to 1.5×10^6 e-h pairs.

[4] A DOFZ detector was chosen for illustration because for EPI diodes back injection is not possible and it is hard to obtain time-resolved signals (see Sec. 4.5.2).

[5] In the following referred to as α-*TCT*.

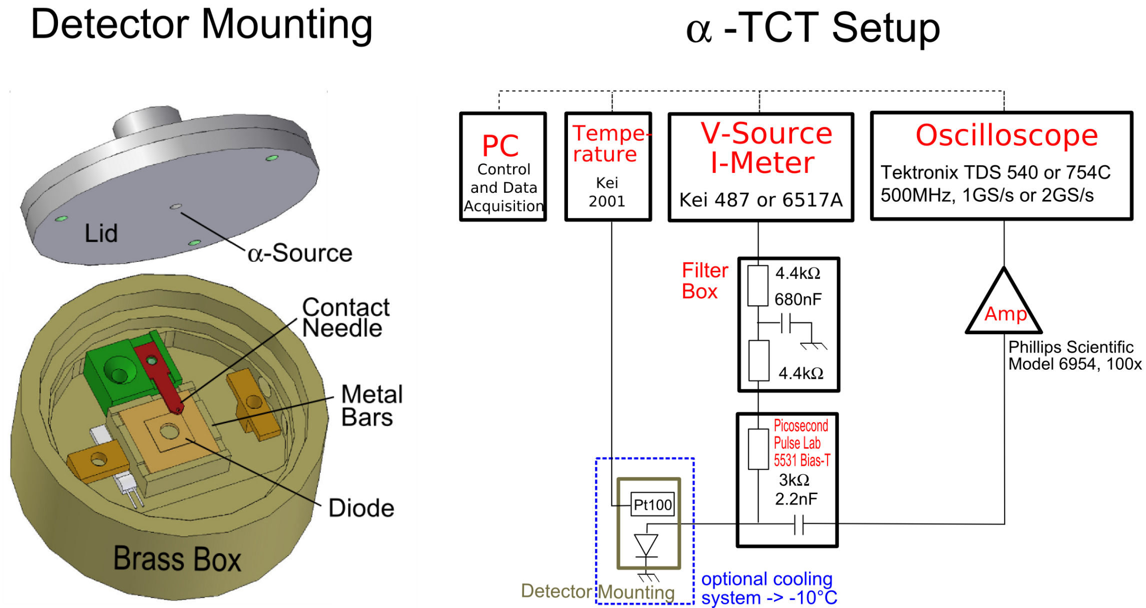

Figure 4.7: α-TCT setup (right) including a close-up of the detector mounting (left).

The setup of the α-TCT can be seen in Fig. 4.7. The diode was mounted in a brass box with metal bars surrounding it at each side in order to fix it at a well-defined position. It was biased and the signal was read out at the p^+ front side via a small needle on a cantilever spring. The α-source was in the middle of the lid which was put on the box during the measurements so that the source was about $2mm$ directly above the injection hole of the diode. A Picosecond Pulse Lab 5531 bias-T was used to decouple the Kei 487 or Kei 6517A voltage source, which served simultaneously also as a current meter, from the input of the amplifier (Phillips Scientific Model 6954 100x, $1.5GHz$ bandwidth). This was connected to a $500MHz$ bandwidth oscilloscope (Tektronix TDS 540, $1GS/s$, or Tektronix TDS 754C, $2GS/s$). The trigger level was set to $80mV$ in order to be above the noise level and trigger on the signal only. In order to enhance the SNR further 300 signals were averaged and a low pass filter box was used to cut off the high frequency noise of the voltage source. In the later analysis of the data the voltage drop at the resistors in the filter box and bias-T was taken into account (here: $11.8k\Omega$).

The high leakage current of highly irradiated diodes was also a problem for the TCT measurements. It was solved for α-TCT by placing the mounting with the detector on a Peltier-cooled, temperature-stabilised chuck in order to measure at -10°C so that the current was suppressed by a factor of about 19. In Sec. 5.4.2 it will be shown that there is no measurable difference between the CCE obtained at 20°C and -10°C.

In Fig. 4.8 an example of an α-TCT current signal is displayed. It can be seen that there is no good time resolution of the current signal, only a smeared peak mainly because of the large capacitance of the thin diodes, which will be discussed further in the next section. Thus only the collected charge, i.e. the integrated current, can be used for analysis.

Sometimes a problem due to micro discharges which caused a flickering of the signal occurred at high voltages so that in this case a reliable signal could not be obtained. This might be enhanced by the metal bars of the mounting which are at ground potential and

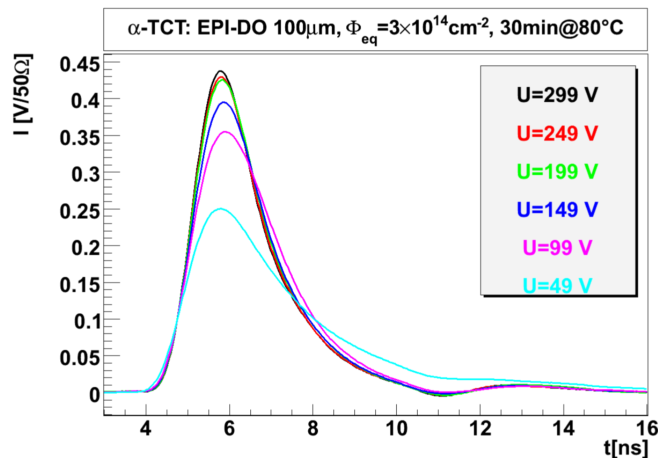

Figure 4.8: An example of an α-TCT signal for an EPI-DO $100\mu m$ detector. No time resolution could be achieved.

have sometimes contact to the edges of the diode. Another problem arose because the diodes were pressed against the back contact only by the needle on the cantilever spring. Thus, especially the small diodes often showed a contact problem resulting in a strongly reduced signal. Consequently, for CCE analysis only large diodes were used.

4.5.2 TCT with a 670nm Laser

The light from a $670nm$ laser creates charge carriers very close to the surface, in the case of EPI diodes at the front side so that almost exclusively electrons contribute to the signal. The absorption of photons in Si and thus also the generated charge carrier density is given by

$$n(x) = \frac{N_{e-h}}{\lambda A_i} \exp\left(-\frac{x}{\lambda}\right), \tag{4.2}$$

where N_{e-h} is the number of created e-h pairs, A_i the illuminated area and λ the absorption length of light in Si, which is only $3.3\mu m$ for a $670nm$ laser [Kra01]. The graph is shown in Fig. 4.5 b).

Another important difference compared to α-TCT is the trigger. Whereas the α-TCT signal is self-triggered, the trigger for the laser-TCT is externally provided by the pulse generator of the laser driver. This ensures operation also for a small signal, i.e. also for low bias voltages under depletion. However, a drawback of the laser method is the bad reproducibility of the laser intensity resulting in an unknown generated charge carrier number so that it is inappropriate for CCE determination.

The first measurements were done with an already existing setup that was similar to the α-TCT setup described above with the following differences. On the one hand an HP 8110A pulse generator was used to fire a laser diode and trigger the oscilloscope and on the other hand a different mounting for the detector was used which only allowed the measurement of the large diodes (for more details see [Sch03]). Fig. 4.11 a) shows a TCT signal taken with this setup for an EPI-ST $150\mu m$ detector. Unfortunately, like for α-TCT, even for the rather thick $150\mu m$ EPI diodes no time-resolved signal could be obtained.

For a good time resolution it is important that the ratio between charge collection time

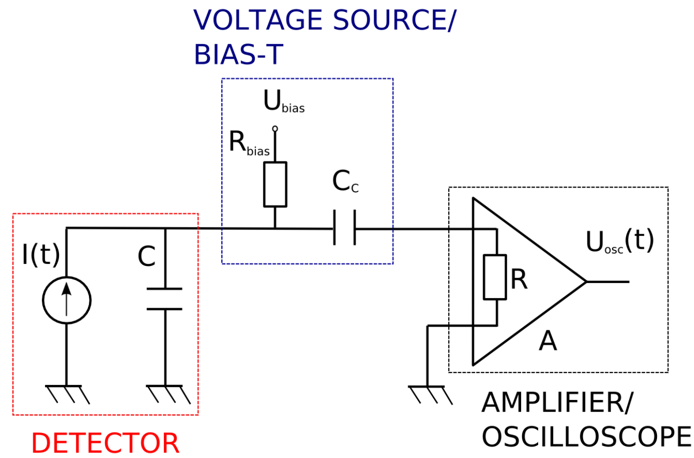

Figure 4.9: The equivalent circuit of detector and TCT setup. The detector provides the signal current $I(t)$, which is shaped by the system out of detector capacitance C in parallel to the input impedance $R = 50\Omega$ of the amplifier/oscilloscope (the decoupling capacitor C_C is so large that it can be neglected). Thus, the detector - read out system acts like an amplifying low pass filter with time constant $\tau_{RC} = RC$.

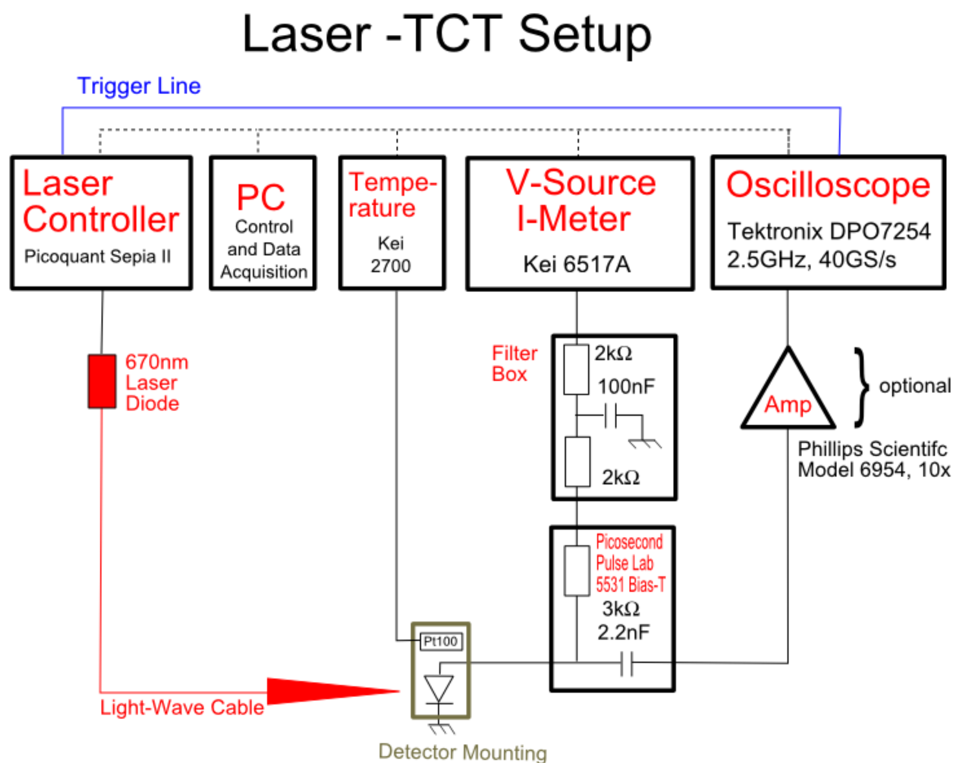

Figure 4.10: The new TCT setup with a 70ps laser, a 2.5GHz oscilloscope and a mounting for small diodes.

t_C on the one hand and signal rise time[6] respectively fall time on the other hand is as large as possible. However, for thinner diodes this ratio decreases quickly. Assuming a constant drift velocity close to saturation, i.e. $v_{dr} \approx 10^7 cm/s$, the charge collection time is $1.5ns$ for a $150\mu m$ detector and even less for thinner diodes. In contrast, the rise and fall times are dominated firstly by the RC time constant[7] τ_{RC} of detector capacitance and amplifier input impedance (for more explanation see Fig. 4.9). As $C \propto A/d$, τ_{RC} rises with decreasing thickness and is about $0.88ns$ for the $150\mu m$ thick big diodes with $C = 17.5pF$ and even larger for thinner diodes. Secondly, the signal rise and fall time is influenced by the rise time of the used electronic devices, which was in this case mainly dominated by the oscilloscope bandwidth BW according to $\tau_{Osc} \approx 0.34/BW$. A bandwidth of $500MHz$ results in $\tau_{Osc} \approx 0.68ns$. And thirdly, the pulse duration of the laser is an important parameter, it was $\geq 1ns$. To conclude, all three listed parameters are of the same order as the charge collection time. Consequently, in order to obtain a good time resolution for thin EPI diodes, the rise and fall time of the signal has to be reduced considerably.

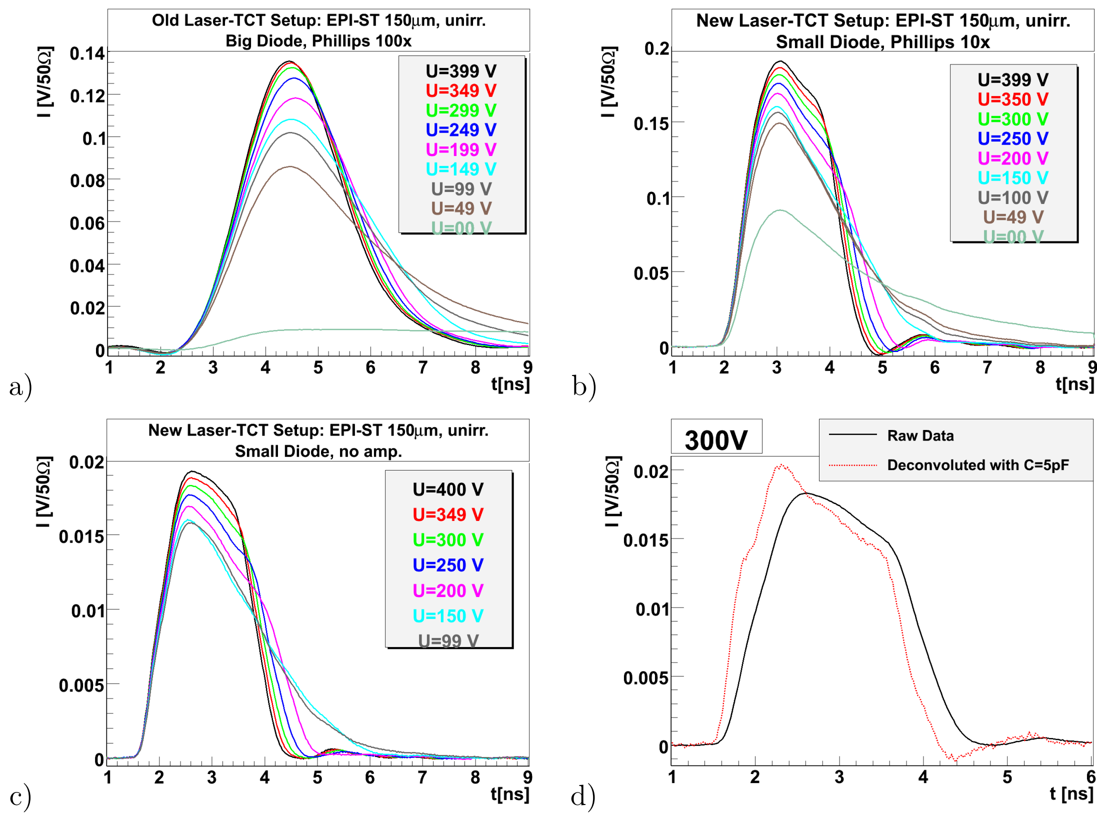

Figure 4.11: Comparison of 670nm laser-TCT signals taken with different setups for an unirradiated EPI-ST $150\mu m$ diode. a) Old setup, large diode, measured rise time $1.3ns$. b) New setup, small diode, with amplifier, measured rise time $0.6ns$. c) New setup, small diode, without amplifier, measured rise time $0.6ns$. d) Effect of deconvolution with $5pF$, setup like c).

This could be achieved by a new TCT setup that could reach improvements in all three mentioned aspects. In Fig. 4.10 a sketch of the new setup is displayed. First of all, as a

[6]The rise time is defined as the time difference between points where the leading edge reaches 10% and 90% of the peak maximum.

[7]The rise time for such an RC system when applying a simple step function signal is even $2.2\tau_{RC}$.

mounting for the diodes the same box as for the α-TCT was used. This enabled the measurement of the small diodes, which reduced the detector area and consequently capacitance by a factor of 4 so that τ_{RC} could be lowered to $0.22ns$ for $150\mu m$ diodes. This alone was enough to get a time-resolved signal to some extent. But further improvements were made by exchanging the $500MHz$ oscilloscope for a $2.5GHz$ oscilloscope (Tektronix DPO 7254, $40GS/s$, $\tau_{Osc} \approx 0.14ns$) and the old laser diode for a fast Picoquant Sepia II laser system with a $70ps$ laser pulse. Measurements were made with a Phillips Scientific Model 6954 amplifier (10x, $1.8GHz$ bandwidth) or even without amplification. 1000 signals were averaged. Fig. 4.11 shows a juxtaposition of TCT signals for an unirradiated EPI-ST $150\mu m$ diode taken with the old and the new setup. A significant improvement in time resolution is easily visible. The measured rise time of the signal of the old setup is $1.3ns$, the one of the new setup is $0.6ns$. The most prominent influence of the amplifier is the undershoot after the signal. The applied bias voltage was corrected for the voltage drop at the resistors in the filter box and bias-T (in total $7k\Omega$ for the new setup).

The problems during the measurements were the same as for the α-TCT with the small diodes because the same mounting principle was used. There was occasionally a bad contact leading to a shoulder at the end of the signal and micro discharges at high voltages. For future measurements it would be desirable to have a detector mounting that does not embrace the diode with metal bars and that presses the sample more strongly on the back plane to ensure a better contact.

Signal Deconvolution

As explained above, the RC system out of detector capacitance and amplifier/oscilloscope input impedance leads to a finite rise time and to a distortion of the original signal (*convolution*). Assuming the equivalent circuit from Fig. 4.9, it can be calculated from the transfer function of this system that the voltage measured at the oscilloscope $U_{osc}(t)$ depends on the original signal current $I(t)$ as

$$U_{osc}(t) = \frac{AR}{\tau_{RC}} \exp\left(-\frac{t}{\tau_{RC}}\right) \int_{-\infty}^{t} I(t') \exp\left(\frac{t'}{\tau_{RC}}\right) dt', \tag{4.3}$$

where A is the amplifier gain, $R = 50\Omega$ the input impedance and $\tau_{RC} = RC$ the time constant[8]. This equation can be rearranged to give

$$I(t) = \frac{\tau_{RC}}{R} \frac{dU_{osc}(t)}{dt} + \frac{U_{osc}(t)}{R}. \tag{4.4}$$

Thus it is theoretically possible to correct for the RC effects and to re-obtain the original current signal of the detector by deconvolution. In practice, however, this is only possible to a certain extent because there are always other effects also interfering (e.g. laser rise time, other electronic distortions). Fig. 4.11 d) shows a comparison between a measured current pulse and the deconvoluted signal. A capacitance of $5pF$ has been chosen, which is a bit larger than the geometrical capacitance of $4.4pF$ because the TCT measurements could be only performed without contacting the guard ring, which increases the effective area and thus the capacitance of the diode. The rising and falling edge become a bit steeper and the rise time is reduced by $0.1ns$ to $0.2ns$, but it is still around $0.5ns$. After deconvolution there

[8]A more detailed derivation can be found in [Kra01].

is a small undershoot after the signal and the noise is enhanced, e.g. due to the numerical differentiation.

Chapter 5

Experimental Results

In this chapter the experimental results of the investigation of macroscopic radiation damage in epitaxial silicon diodes will be presented and discussed. The first section will give an overview on general properties of the measured CV and IV characteristics. In the following, the fluence and annealing time dependence of the reverse current and the depletion voltage respectively effective doping concentration will be studied. The last section will present results related to charge collection properties and trapping obtained with α- and laser-TCT.

5.1 CV and IV Characteristics

CV and IV measurements were performed for both big and small diodes so that it was possible to cross-check the results at a certain fluence and to increase the number of data points. For the $150\mu m$ diodes there was even a second set of big diodes measured (labelled *big 2*). A good CV and IV curve and thus a reliable determination of U_{dep} and I_{dep} could be achieved for the equivalent fluence values $1 \times 10^{14} cm^{-2}$, $3 \times 10^{14} cm^{-2}$ and $1 \times 10^{15} cm^{-2}$ as shown in Fig. 5.1. From considering the variations due to repeated measurements and using different modes (serial/parallel) and different fitting ranges around the kink the achieved precision of U_{dep} and I_{dep} is estimated to be below 5%. The results for the diodes irradiated by $4 \times 10^{15} cm^{-2}$, however, have to be treated with great care. At this fluence DO $150\mu m$ could not be measured at all whereas for ST $150\mu m$ and DO $100\mu m$ only the small devices could be taken because the reverse current of the big ones exceeded the current limit of the voltage source. But also the diodes that could be succesfully measured at this fluence showed the problems of the non-saturating current and sometimes not-reached end capacitance as explained in Sec. 4.4. Those CV/IV characteristics were analysed in parallel mode and the uncertainty is estimated to be much larger, i.e. about 10% for U_{dep} and 20% for I_{dep}. Detectors at fluences even higher than $4 \times 10^{15} cm^{-2}$ could not be measured at all at room temperature.

Fig. 5.1 shows example CV/IV characteristics for ST $150\mu m$ and DO $150\mu m$. There are obviously significant differences between ST and DO as the curves of ST material are much more complex than the ones of DO. There are clearly distinguishable regions with varying slopes, which hint at a non-uniform distribution of N_{eff}, especially for ST. This might have two reasons: On the one hand the density of radiation-induced defect centres itself might be inhomogeneous, which seems quite reasonable to assume if recalling the non-uniform distribution of oxygen (see Fig. 4.1) and possibly other impurities. On the other hand it might be also caused by an inhomogeneous occupation of the defect levels. This is

supported by the observation of the double junction phenomenon, especially at high fluences (for more details see Sec. 5.4.1). Probably it is a combination of both, at least at higher fluences. In any case these complications show that the analysis methods commonly used are quite simplified. Only one single part of the curve, namely the kink at the depletion point, is analysed and only this one value for I and N_{eff} is used to characterise the whole diode. It has to be posed the question whether this is enough to fully describe the radiation damage of the whole detector. However, the N_{eff} obtained here via the depletion voltage can still be regarded as a relevant value and can be used for a first overview on the radiation damage. But one should keep in mind the limitations of this simple approach.

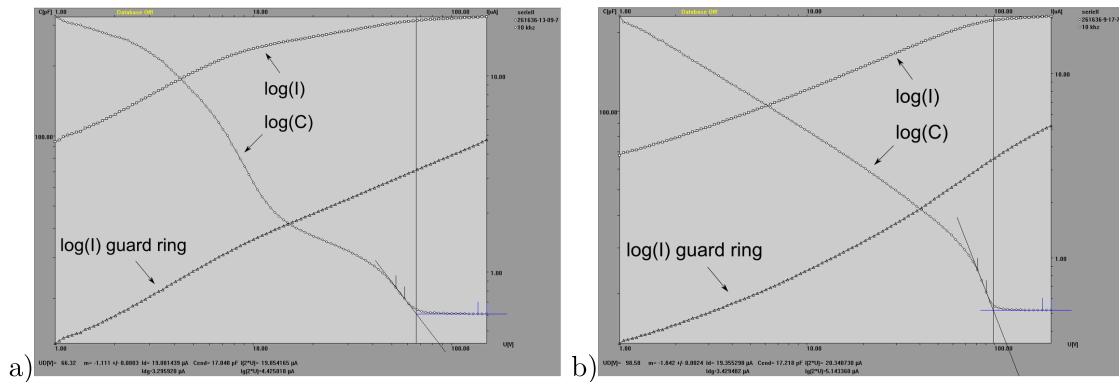

Figure 5.1: CV and IV characteristics in serial mode for a) EPI-ST $150 \mu m$, $\Phi_{eq} = 1 \times 10^{14} cm^{-2}$, $8 min$ at 80°C; b) EPI-DO $150 \mu m$, $\Phi_{eq} = 1 \times 10^{14} cm^{-2}$, $8 min$ at 80°C.

5.2 Reverse Current

Irradiation of Si detectors causes the introduction of deep-level defects in the band gap. These defects act as generation centres and result macroscopically in an increase in reverse current (see Sec. 3.4). If the current is normalised to the sensitive detector volume, the current-related radiation damage can be compared for different detector geometries.

5.2.1 Fluence Dependence of the Reverse Current

Fig. 5.2 shows the volume-normalised current at full depletion I_{dep}/V as a function of the equivalent fluence as determined by Al activation. The values are taken after $8 min$ annealing at 80°C. This is a commonly accepted reference point because it approximately coincides with the minimum of ΔN_{eff} (cf. [Mol99] and Sec. 5.3) and fluctuations of annealing due to irradiation and transport are minimised. The detector current before irradiation is negligible and thus did not need to be subtracted: In this work the minimum investigated fluence is $10^{14} cm^{-2}$ with a reverse current of a few μA compared to sub-nA before irradiation.

It can be seen that the normalised current is proportional to the equivalent fluence as shown by many investigations before. A linear fit yields the current damage parameter α which is displayed in Tab. 5.1 for the different materials and geometries. The overall fit gives $\alpha = (3.9 \pm 0.1) \times 10^{-17} Acm^{-1}$ if the less reliable values at the high fluence of $4 \times 10^{15} cm^{-2}$ are not taken into account and $\alpha = (4.3 \pm 0.1) \times 10^{-17} Acm^{-1}$ if they are included into the fit[1].

[1]The denoted uncertainties are the statistical errors of the fit only.

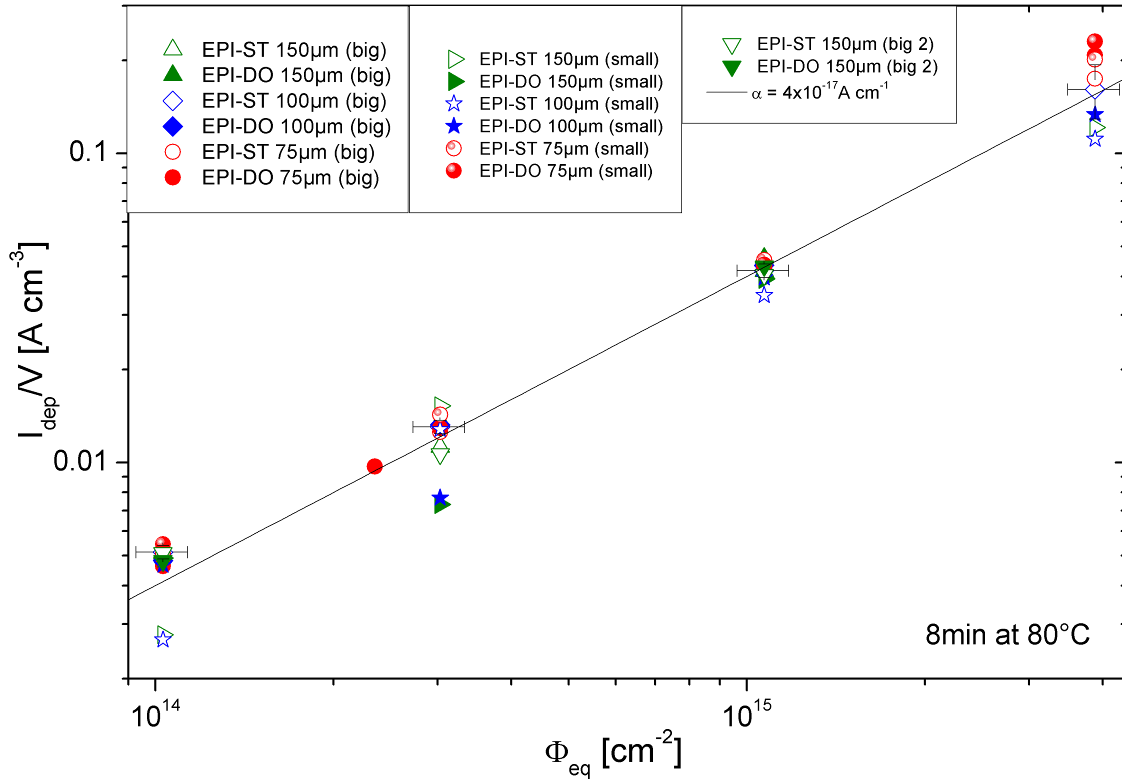

Figure 5.2: The reverse current normalised to the detector volume as a function of equivalent fluence after $8min$ annealing at 80°C. Different detector types and geometries are shown. The line is drawn with the reference slope of $\alpha = 4.0 \times 10^{-17} Acm^{-1}$. For clearness the errors are only shown exemplarily for EPI-ST $100\mu m$.

This result agrees well with the reference value of $\alpha = 4.0 \times 10^{-17} Acm^{-1}$ found by [Mol99]. The deviation is small and can be explained by the fluence uncertainty of about 10%. There is also no significant difference between the different material types and thicknesses observed. Although it seems that the current damage rate of EPI-DO exceeds the one of EPI-ST for all big diodes, this is opposite for most of the small diodes and the maximum deviation is with 10% in the same range as the reported fluence uncertainty. The difference between two sets of the same kind of diodes, e.g. EPI-DO $150\mu m$, is not less either.

These deviations already hint at a major problem of the $I/V(\Phi_{eq})$ curve. Although the global fit value for α is as expected, there is a large extent of scattering of the individual points around the fitted line. This is best to be seen from Fig. 5.3 where the current is not only normalised to the volume, but also divided by the fluence, which gives the individual damage parameter α for each point[2]. Especially the small diodes show a large deviation up to 40% from the mean value. For the low fluence values this is not easy to explain because, as already mentioned, in this range the CV and IV characteristics are well measurable so that also I_{dep} should have an uncertainty below 5%. The suspicion is that the fluence uncertainty is larger than expected so that the real fluence is different from the denoted one which was measured by Al activation spectroscopy. One reason could be for example that the proton

[2]Note that this parameter is similar to the proportionality constant α from the previous paragraph, but here it is no fit result but only the ratio $I/(V \cdot \Phi_{eq})$ of each single data point.

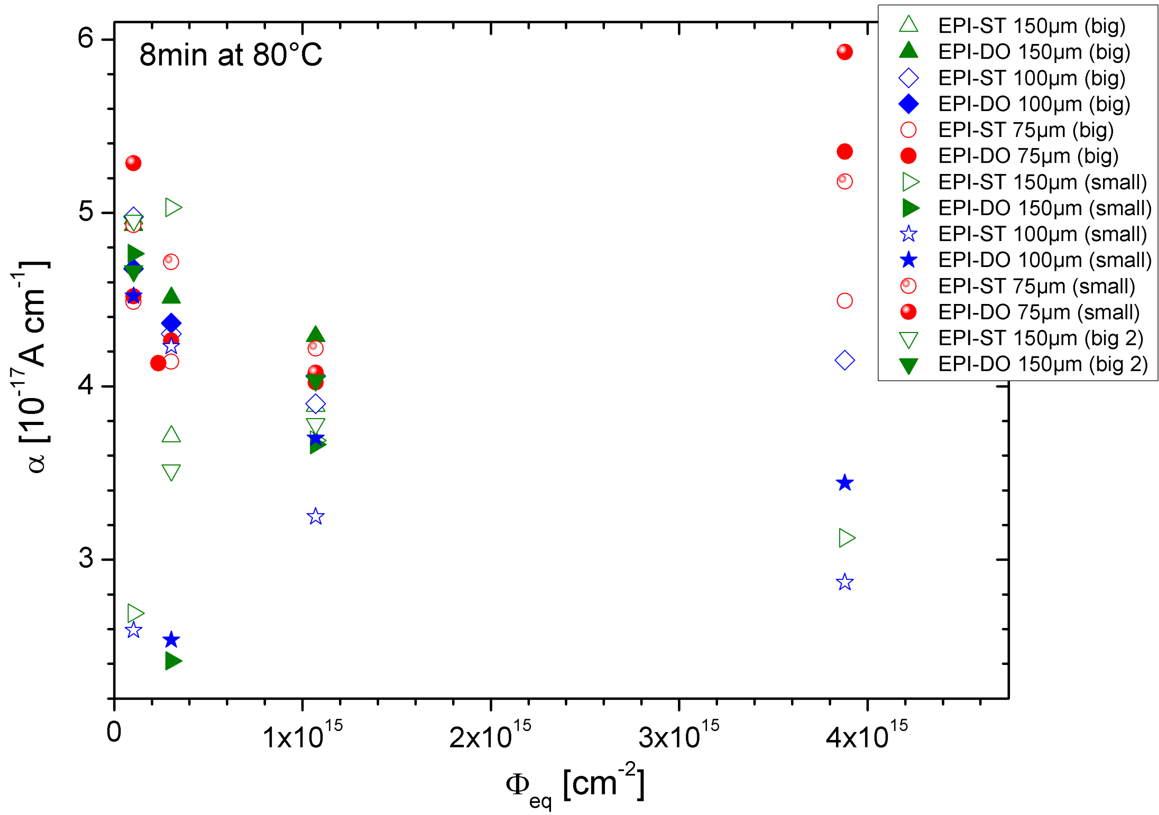

Figure 5.3: The individual current damage parameter α as a function of Φ_{eq}.

beam was more inhomogeneous during irradiation than thought. As already mentioned in Sec. 3.4 the linearity of $I/V(\Phi_{eq})$ is often reliably used for dosimetry. So it is possible to correct the denoted fluence values via the reference damage parameter $\alpha = 4.0 \times 10^{-17} Acm^{-1}$ and the measured normalised current[3]. The analysis of the U_{dep} respectively ΔN_{eff} fluence dependence in Sec. 5.3 supports that this is justified. The corrected fluence values are listed in Appendix A. However, for the high fluence value of $4 \times 10^{15} cm^{-2}$ the measurement of I_{dep} is also very uncertain so that its suitability for fluence determination is doubtful. In the next section there will be also more reasons given like self-annealing effects, which suggest that the current after $8min$ annealing should not be taken for the fluence correction of $4 \times 10^{15} cm^{-2}$. Therefore, in most of the following cases the α-normalised values will be only used for analysis for the diodes irradiated by fluences below $4 \times 10^{15} cm^{-2}$. For easy reference in the text, the simplified fluence notation as introduced in Tab. 4.2 will be kept.

5.2.2 Annealing Behaviour

The annealing of defects results in a change of the reverse current, which is dependent on annealing time t_a and temperature T_a. The annealing curves of the normalised current I_{dep}/V after heat treatment at 80°C are shown in Fig. 5.4. Each diagram contains the curves for the 6 different EPI materials at a certain fluence. Large annealing times of up to $92640 min$ were only performed for the big $75 \mu m$ diodes, the rest was only annealed up to $30 min$.

[3] The fluences corrected in such a way will be also referred to as *α-normalised fluences*.

	α $[10^{-17}Acm^{-1}]$					
Material	ST 150μm	DO 150μm	ST 100μm	DO 100μm	ST 75μm	DO 75μm
big 1	3.88 $\pm$ 0.08	4.31 $\pm$ 0.06	3.94 $\pm$ 0.10	4.09 $\pm$ 0.07	4.04 $\pm$ 0.04	4.05 $\pm$ 0.04
big 2	3.77 $\pm$ 0.09	4.04 $\pm$ 0.06				
small	3.78 $\pm$ 0.26	3.58 $\pm$ 0.24	3.32 $\pm$ 0.19	3.62 $\pm$ 0.22	4.26 $\pm$ 0.10	4.09 $\pm$ 0.12
combined excl. $4 \times 10^{15}cm^{-2}$	3.91$\pm$0.05					
combined incl. $4 \times 10^{15}cm^{-2}$	4.27$\pm$0.14					

Table 5.1: The current damage parameter α after $8min$ annealing at 80°C for different materials and geometries. If not stated otherwise the fit excludes the high fluence value of $4 \times 10^{15}cm^{-2}$. The error is the statistical error of the fit only.

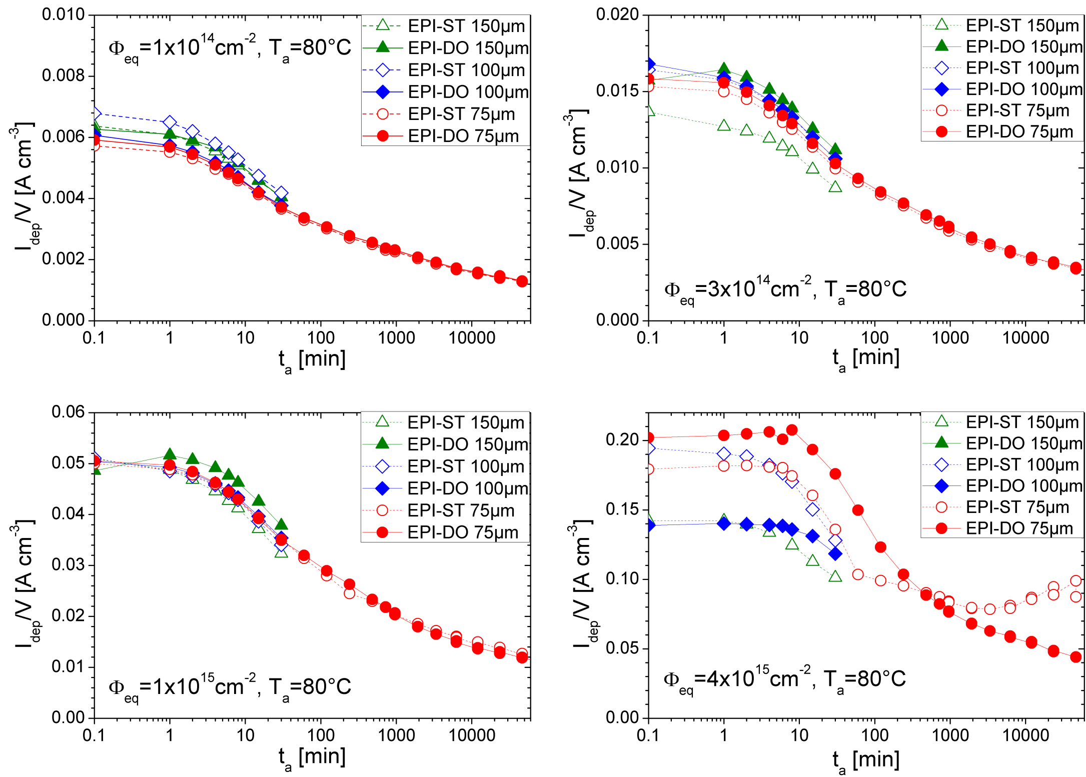

Figure 5.4: Annealing behaviour of the normalised current I_{dep}/V at different fluences. Note the changing scale of the y-axis.

Apart from an approximately constant shift in y-direction due to the already above discussed supposed fluence fluctuations, the individual curves show nearly the same behaviour and no difference between ST and DO or different thicknesses can be observed. The reverse current decreases steadily with increasing annealing time. If the normalised current is divided by the fluence, i.e. if the damage parameter α is considered as displayed in Fig. 5.5 for the $75\mu m$ diodes, it can be seen that the current annealing is also independent of fluence. Only the curves for the high fluence of $4 \times 10^{15}cm^{-2}$ deviate in certain points: There seems to be a flat slope at the beginning and the α values at short annealing times are larger than expected. Moreover, for the high fluence of EPI-ST $75\mu m$ there is first a slowing down of the decrease and later even a re-increase at large annealing times, which coincides with the type inversion

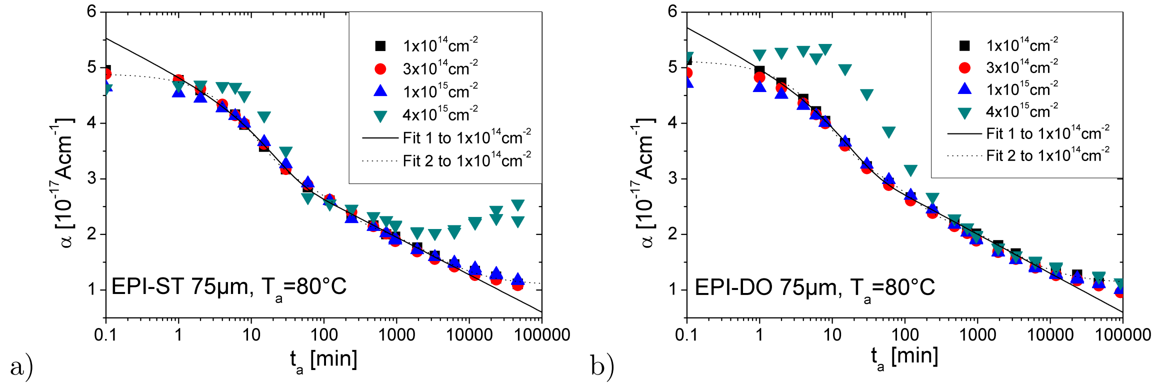

Figure 5.5: Annealing behaviour of the current damage constant α for EPI-ST 75μm (a) and EPI-DO 75μm (b). The lines are fits to the data according to Eq. 5.1 (straight line, fit range: 1min-3360min) and Eq. 5.2 (dotted line, whole fit range). At late annealing times and large fluences the bistable effect is observed, especially for ST $4 \times 10^{15} cm^{-2}$, i.e. that measurements directly after annealing (upper values) and after 24h storage in the dark (lower values) give different results. For more details see [Mol95]. For further analysis, only the values after 24h in the dark were taken into account.

point (see Sec. 5.3). This shows that, as usual, special caution is needed for the analysis of this high fluence. A possible explanation can be given when considering the effects of current breakthrough, self-annealing and U_{dep} annealing behaviour as proposed in the following.

On the one hand irradiations by $4 \times 10^{15} cm^{-2}$ take a very long time (almost 2 weeks at room temperature) so that self-annealing effects can occur already during irradiation. However, it is not straight-forward to account for self-annealing effects quantitatively. One cannot simply take the whole irradiation duration because the irradiation is a steady process. This means that during irradiation at the same time new defects are created and earlier created defects anneal out.

On the other hand there is again the problem of diode breakthrough because the depletion voltage and therefore also the electric field are so large at high fluence. This leads to a distortion of the reverse current so that the α value is higher than expected at short annealing times. But due to annealing both the current and the depletion voltage decrease at a certain point so that at later annealing times no breakthrough problems occur anymore. It can be nicely seen for EPI-DO 75μm that the $4 \times 10^{15} cm^{-2}$ curve joins the ones of the other fluences at 480min. Also the $4 \times 10^{15} cm^{-2}$ curve of EPI-ST 75μm reaches for a short time the other fluences before deviating again. In that case the re-increase later can be explained by the fact that the diode type-inverts between 60min and 120min and U_{dep} rises again so high that the increasing electric field leads again to diode breakthrough.

For the successfully measured fluences it was tried to find a model that fits the annealing curve data well. Because of the limited annealing times up to only 30min for the other diodes, this could be only done for the 75μm detectors. A commonly used function for the description of the current annealing reads

$$\alpha(t_a) = \alpha_1 exp\left(-\frac{t_a}{\tau_1}\right) + \alpha_0 - \beta \ln\left(\frac{t_a}{t_0}\right) \tag{5.1}$$

with t_0 usually set to 1min [Mol99]. Thus in this parameterisation the annealing is described

by an exponential decay related to a first-order process, a constant damage parameter α_0 and a logarithmic term. The latter one is only semi-empirical and it is not claimed to be based on a physical model. But a similar behaviour is found for the annealing of trapped oxide charge in SiO_2 layers and so far the data has been mostly fitted well by this model. However, it can be seen from Fig. 5.5 that here this function might be a good approximation in the time range between $1min$ and about $5000min$ but fails to describe the data below $1min$ and at late annealing times. This had to be expected because the logarithmic function diverges below $1min$ and grows monotonically at late times so that α will become negative eventually, which is unphysical. Instead, it can be observed that α seems to saturate at late annealing times so that another model is needed. Nevertheless, as most of the previous studies used to work with this parameterisation, the extracted parameters from a fit using this function are listed in Tab. 5.2. It should be noted that in addition to the listed statistical fit errors there are also additional uncertainties due to the chosen fit range, which are in the same order. No big differences between ST and DO and between the different fluences can be seen except for the deviation of $1 \times 10^{15} cm^{-2}$, especially with respect to τ_1. This is probably again due to self-annealing effects as one can see from Fig. 5.5 that for short annealing times the curve of this fluence is left of the ones of lower fluences. After a naive self-annealing correction assuming additional $3min$ of annealing the parameters agree much better with the ones of lower fluences. To avoid those uncertainties, the combined fit includes the data of $1 \times 10^{14} cm^{-2}$ and $3 \times 10^{14} cm^{-2}$ only, but for both ST and DO. The results $\alpha_0 = (4.10 \pm 0.04) \times 10^{-17} Acm^{-1}$ and $\beta = (0.31 \pm 0.01) \times 10^{-17} Acm^{-1}$ agree within 10% with the values from [Mol99] and [Sch03], but $\alpha_1 = (0.82 \pm 0.04) \times 10^{-17} Acm^{-1}$ is about 30% lower. $\tau_1 = 19.44 \pm 1.46$ is about two times the value of [Mol99], but the deviation from the result of [Sch03] is less.

Material	Φ_{eq} $[10^{14} cm^{-2}]$	α_0 $[10^{-17} Acm^{-1}]$	α_1 $[10^{-17} Acm^{-1}]$	τ_1 $[min]$	β $[10^{-17} Acm^{-1}]$
EPI-ST 75μm	1	3.97 ± 0.06	0.89 ± 0.06	20.63 ± 1.83	0.29 ± 0.01
	3	4.14 ± 0.07	0.74 ± 0.07	20.92 ± 2.75	0.32 ± 0.01
	10	3.72 ± 0.12	0.93 ± 0.11	47.18 ± 5.86	0.26 ± 0.02
EPI-DO 75μm	1	4.11 ± 0.05	0.91 ± 0.05	17.02 ± 1.24	0.31 ± 0.01
	3	4.13 ± 0.06	0.79 ± 0.06	19.47 ± 1.97	0.32 ± 0.01
	10	4.24 ± 0.13	0.53 ± 0.12	34.87 ± 9.18	0.33 ± 0.02
	10 (3min self-ann.)	4.46 ± 0.04	0.91 ± 0.04	14.49 ± 1.35	0.37 ± 0.01
Combined		4.10 ± 0.04	0.82 ± 0.04	19.44 ± 1.46	0.31 ± 0.01
[Mol99] 300μm		4.23	1.13	9	0.28
[Sch03] 50μm		4.14	1.27	14.78	0.28

Table 5.2: Current annealing parameters extracted from the fit according to Eq. 5.1. The combined fit includes the data of $1 \times 10^{14} cm^{-2}$ and $3 \times 10^{14} cm^{-2}$ only, but for both ST and DO. For comparison the results from previous works have been added. The fit range was $1min$-$3360min$.

It was found that an alternative description given by the sum of two first-order processes, a stable part and a second-order process fits the data much better:

$$\alpha'(t_a) = \alpha'_0 + \alpha'_1 exp\left(-\frac{t_a}{\tau'_1}\right) + \alpha'_2 exp\left(-\frac{t_a}{\tau'_2}\right) + \alpha'_3 \frac{1}{1 + \frac{t_a}{\tau'_3}}. \tag{5.2}$$

This function can also account for the saturation behaviour below $1min$ and at late annealing times because $\alpha'(t_a = 0) = \sum_i \alpha'_i$ and $\alpha'(t_a \to \infty) = \alpha'_0$. The results of the fit are shown in Tab. 5.3. However, for a real second-order process one would expect that the time constant

Material	Φ_{eq} $[10^{14}cm^{-2}]$	α'_0 $[10^{-17}Acm^{-1}]$	α'_1 $[10^{-17}Acm^{-1}]$	τ'_1 $[min]$	α'_2 $[10^{-17}Acm^{-1}]$	τ'_2 $[min]$
EPI-ST 75μm	1	1.09 ± 0.03	1.62 ± 0.09	9.85 ± 0.85	1.02 ± 0.09	118 ± 21
	3	1.09 ± 0.03	1.71 ± 0.07	11.72 ± 0.90	0.93 ± 0.09	176 ± 39
	10	1.19 ± 0.02	1.15 ± 0.11	12.29 ± 1.54	1.17 ± 0.10	96 ± 16
EPI-DO 75μm	1	1.12 ± 0.03	1.67 ± 0.08	8.60 ± 0.71	1.06 ± 0.08	104 ± 18
	3	0.99 ± 0.03	1.73 ± 0.08	11.26 ± 0.99	0.99 ± 0.09	170 ± 36
	10	1.04 ± 0.03	1.54 ± 0.07	14.01 ± 1.13	0.99 ± 0.09	234 ± 48

Material	Φ_{eq} $[10^{14}cm^{-2}]$	α'_3 $[10^{-17}Acm^{-1}]$	τ'_3 $[min]$
EPI-ST 75μm	1	1.21 ± 0.05	2546 ± 489
	3	1.17 ± 0.08	2224 ± 559
	10	1.13 ± 0.05	1854 ± 324
EPI-DO 75μm	1	1.27 ± 0.05	2376 ± 417
	3	1.22 ± 0.07	3015 ± 664
	10	1.16 ± 0.09	2713 ± 660

Table 5.3: Current annealing parameters extracted from the fit according to Eq. 5.2.

is inversely proportional to the defect concentration (cf. Eq. 3.12). In a first approximation the defect generation should be proportional to the fluence so the expectation is $\tau_3 \propto 1/\Phi_{eq}$. This is not fulfilled at all. For ST material, τ_3 is indeed decreasing with fluence, but much too little (starting from $\tau_3 = 2546min$ for $1 \times 10^{14}cm^{-2}$, τ_3 should decrease to one tenth of this value for $1 \times 10^{15}cm^{-2}$, but it is still $1854min$). For DO there is no such trend visible at all. Such a problem that the fit is best when using a second-order approach but the related time constant behaves like for a first-order process is already known for the reverse annealing of N_{eff} for FZ and Cz (see [Mol99]). In that case a pragmatic approach had been adopted, i.e. the second-order function was used for the fit, but one should be aware that the underlying physical process is probably of first order with a so-far unknown other effect interfering.

5.3 Development of U_{dep} and N_{eff}

5.3.1 Overview

Radiation-induced defect levels do not only result in an increased reverse current, but also affect the effective doping concentration and therefore the depletion voltage of the detector. Recall that according to Eq. 2.5 $U_{dep} \propto |N_{eff}|d^2$. The depletion voltage is a very important detector parameter that determines the operability so that in this overview section the dependence of U_{dep} on fluence and annealing time is presented. However, in order to understand the underlying physical processes of radiation damage, it is more instructive to look at $N_{eff} = N_D - N_A$ so that a later detailed analysis will concentrate on that parameter.ability so that in this overview section the dependence of U_{dep} on fluence and annealing time is presented. However, in order to understand the underlying physical processes of radiation damage, it is more instructive to look at $N_{eff} = N_D - N_A$ so that a later detailed analysis will concentrate on that parameter.

Fig. 5.6 shows the U_{dep} annealing curves for all different materials at certain fluences. The typical development is as follows: Directly after irradiation the depletion voltage rises up to a maximum at about $8min$ before it decreases again. Thus, the annealing behaviour

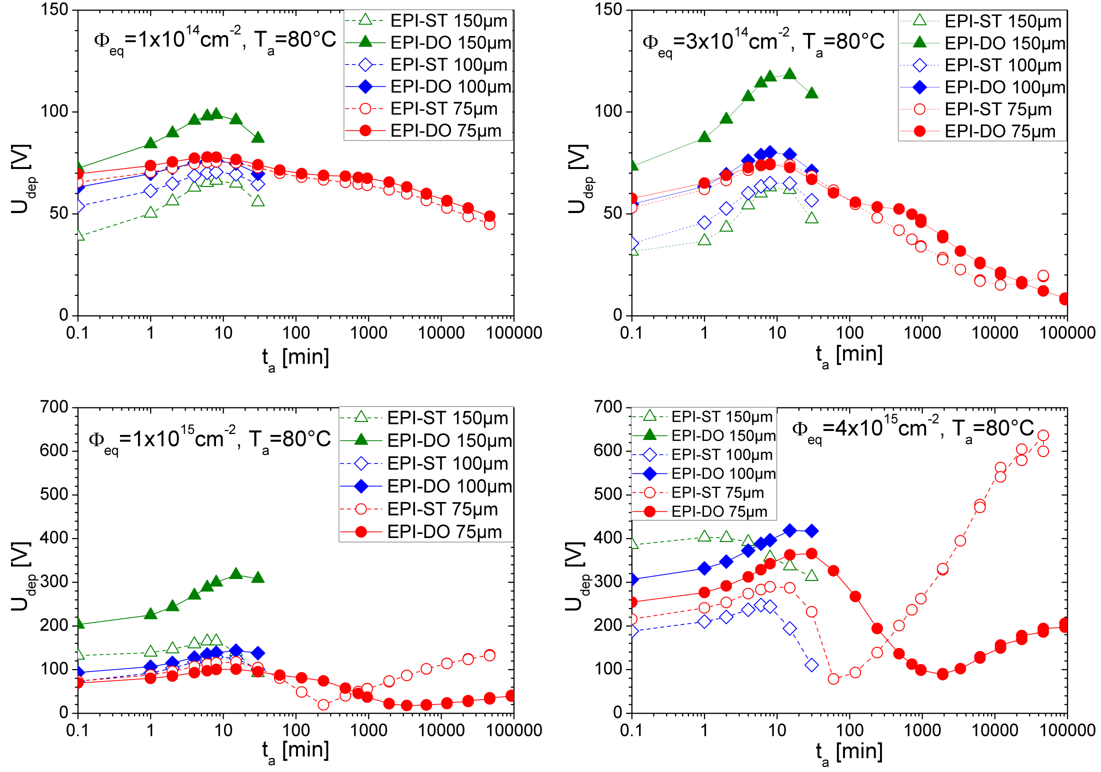

Figure 5.6: U_{dep} annealing curves at different fluences. Note the different y-scales. Like in Fig. 5.5, the bistable effect can be observed, but only the lower values after 24h in the dark will be taken into account in the following.

can be subdivided into a *short-term annealing*, a *stable damage* component[4] and a *long-term annealing*. From previous investigations it is known that the short-term annealing is dominated by an increase in N_{eff} due to an out-annealing of radiation-induced acceptors. This results in an increase of U_{dep} for non-inverted diodes (the positive N_{eff} becomes more positive) and in a decrease of U_{dep} for inverted diodes[5] (the negative N_{eff} becomes less negative so that $|N_{eff}|$ decreases). In contrast, the long-term annealing is known to be governed by a decrease in N_{eff} due to the creation of acceptor-like defect complexes. Thus the effect is a decrease of U_{dep} for non-inverted diodes and an increase of U_{dep} for inverted detectors[6]. To conclude, the here observed shape of the annealing curves clearly indicates that none of the here investigated diodes have undergone type inversion during irradiation up to a fluence of $4 \times 10^{15} cm^{-2}$. This is mostly also confirmed by the TCT current pulse shapes (see Sec. 5.4.1). However, the re-increase of U_{dep} at late annealing times for $75\mu m$ diodes at a fluence of $1 \times 10^{15} cm^{-2}$ and $4 \times 10^{15} cm^{-2}$ indicates that these diodes type-invert during annealing. It can be observed that the standard material undergoes inversion earlier than the oxygen-enriched one.

The maximum of the annealing curve is mostly to be found at $8min$. Therefore this point is regarded as especially characteristic for the description of the radiation damage. It is the best approximation for the stable damage if a fit of the whole curve is impossible, e.g.

[4]The stable damage is the part of the radiation damage that does not change with annealing time.
[5]This is why the short-term annealing is also known as *beneficial annealing*.
[6]Because of this the long-term annealing is also called *reverse annealing*.

like in this case for the $100\mu m$ and $150\mu m$ which were only annealed up to $30min$. The stable damage is independent of annealing time and therefore the most important damage component. However, for higher fluences it can also occur that the maximum is delayed, e.g. to $15min$ or sometimes even to $30min$. This happens more often for the oxygen-rich materials, but a reason for this behaviour is not known yet. Again one should be aware of possible self-annealing effects, but correcting for them would even lead to a further delay as it would shift the curve to the right. However, despite of this possible change in the maximum, the value at $8min$ is still regarded to be best for a description of the stable radiation-induced damage.

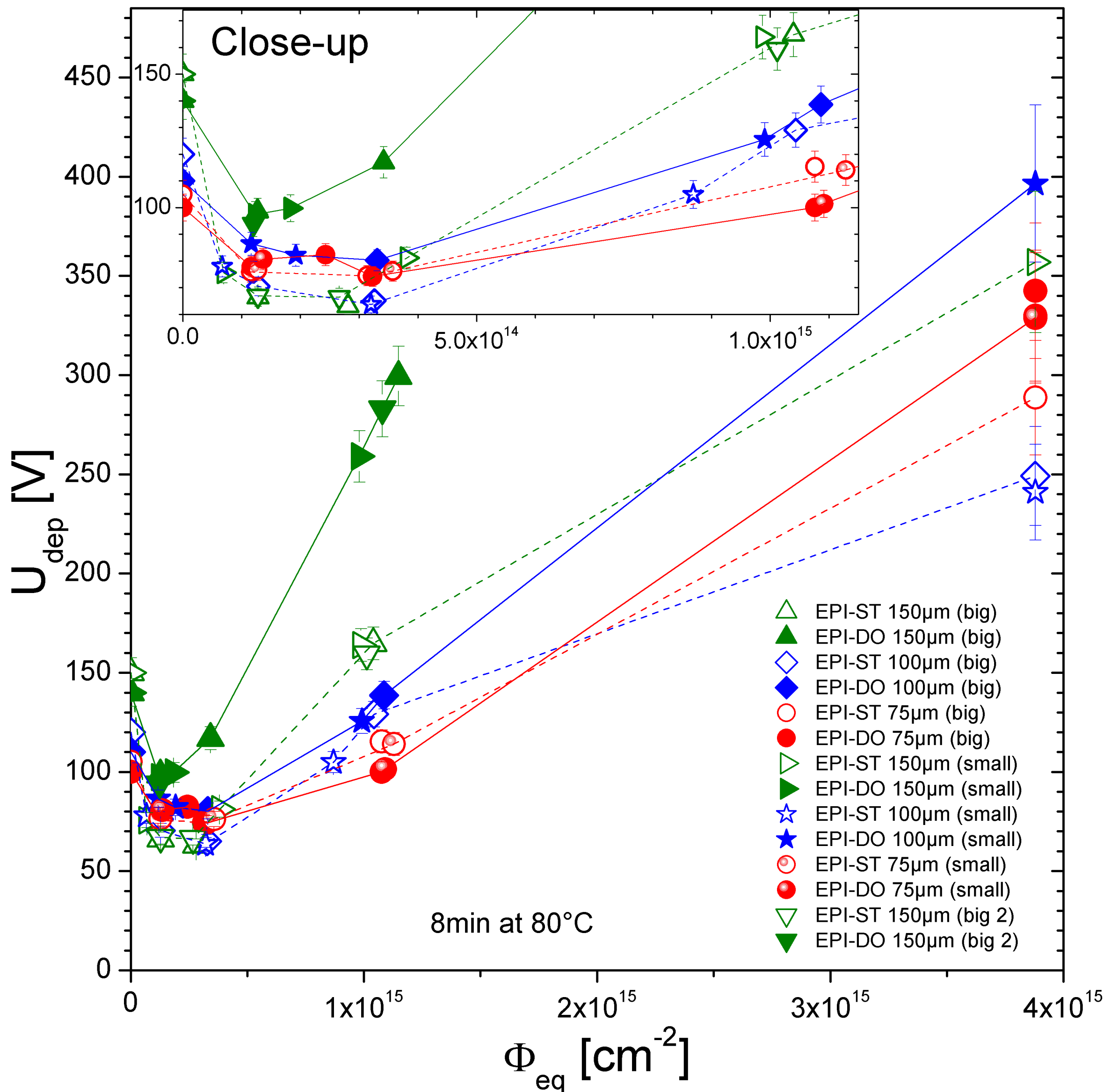

Figure 5.7: Depletion voltage after $8min$ at 80°C annealing. Up to $1 \times 10^{15} cm^{-2}$ the α-normalised fluence was used, but for $4 \times 10^{15} cm^{-2}$ the value from Al activation was taken.

Fig. 5.7 shows the depletion voltage after $8min$ annealing as a function of fluence. All diode types show the same general behaviour: A drop for small fluences, which can be ex-

plained by donor removal, and an increase for larger fluences due to donor creation (for a detailed discussion see next section). The relative position of data points that belong to the same material and thickness, but to different sets of diodes (e.g. small and big) encourages that it was justified to α-normalise the fluence. As explained in Sec. 5.2.1, this re-determination has been done up to $1 \times 10^{15} cm^{-2}$ and it can be seen that now all data points fit in nicely and lie on a smooth curve.

From considering the thickness alone, one would expect the depletion voltage to be always highest for the $150\mu m$ detectors and lowest for the $75\mu m$ ones. But the development of U_{dep} depends also on other parameters, especially the initial doping concentration and the oxygen concentration. As some of these parameters lead to interfering effects, it is difficult to see clear trends except that EPI-DO $150\mu m$ has always the highest U_{dep} (also at $4 \times 10^{15} cm^{-2}$ if extrapolated). It is easier to look at the change in N_{eff} first, which will be done in the following paragraph, before returning to the depletion voltage at the end of this section.

5.3.2 ΔN_{eff} at 8min - Stable Damage

$\Delta N_{eff}(\Phi_{eq}, t_a) = N_{eff,0} - N_{eff}(\Phi_{eq}, t_a)$ describes the radiation-induced change in the effective doping concentration. The respective values after $8min$ annealing, denoted as $\Delta N_{eff,C}$, were obtained according to Eq. 2.5 from the U_{dep} values in Fig. 5.7[7]. They approximately represent the stable damage and are shown in Fig. 5.8. The advantage of using ΔN_{eff} instead of U_{dep} is that interfering effects like the different thicknesses are excluded and one can concentrate on the radiation-induced changes. A parameterisation of the stable damage component can be given by

$$\Delta N_{eff,C} = N_{C,0}\,(1 - \exp(-c\Phi_{eq})) + g_C \Phi_{eq}. \tag{5.3}$$

The first term describes an incomplete donor removal with $N_{C,0} \leq N_{eff,0}$ being the removable doping concentration and c being the so-called removal constant that describes the removal velocity[8]. The second term represents a fluence-proportional introduction of space charge. $g_C = g_{C,A} - g_{C,D}$ is an effective introduction rate, i.e. the difference between donor and acceptor introduction rate. If g_C is positive, mostly acceptors are created, if it is negative then predominantly donors are introduced.

The data was fitted according to this parameterisation. However, like in the previous section for the leakage current it has to be emphasised also here that the data for $4 \times 10^{15} cm^{-2}$ is very uncertain, especially the fluence. Unfortunately, this is exactly the point which has a high influence on the fit, particularly on the parameter g_C. Different fitting modes were tried like including or excluding $4 \times 10^{15} cm^{-2}$ and using the fluence values from either Al activation or after α-normalisation. Because of these uncertainties the error is probably higher than the statistical error of the fit which is shown here. In order to reduce the uncertainties and especially to reduce the high dependence on the badly-measurable $4 \times 10^{15} cm^{-2}$ fluence point it would be highly desirable to have more intermediate data points, especially around $7 \times 10^{14} cm^{-2}$ and between $1 \times 10^{15} cm^{-2}$ and $4 \times 10^{15} cm^{-2}$. This is already planned for the next irradiation campaign. Until then, in order to improve the number of data points here, all available diodes of the same material were joined together, i.e. both small and big ones and if available even a second set of them.

[7] The uncertainties were determined according to Gaussian error propagation with the U_{dep} uncertainties as specified in Sec. 5.1, assumed 3% thickness uncertainty and 2% error in $N_{eff,0}$.

[8] After $\Phi_{eq} = 1/c$ the initial doping concentration is reduced by $(1 - 1/e)N_{C,0}$.

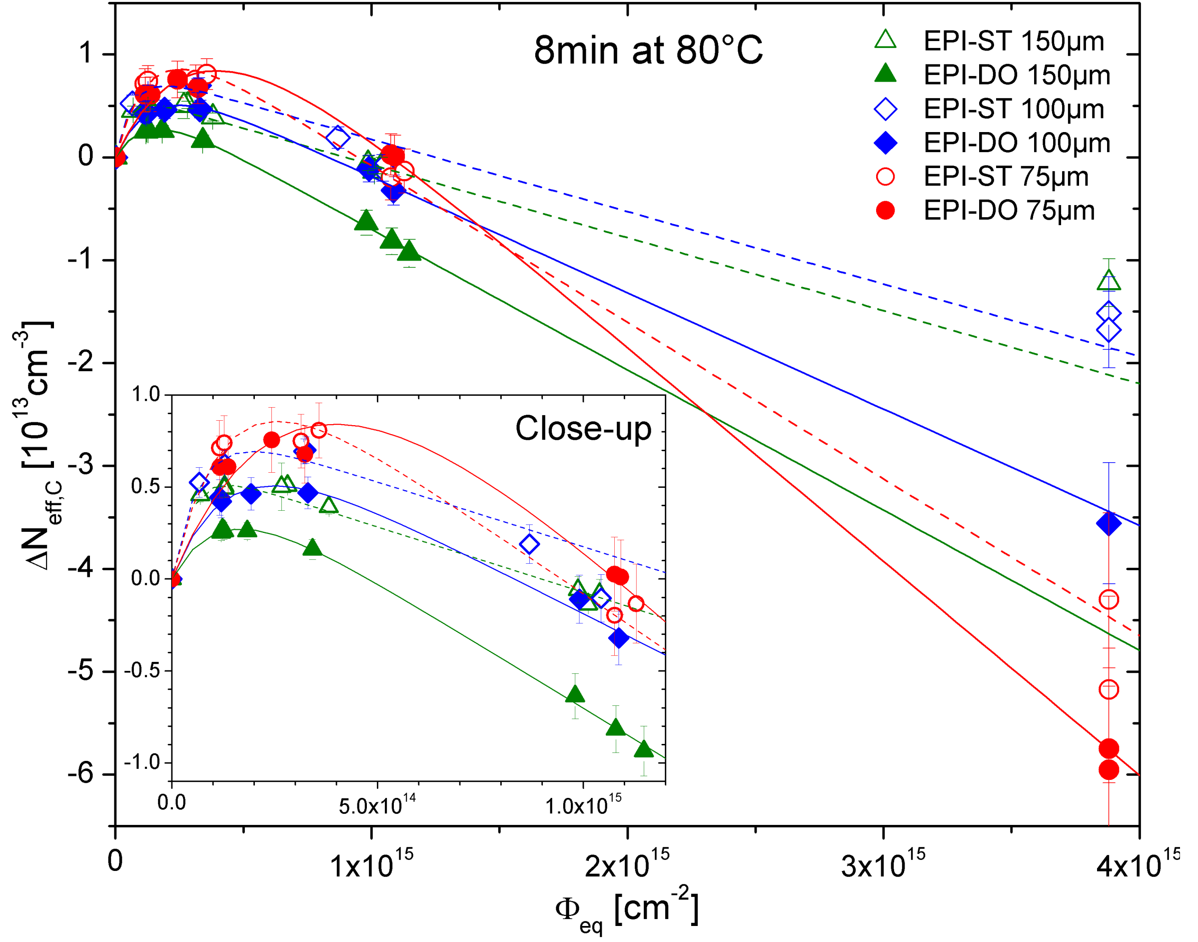

Figure 5.8: The radiation-induced change in the effective doping concentration at $8min$ at 80°C as a function of fluence (corresponds approximately to the stable damage component) with fits according to Eq. 5.3. The fluence up to $1 \times 10^{15} cm^{-2}$ was corrected according to the reverse current, but for $4 \times 10^{15} cm^{-2}$ the value from Al spectroscopy was taken.

However, it turned out that the general trends which will be explained in the following are observed for any of the used fitting modes. The results presented here are from an error-weighted fit[9] that uses the α-normalised fluence values up to $1 \times 10^{15} cm^{-2}$ and the fluence from Al activation for $4 \times 10^{15} cm^{-2}$ as seen in Fig. 5.8. The results are shown in Tab. 5.4 and Fig. 5.9 with the statistical errors from the fit. It is especially interesting to study how they change with respect to material properties. Consequently, in Fig. 5.9 the different materials are arranged in such a way that the average oxygen concentration is increasing from the left to the right. On the left there are the low-oxygen standard materials, starting from the thick $150\mu m$ diodes going to the thin $75\mu m$ ones, and on the right there are the oxygen-enriched materials.

First of all, it can be seen that for all epitaxial materials investigated here the introduc-

[9]The fits performed here are according to the standard least-squares method. If the error is considered as weight, the sum of the squared deviations between data points y_i and fit function $f(x_i, a_k)$ is calculated as $\chi^2 = \sum_i \frac{1}{\sigma_{y_i}^2}[y_i - f(x_i, a_k)]^2$, where σ_{y_i} are the errors of y_i and a_k are the free parameters of the fit.

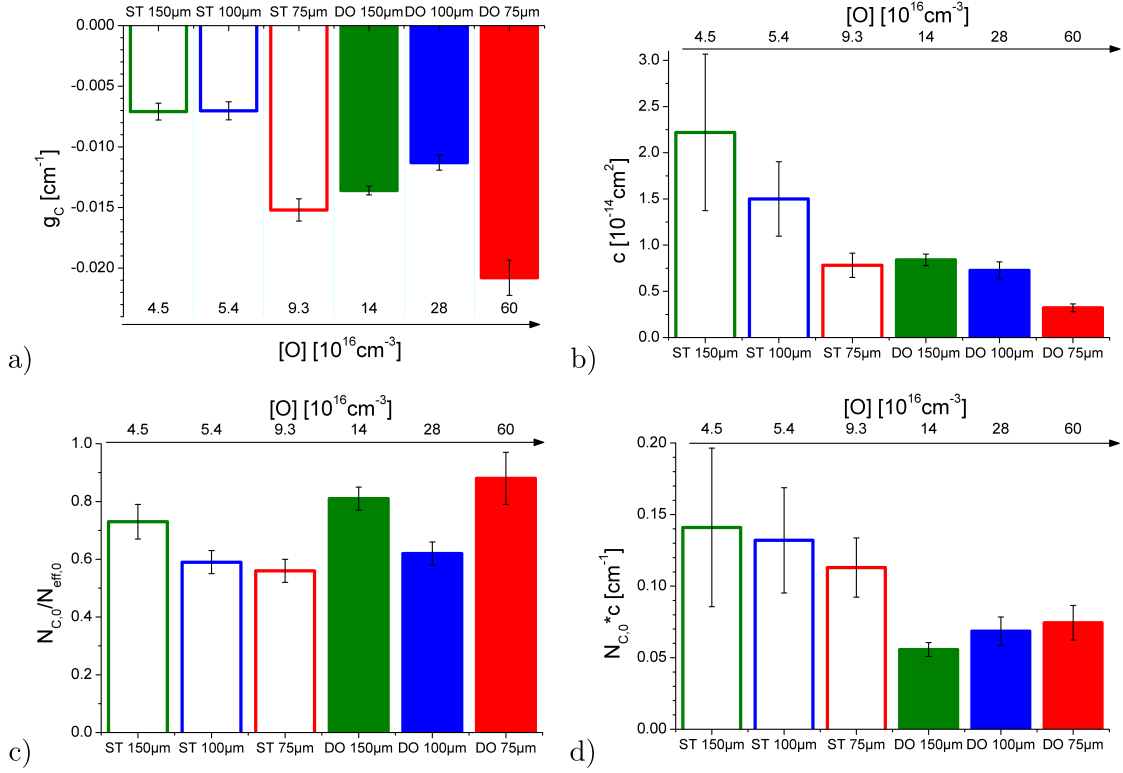

Figure 5.9: The results from the fit to $\Delta N_{eff,C}(\Phi_{eq})$. a) The introduction rate g_C, b) the removal constant c, c) the removed donor fraction $\frac{N_{C,0}}{N_{eff,0}}$, d) the initial donor removal rate $N_{C,0} \cdot c$. The different materials are arranged in such a way that the average oxygen concentration is increasing from the left to the right.

Material	$N_{eff,0}$ $[10^{12}cm^{-3}]$	[O] $[10^{16}cm^{-3}]$	$N_{C,0}$ $[10^{12}cm^{-3}]$	c $[10^{-14}cm^{-2}]$	g_C $[10^{-2}cm^{-1}]$	$\frac{N_{C,0}}{N_{eff,0}}$	$N_{C,0} \cdot c$ $[10^{-2}cm^{-1}]$
ST 150μm	8.75	4.5	6.4 ± 0.6	2.22 ± 0.85	-0.71 ± 0.07	0.73 ± 0.06	14.1 ± 5.5
DO 150μm	8.17	14	6.6 ± 0.3	0.84 ± 0.06	-1.36 ± 0.04	0.81 ± 0.04	5.6 ± 0.5
ST 100μm	15.00	5.4	8.8 ± 0.7	1.50 ± 0.40	-0.70 ± 0.07	0.59 ± 0.04	13.2 ± 3.7
DO 100μm	15.14	28	9.4 ± 0.7	0.73 ± 0.09	-1.13 ± 0.06	0.62 ± 0.04	6.9 ± 1.0
ST 75μm	25.82	9.3	14.4 ± 1.1	0.78 ± 0.13	-1.52 ± 0.09	0.56 ± 0.04	11.3 ± 2.1
DO 75μm	26.17	60	23.1 ± 2.2	0.32 ± 0.04	-2.08 ± 0.15	0.88 ± 0.09	7.4 ± 1.2

Table 5.4: The results from a weighted fit to $\Delta N_{eff,C}(\Phi_{eq})$ using the α-normalised fluence up to $1 \times 10^{15}cm^{-2}$ and the fluence from Al activation for $4 \times 10^{15}cm^{-2}$.

tion rate g_C is negative ranging from -0.007 ± 0.001 for EPI-ST 150μm to -0.021 ± 0.002 for EPI-DO 75μm. This means that the stable damage for high fluences is dominated by donor generation. This is in contrast to FZ and even DOFZ material where g_C is positive (predominant acceptor generation), but has been observed before for Cz and thinner epitaxial material [Lin06b]. There it has also been reported that the absolute value of g_C is increasing with decreasing thickness. This was attributed to a higher oxygen concentration in thinner material, leading to an enhanced shallow donor creation and to a further suppression of acceptor generation (see Sec. 3.6.1). Here on first sight, g_C is not strictly monotonically increasing with increasing oxygen content, although the overall trend leads in this direction. However, one should be aware that the denoted oxygen concentration is just a mean value of an inhomogeneous density distribution (see Fig. 4.1) so that there might be effects arising

from this inhomogeneity. Also, part of the donor creation is supposed to be related to oxygen dimers whose density distribution can differ from the one of single oxygen. Moreover, there might be other differences due to the different thicknesses, which interfere. For example the initial doping concentration varies with thickness. Thus it is most instructive to compare the results from ST and DO material of the same thickness in order to exclude such effects. In this case, it becomes clearly visible that the donor introduction rate is higher for oxygen-enriched material than for standard one as expected.

The removal constant c is a measure of how fast the donor removal takes place and is displayed in Fig. 5.9 b). Apart from a very small deviation, the removal constant decreases for increasing [O], which becomes even clearer if one compares ST and DO material of the same thickness. A possible explanation for the delayed donor removal of DO might be that the oxygen acts as a sink for vacancies, i.e. that e.g. the reaction $V + O \rightarrow VO$ takes vacancies away and therefore suppresses the reaction $V + P \rightarrow VP$ to a certain extent.

The results for the removable fraction of the initial doping concentration, $N_{C,0}/N_{eff,0}$, are displayed in Fig. 5.9 d) with values ranging from 0.56 ± 0.04 to 0.88 ± 0.09. It is not known yet why there is only a partial doping removal taking place, but the values obtained here are already higher than found before (e.g. 0.35 for $50\mu m$ Epi diodes according to [Sch03]). Also here a slight difference between ST and DO is observed with $N_{C,0}/N_{eff,0}$ being a bit larger for DO, but this is statistically not very significant.

If the removal constant is multiplied with the removable doping concentration $N_{C,0}$, one obtains the initial donor removal rate[10] which is shown in Fig. 5.9 d). Earlier investigations after neutron irradiation have revealed a not-understood reciprocal dependence of c on $N_{C,0}$, i.e. that $N_{C,0} \cdot c$ was measured to be approximately constant [Mol99]. Within the errors this is also observed here, but only for ST and DO separately. Comparing ST and DO material, it can be seen that $N_{C,0} \cdot c$ is higher for ST than for DO because of the large difference between ST and DO in c.

5.3.3 Full Annealing Analysis according to the Hamburg Model for $75\mu m$ Diodes

In contrast to the thicker diodes, which were only annealed up to $30 min$, the big $75\mu m$ detectors were annealed up to $46560 min$ or some even to $92640 min$. Therefore an analysis of the full annealing process could be performed.

The Hamburg Model

A description of the annealing behaviour of irradiated diodes is provided by the so-called Hamburg model. As already mentioned above, the change in N_{eff}, which is dependent on Φ_{eq} and annealing time t_a, can be decomposed into the three parts short-term annealing N_A, stable damage N_C and long-term annealing N_Y:

$$\begin{aligned} \Delta N_{eff}(\Phi_{eq}, t_a) &= N_{eff,0} - N_{eff}(\Phi_{eq}, t_a) &(5.4)\\ &= N_A(\Phi_{eq}, t_a) + N_C(\Phi_{eq}) + N_Y(\Phi_{eq}, t_a). &(5.5)\end{aligned}$$

[10]For low fluences Eq. 5.3 can be simplified to $\Delta N_{eff,C} = N_{C,0} \cdot c\Phi_{eq} + g_C \Phi_{eq}$ so that $N_{C,0} \cdot c$ is obviously the donor removal rate at low fluences.

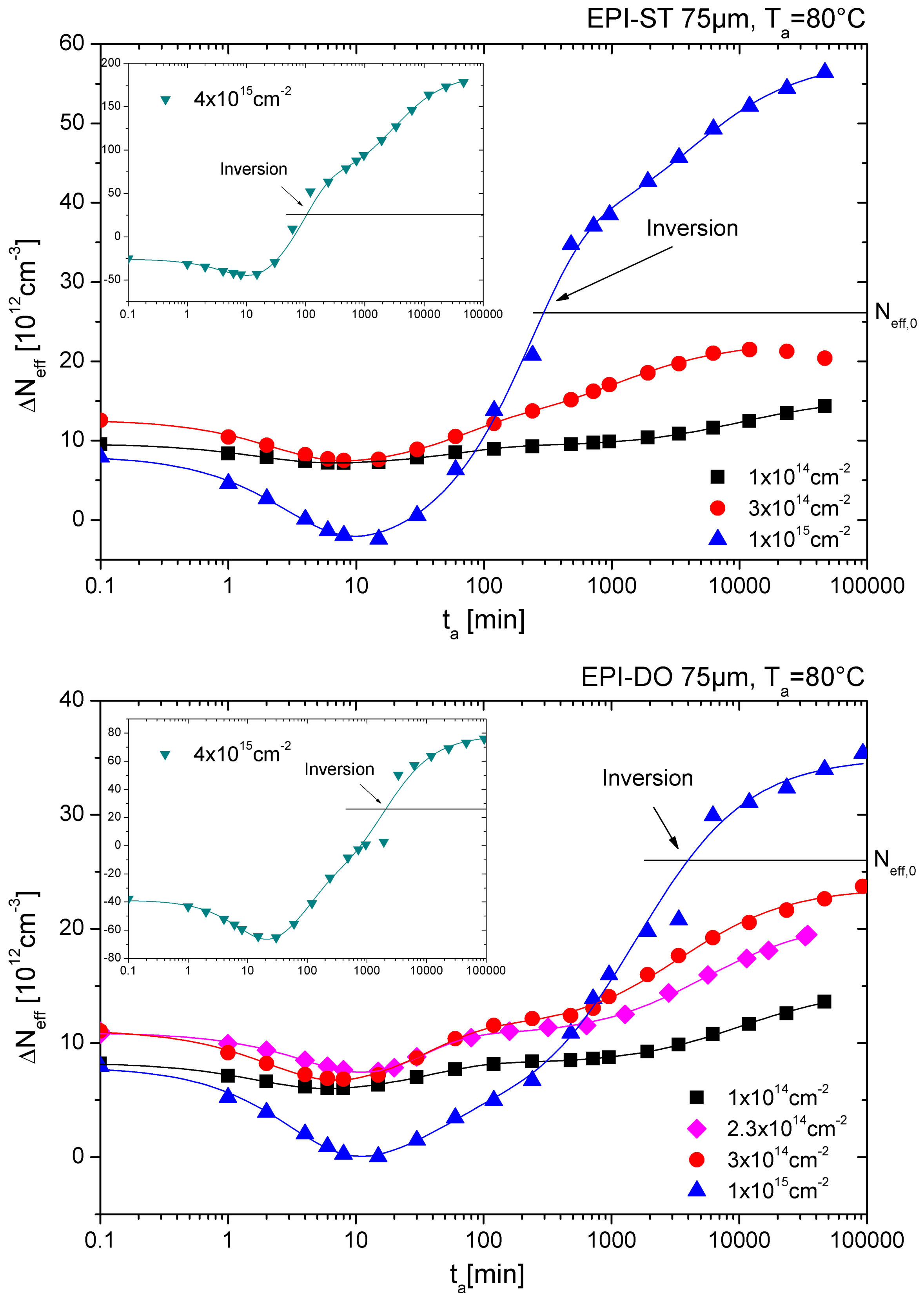

Figure 5.10: The ΔN_{eff} annealing curves for EPI-ST 75μm (top) and EPI-DO 75μm (bottom) including fits according to the Hamburg model. Note the different y-scales.

The short-term annealing can be described by a sum of first-order processes [Wun92]. However, both for annealing experiments at 80°C and for the application of detectors in particle physics experiments, only the component with the longest time constant τ_A plays a role. Thus, the short-term annealing is parameterised by one exponential term only:

$$N_A(\Phi_{eq}, t_a) = N_{A,0}(\Phi_{eq}) \exp\left(-\frac{t_a}{\tau_A}\right), \tag{5.6}$$

where $N_{A,0}(\Phi_{eq})$ is the short-term annealing amplitude.

The stable damage part consisting of donor removal and radiation-induced donors and/or acceptors is already explained in detail above. It is by definition independent of annealing time so that it adds just a constant N_C to the function.

Lastly, N_Y is the long-term annealing component that describes the build-up of acceptors. It turned out that the long-term annealing behaviour of epitaxial diodes is best described by the sum of a first-order process and a second-order one [Sch03]:

$$N_Y(\Phi_{eq}, t_a) = N_{Y,1}(\Phi_{eq}) \left(1 - \exp\left(-\frac{t_a}{\tau_{Y,1}}\right)\right) + N_{Y,2}(\Phi_{eq}) \left(1 - \frac{1}{1 + \frac{t_a}{\tau_{Y,2}}}\right), \tag{5.7}$$

with $N_{Y,\gamma}$ and $\tau_{Y,\gamma}$ being the respective amplitude and time constant for the process of order γ.

Results

Fig. 5.10 shows the annealing curves for EPI-ST 75μm and EPI-DO 75μm with fits according to the above explained model. The results for the fit parameters are displayed in Tab. 5.5. It has to be emphasised that it was very difficult to obtain a good fit. It was very unstable to have 7 free fit parameters as there were several minima of χ^2 in the multi-dimensional parameter space. Thus for some of the parameters constraints had to be introduced like all parameters except N_C be larger than 0 or $\tau_A < \tau_{Y,\gamma}$. Still, the question is whether the fit result is unique. Moreover, again the highly irradiated detectors presented more difficulties than the others. On the one hand one should be again aware of self-annealing effects that might lead to a distortion especially of the short-term parameters. On the other hand, the diodes irradiated by $1 \times 10^{15} cm^{-2}$ and $4 \times 10^{15} cm^{-2}$ type-inverted during annealing as indicated in the figure ($\Delta N_{eff} = N_{eff,0}$). Close to inversion the field distribution is not very well-defined because $|N_{eff}|$ is almost zero so that small fluctuations play a large role. As can be seen in the figure the points around inversion scatter more than the others. It was chosen here to exclude such points from the fit. However, one should keep in mind for the following discussion that this might lead to a distortion, especially for the first-order fit parameters. In the end, it should be noted that it is not completely possible to separate short-term and long-term annealing component and stable damage as a change in one component influences the results of the values of the others.

As mentioned, the short-term annealing range is very uncertain. It will be only noted here that the value of τ_A for the lowest and therefore most reliable fluence is around $2min$ for both ST and DO, which is in good agreement with results from [Sch03] for 50μm EPI detectors and even from [Mol99] for FZ. However, for higher fluences τ_A increases which cannot be explained if assuming a first-order process. This increase is reflected in a delay of

	Φ_{eq} $[10^{14}cm^{-2}]$	N_C $[10^{12}cm^{-3}]$	$N_{A,0}$ $[10^{12}cm^{-3}]$	τ_A $[min]$	$N_{Y,1}$ $[10^{12}cm^{-3}]$	$\tau_{Y,1}$ $[min]$	$N_{Y,2}$ $[10^{12}cm^{-3}]$	$\tau_{Y,2}$ $[min]$
ST	1	6.9 ± 0.1	2.7 ± 0.1	1.8 ± 0.2	2.4 ± 0.1	64 ± 7	6.0 ± 0.2	10090 ± 924
	3	6.5 ± 0.2	6.2 ± 0.2	2.4 ± 0.2	5.4 ± 0.4	62 ± 9	10.4 ± 0.3	1058 ± 130
	10	-4.4 ± 0.8	12.5 ± 1.0	3.2 ± 0.7	39.6 ± 1.8	223 ± 21	22.7 ± 1.5	3992 ± 1205
	40	-66.7 ± 2.7	41.0 ± 2.6	6.3 ± 0.6	130.5 ± 2.4	93 ± 6	123.2 ± 1.3	3050 ± 152
DO	1	5.5 ± 0.1	2.8 ± 0.1	1.9 ± 0.2	2.7 ± 0.1	39 ± 3	6.5 ± 0.1	10066 ± 619
	2.3	4.4 ± 1.2	6.5 ± 1.2	5.6 ± 0.9	6.2 ± 1.2	27 ± 6	10.0 ± 0.2	5286 ± 402
	3	5.4 ± 0.5	5.8 ± 0.5	2.4 ± 0.5	5.8 ± 0.5	37 ± 7	12.4 ± 0.3	3393 ± 327
	10	-1.8 ± 1.5	9.7 ± 1.5	3.5 ± 0.9	4.9 ± 1.4	39 ± 24	31.9 ± 0.8	1559 ± 150
	40	-81.9 ± 6.1	43.3 ± 5.9	9.1 ± 1.8	47.7 ± 5.8	91 ± 24	112.5 ± 4.2	1793 ± 279

Table 5.5: Fit results of the annealing curves at 80°C for EPI-ST 75μm and EPI-DO 75μm.

the minimum of ΔN_{eff} in the annealing curves of high fluences. N_A is tendentially increasing with fluence as expected.

The fluence dependence of the stable damage part N_C is displayed in Fig. 5.11 a). The same analysis like in Sec. 5.3.2 for $\Delta N_{eff,C}$ at $8min$ has been repeated here for N_C, i.e. the curves were fitted according to Eq. 5.3 with $N_C(\Phi_{eq}) = N_{C,0}\,(1 - \exp(-c\Phi_{eq})) + g_C\Phi_{eq}$ with the errors as weights. For comparison results from both Sec. 5.3.2 and here are presented in Tab. 5.6. It can be seen that the values differ quite substantially between the analysis of $\Delta N_{eff,C}$ at $8min$ and N_C. Ideally, N_C should be the better description of the stable damage because $\Delta N_{eff,C}$ at $8min$ is only an approximation and still contains contributions from the short- and long-term annealing. However, due to the high instability and model-dependence of the Hamburg model fit and the smaller amount of data points because only big diodes were included in the analysis of N_C, the results for $\Delta N_{eff,C}$ at $8min$ are regarded to be more reliable here. They have the additional advantage that they were obtained for all kinds of diodes and not only for 75μm. However, despite the differences for the absolute values between the results for N_C and $\Delta N_{eff,C}$, the general tendency is the same: g_C is negative, reflecting predominant donor production, which is higher for DO than for ST. Also, for both methods c is lower for DO than for ST.

Method	Material	$N_{C,0}$ $[10^{12}cm^{-3}]$	c $[10^{-14}cm^{-2}]$	g_C $[10^{-2}cm^{-1}]$	$\frac{N_{C,0}}{N_{eff,0}}$	$N_{C,0}\cdot c$ $[10^{-2}cm^{-1}]$
N_C from Hamburg model fit	ST 75μm	13.3 ± 1.9	0.99 ± 0.25	-1.9 ± 0.3	0.51 ± 0.08	13 ± 4
	DO 75μm	14.5 ± 5.3	0.67 ± 0.31	-2.1 ± 0.6	0.55 ± 0.20	10 ± 6
$\Delta N_{eff,C}$ at 8min	ST 75μm	14.4 ± 1.1	0.78 ± 0.13	-1.5 ± 0.1	0.56 ± 0.04	11 ± 2
	DO 75μm	23.1 ± 2.2	0.32 ± 0.04	-2.1 ± 0.1	0.88 ± 0.09	7 ± 1

Table 5.6: Stable damage parameters for EPI-ST 75μm and EPI-DO 75μm. Comparison between N_C from fit and $\Delta N_{eff,C}$ at $8min$.

The two amplitudes $N_{Y,\gamma}$ of the long-term annealing tendentially increase with fluence as expected. Fig 5.11 b) displays the sum $N_{Y,total}$ of the two components as a function of fluence, which shows an approximately linear increase, especially for ST: $N_{Y,total} = g_Y\Phi_{eq}$. The proportionality factor $g_Y = g_{Y,A} - g_{Y,D}$ is an effective long-term annealing introduction rate. The values found here,

$$g_Y = 0.0638 \pm 0.0006 \qquad \text{for ST and} \tag{5.8}$$

$$g_Y = 0.0564 \pm 0.0008 \qquad \text{for DO,} \tag{5.9}$$

are in fair agreement with [Mol99] and the positive sign shows that the long-term annealing

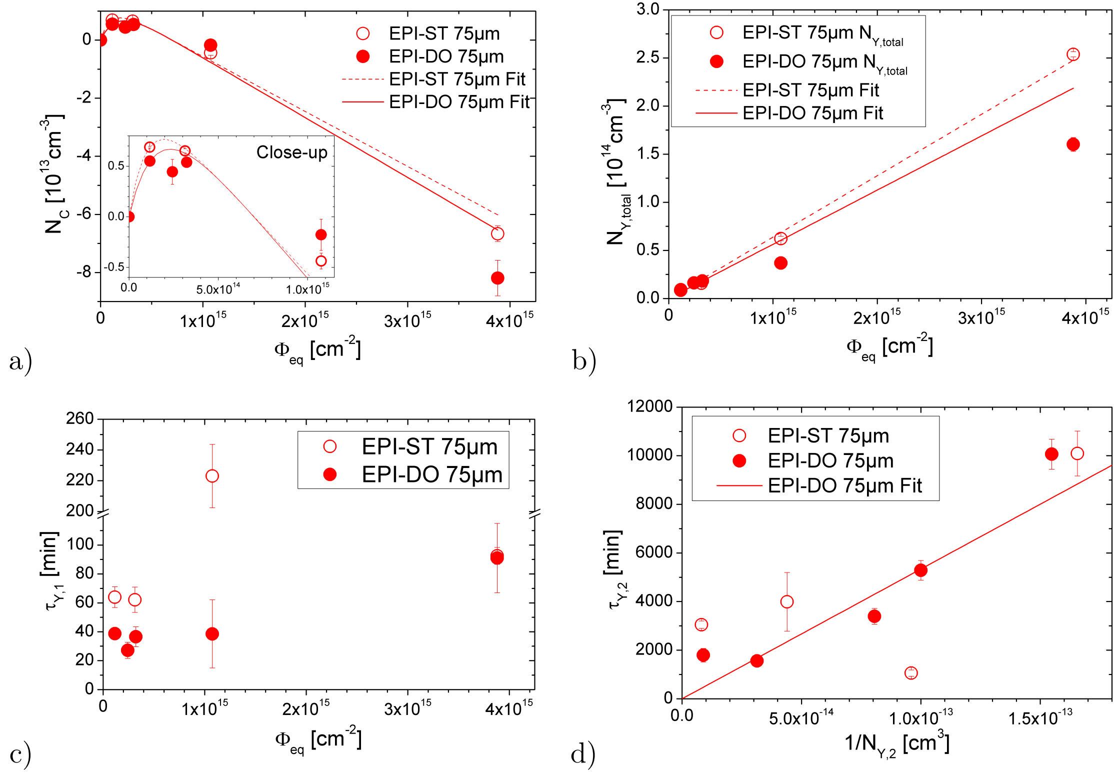

Figure 5.11: Hamburg model fit results for EPI 75μm. The displayed fluence is according to the α-normalised values up to $1 \times 10^{15} cm^{-2}$ and according to Al activation for $4 \times 10^{15} cm^{-2}$. a) The stable damage component as a function of fluence including a close-up for low fluences and weighted fits according to Eq. 5.3. b) The total long-term annealing introduction rate $N_{Y,total} = N_{Y,1} + N_{Y,2}$ as a function of fluence including weighted linear fits. c) The first-order time constant $\tau_{Y,1}$ as a function of fluence (note the break in the y-axis). d) The second-order time constant $\tau_{Y,2}$ as a function of $1/N_{Y,2}$ with a weighted linear fit for DO.

is dominated by acceptor generation as expected. g_Y is a bit less for oxygen-enriched material, which also confirms earlier observations. This is the reason why the diodes made of ST material undergo type inversion earlier during annealing than oxygen-enriched material (see Fig. 5.7).

The long-term annealing was described here by the sum of a first- and a second-order process which should be reflected by the different behaviour of the time constants, i.e. $\tau_{Y,1} = const$ and $\tau_{Y,2} \propto \frac{1}{N_{Y,2}}$ (see Sec. 3.5). Fig. 5.11 c) shows that $\tau_{Y,1}$ is approximately constant at low fluences as expected. The increase at higher fluences might be misleading due to the already above-mentioned uncertainties. Fig. 5.11 d) shows that $\tau_{Y,2}$ is approximately linear to $\frac{1}{N_{Y,2}}$ for DO. This might be also the case for ST, but the data points scatter too much for a reliable conclusion so that no fit was performed in that case. Thus, the first- and second-order nature of the long-term annealing could be confirmed.

5.3.4 Consequences for Radiation Hardness

After having analysed the fluence and annealing dependence of ΔN_{eff} and having tried to compare the data with a microscopic model, it is instructive to come back to the depletion

voltage with this knowledge. It can be now understood why e.g. the $75\mu m$ diodes do not always have the lowest depletion voltage at $8min$ at 80°C (cf. Fig. 5.7): On the one hand it is true that a lower thickness tendentially means a lower depletion voltage as $U_{dep} \propto d^2$. But on the other hand, a lower thickness also implies a higher oxygen concentration which leads to a larger donor introduction at high fluences. It turned out that the absolute value of the effective introduction rate g_C is higher for $75\mu m$ than e.g. for EPI-ST $100\mu m$ and overcompensates the advantage of the lower thickness at high fluences.

It should be noted that in EPI diodes, the oxygen dependence of the increase in U_{dep} at high fluences is in contrast to FZ material. In FZ oxygen-enrichment decelerates predominant acceptor creation so that after type inversion a negative N_{eff} becomes less fast more negative, thereby slowing down the U_{dep} rise. EPI material, however, is characterised from the beginning by high oxygen levels and thus by predominant donor creation. Therefore, a further oxygenation results in a faster donor generation and consequently N_{eff} rise.

Regarding the depletion voltage at $8min$ at 80°C (approximately stable damage), it turned out that EPI-ST $100\mu m$ seems to be the optimum material out of the here investigated ones. Up to a fluence of $4 \times 10^{15} cm^{-2}$ its depletion voltage remains very moderate below $250V$. But also the other materials do not exceed $400V$ except EPI-DO $150\mu m$ which could not be measured anymore at this fluence but has probably a much higher depletion voltage. However as mentioned, for the SLHC a total fluence of up to $1.6 \times 10^{16} cm^{-2}$ is expected in the innermost vertex layer. Unfortunately, experimental problems prevented from performing measurements of U_{dep} at such high fluences. But in order to obtain a rough estimate of the depletion voltage, the stable damage fit parameters from Tab. 5.4 were used for an extrapolation of $\Delta N_{eff,C}$ before transforming it to U_{dep} via Eq. 2.5. The extrapolated depletion voltage is displayed in Fig. 5.12. It should be emphasised that due to the fit and measurement uncertainties, this extrapolation is very rough.

The bias limit for the operation of detectors is supposed to be around $500V$ because the infrastructure and the electronics are not designed to withstand much higher voltages. Depending on the device configuration, it is possible to run the detector in an under-depleted mode to a certain extent, but with adverse effects on the charge collection efficiency because the sensitive region is reduced. However, concerning the sensor one should also keep in mind the maximum electric field strength because this is the parameter that is important for the danger of breakthrough effects. As $E_{max} = \frac{2}{d}\sqrt{U \cdot U_{dep}}$ for $U < U_{dep}$ in a linear-field approximation, which follows from combining Eqs. 2.2, 2.4 and 2.5, the electric field maximum rises for increasing U_{dep} even if the bias voltage is fixed. If a bias of $500V$ is applied to a detector with a depletion voltage of the same value, E_{max} is already quite high[11] with $67kV/cm$ for $150\mu m$, $100kV/cm$ for $100\mu m$ and $133kV/cm$ for $75\mu m$ detectors. Therefore, for a first estimate a depletion voltage limit of $500V$ is assumed. In this case, EPI-ST $100\mu m$ would withstand up to a fluence of about $8.5 \times 10^{15} cm^{-2}$; at $1.6 \times 10^{16} cm^{-2}$ it would have a depletion voltage of about $900V$. Not much worse is EPI-ST $75\mu m$ which would reach $500V$ at $7 \times 10^{15} cm^{-2}$, followed by DO $75\mu m$ and $100\mu m$ at $5.5 \times 10^{15} cm^{-2}$. The $150\mu m$ detectors would survive only a fluence of approximately $4 \times 10^{15} cm^{-2}$ (ST) and $2 \times 10^{15} cm^{-2}$ (DO). It should be noted that in practice, the depletion voltage for segmented detectors is a bit higher than for pad diodes because of the gaps between the electrodes.

Thus, at first sight it seems that none of the here investigated detectors will survive the whole SLHC period. However, these considerations were only done for the stable damage

[11] According to [Sze07] the maximum field at breakdown can be estimated as $200kV/cm$ for a doping level of $10^{13} cm^{-3}$.

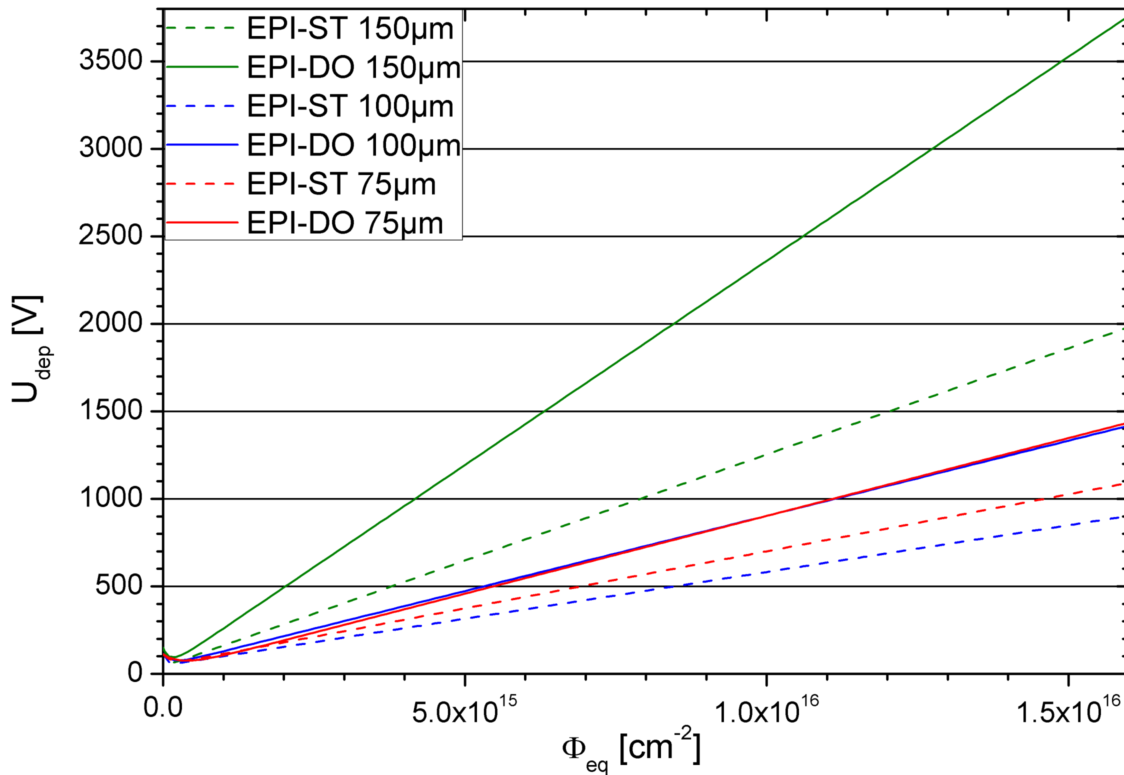

Figure 5.12: The depletion voltage up to $1.6 \times 10^{16} cm^{-2}$ as calculated according to the stable damage fit parameters from Tab. 5.4. The curves for EPI-DO $100\mu m$ and EPI-DO $75\mu m$ overlap and are hardly distinguishable.

point at $8min$ annealing and it was assumed that the whole irradiation is done at one single moment before the annealing. But this is not very realistic because the SLHC will run for years with maintenance periods in between so that irradiation and annealing will alternate. For the DOFZ detectors used at the LHC it is tried to keep this annealing at a minimum by cooling also during most of the beam-off periods. This is because for such detectors both the stable damage and the long-term annealing are dominated by acceptor introduction so that these two effects enhance each other. In contrast, as shown here, for EPI detectors the stable damage is dominated by donor creation whereas the long-term annealing is still characterised by acceptor introduction. Consequently, these two effects can compensate each other to a certain extent, depending on the fluence and annealing point. Therefore the long-term annealing during maintenance periods can be beneficial and the detectors might survive up to higher fluences than predicted in the simple extrapolation above. To check this, it would be desirable to perform a so-called *CERN scenario experiment* that realistically simulates the consecutive periods of irradiation and annealing for an SLHC operation. Experiments in the past for thinner epitaxial material (up to $50\mu m$) have proven the beneficial effect [Lin06b] and it would be interesting to see how the thicker materials investigated here perform. Moreover, one has to consider that the here observed results are valid for proton irradiation only, which is a good simulation for detectors near the vertex point because the there mostly expected pions behave very similarly. But there is also a certain influence of neutron radiation for which the stable damage is dominated by acceptor introduction in $75\mu m$ EPI diodes [Koc07].

Thus, this might also compensate the predominant donor generation after charged hadron irradiation to a certain extent, thereby extending the detector lifetime.

5.4 TCT Results

In the following sections the results regarding charge collection properties and trapping, which were obtained with TCT, will be presented. First, the outcomes of the $670nm$ laser-TCT measurements will be shown with emphasis on the effective trapping time constant τ_{eff} and the electric field distribution, before presenting CCE measurements with α-particles. Finally, the measured data will be compared to charge collection simulations.

Most of the TCT measurements were done after $30min$ annealing at 80°C for the following reasons. Firstly, this is already quite a stable point at which the short-term annealing is basically completed so that long measurements at room temperature have a negligible effect on the further annealing of I_{dep} and U_{dep}. Secondly, in many cases the depletion voltage has already decreased again after its maximum mostly at $8min$ (see Fig. 5.6), which makes it easier to perform the necessary measurements above full depletion.

5.4.1 Time-Resolved Current Signals with 670nm Laser-TCT

As explained in Sec. 4.5.2 time-resolved current signals could be obtained with the help of a new $670nm$ laser-TCT setup using the small diodes. However, this was only possible for the rather thick $150\mu m$ detectors as for the thinner ones the detector capacitance was still too large. Thus, the presented results are close to the resolution limit, which can be seen from the fact that the rise and fall times are not much shorter than the pulse width. The measured TCT current pulses after front injection are presented in Fig. 5.13 for a selection of different bias voltages (after $30min$ annealing at 80°C, measured at room temperature).

Determination of the Effective Trapping Time Constant

One of the most important questions is how the trapping of signal charge carriers at radiation-induced defects influences the current pulse shape and the collected charge. According to Sec. 2.2.5 the number of charge carriers decreases exponentially with time in a first approximation (cf. Eq. 2.17). As the induced current is proportional to the number of charge carriers, it behaves in the same way:

$$I_m(t) = I_0(t) \exp\left(-\frac{t - t_0}{\tau_{eff}}\right), \tag{5.10}$$

where $I_m(t)$ is the measured current, $I_0(t) = \frac{q_0 N_0}{d} v_{dr}(t)$ the ideal current in the absence of trapping, τ_{eff} the effective trapping time constant and t_0 the start of the pulse. To be precise, this relation is valid for each charge carrier type separately, but in the present case of $670nm$ laser front injection, almost only electrons are contributing.

One way to determine the trapping time constant is to fit the collected charge as a function of bias voltage $Q(U)$ with a calculated model function, i.e. the integral of Eq. 5.10 (see Sec. 5.4.3). The drawbacks of such an approach are the numerous model assumptions necessary, e.g. with respect to a drift velocity - electric field dependence and the electric field

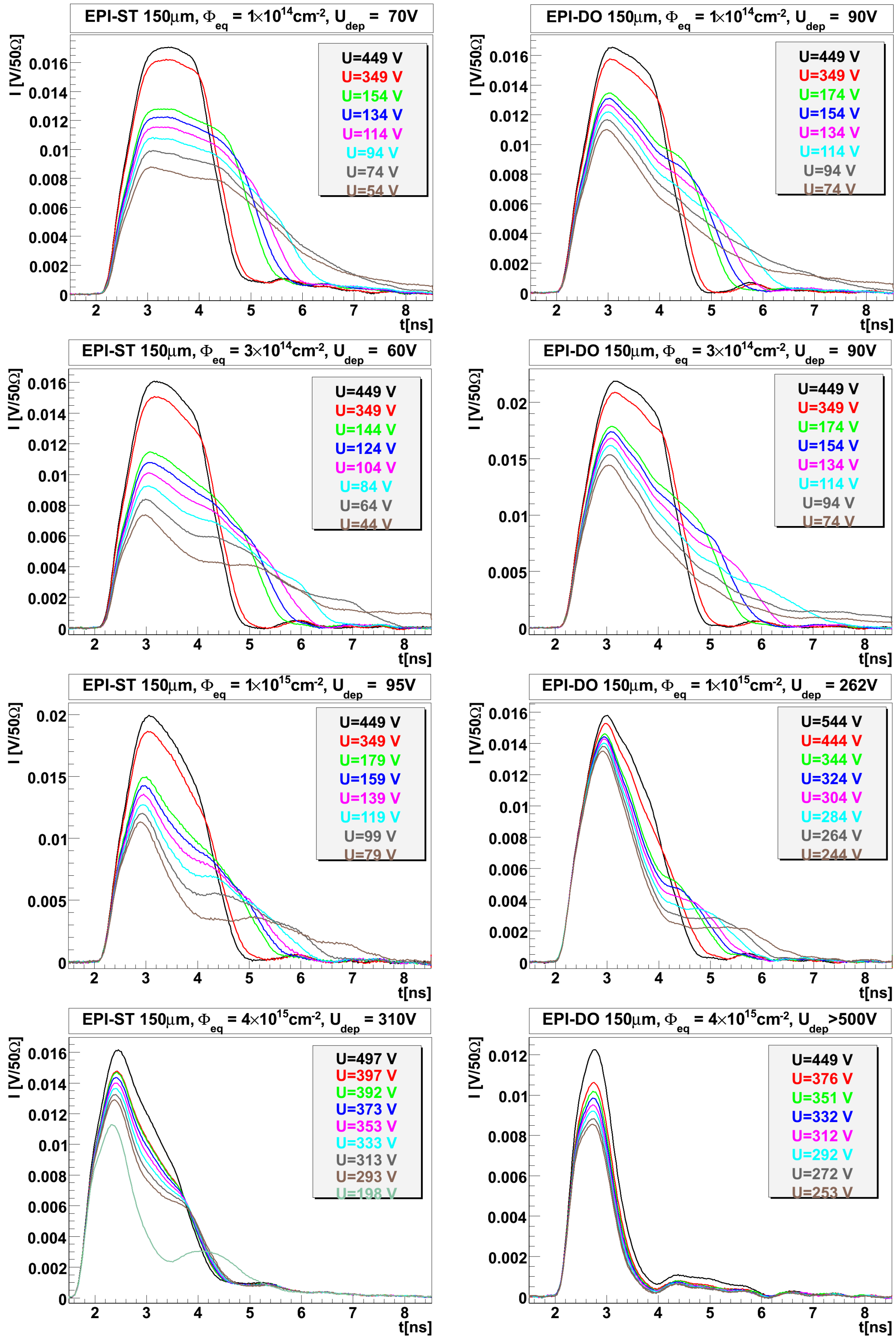

Figure 5.13: TCT current pulses as measured at room temperature after front injection with 670nm laser light for EPI-ST 150μm (left) and EPI-DO 150μm (right) without amplifier (30min at 80°C). The denoted depletion voltage was obtained with the CV method at 10kHz (not measurable for EPI-DO 150 μm, $4 \times 10^{15} cm^{-2}$). Note that the here labelled fluences differ substantially from the α-normalised values which can be found in Tab. 5.7.

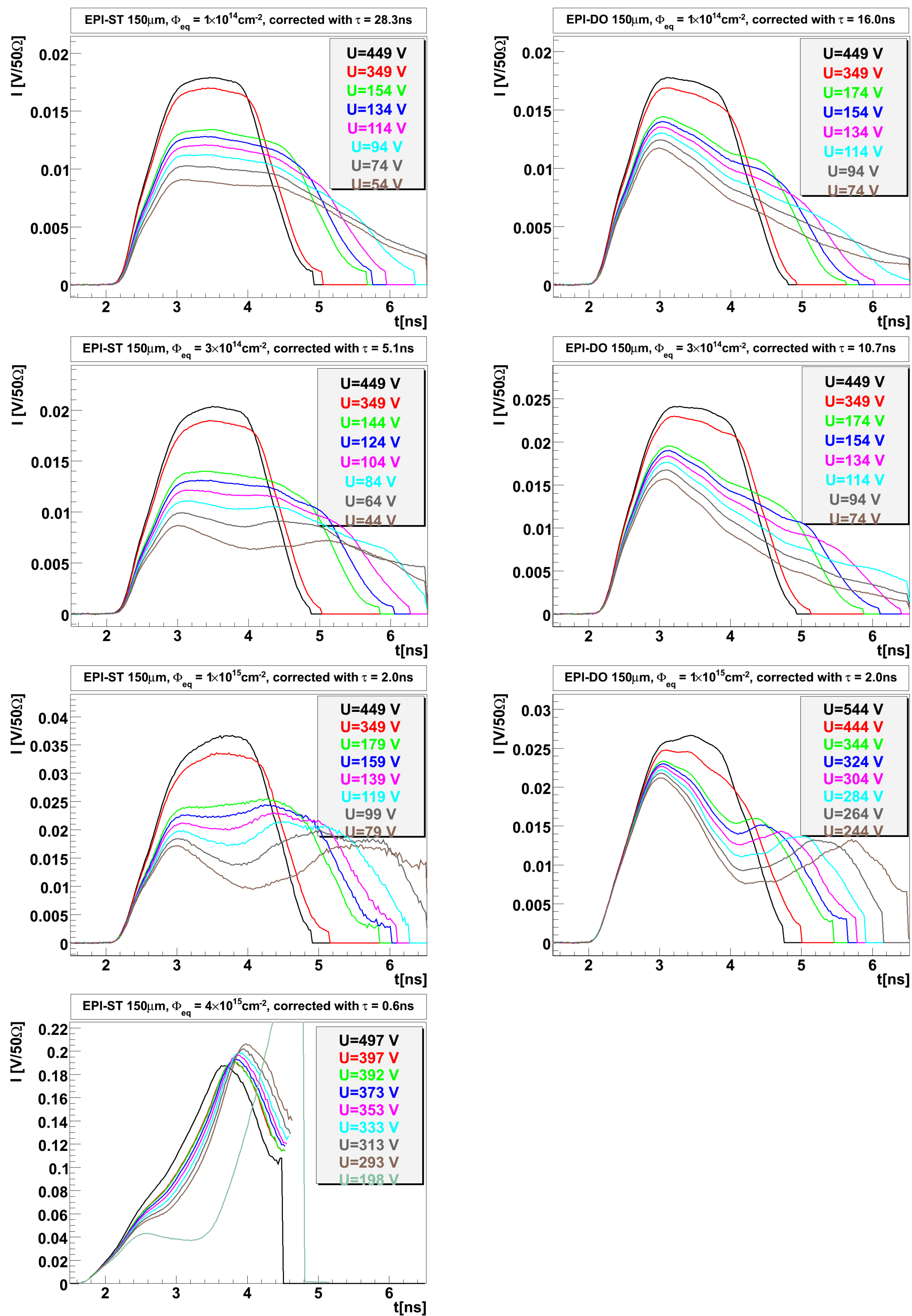

Figure 5.14: TCT current pulses corrected for trapping using $\tau = \tau_{eff,lit}$ according to [Kra01]. The signal has been cut off directly after the pulse. The correction was not possible for EPI-DO 150μm, $4 \times 10^{15} cm^{-2}$ because only signals below full depletion could be measured.

distribution inside the diode. But the advantage is that no time-resolved signal is required, only the integrated charge. Thus before achieving to improve the time-resolution with the new TCT setup, it was also tried here. It would also allow a determination of τ_{eff} for the thinner diodes. However, it turned out that a successful reproduction of the measured $Q(U)$ curve with a calculated function could not be achieved satisfactorily. This problem will be referred to again in Sec. 5.4.3.

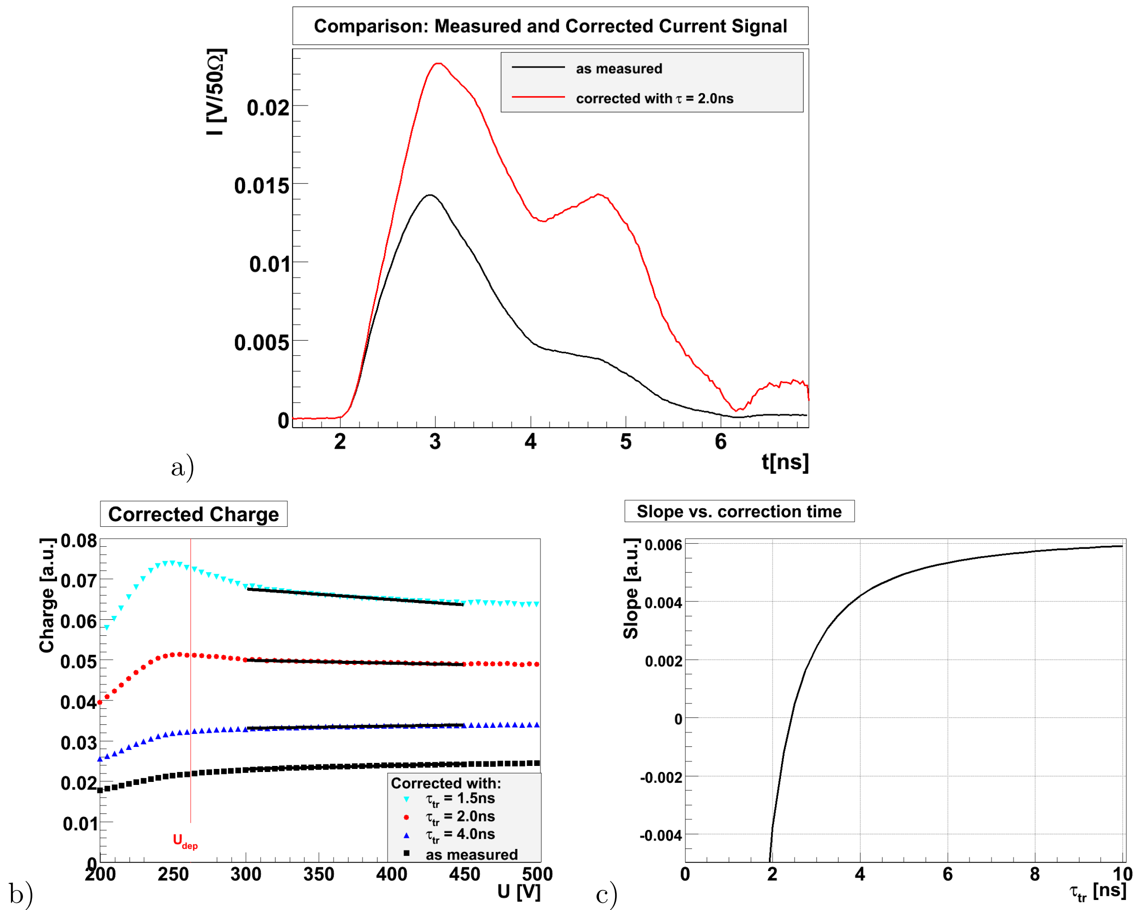

Figure 5.15: The principle of the charge correction method for the example of the EPI-DO $150\mu m$ diode irradiated by $1 \times 10^{15} cm^{-2}$. a) The TCT current signal at $305V$ as measured and corrected with $\tau_{tr} = 2ns$. b) The integrated charge of the signal as a function of bias voltage for different correction times with linear fits in the range $300V$ - $450V$. c) The slope of the linear fits from b) as a function of τ_{tr}. The trapping time constant can be obtained from the intersection point with zero.

Instead, the widely used *charge correction method (CCM)* according to [Kra01] was applied. This approach is free of electric field and drift velocity model uncertainties, but it requires a time-resolved signal so that only the $150\mu m$ diodes could be analysed. The basic idea is to take the measured current pulse shape $I_m(t)$ and correct it with different possible trapping time constants τ_{tr} by inverting Eq. 5.10, i.e. by multiplying it with $\exp\left(\frac{t-t_0}{\tau_{tr}}\right)$ (see Fig. 5.15 a)). Then the corrected signals are integrated and the collected charge as a function of bias voltage is considered for different τ_{tr} as shown in Fig. 5.15 b). In the case of no trapping the collected charge is expected to be independent of voltage in a depleted detector

because if no charge carriers are captured it does not matter how long the drift takes. Therefore, the value of the right effective trapping time is found if the corrected charge curve has a slope of zero above the depletion voltage. This is determined by performing a linear fit to the corrected $Q(U)$ curves and plotting the slope against τ_{tr} as shown in Fig. 5.15 c). The intersection point with zero is the seeked trapping time constant because $Slope(\tau_{tr} = \tau_{eff}) = 0$. It should be noted that also this method is not free of assumptions. One condition is that the current pulse is due to charge carrier drift only and free of distortions, e.g. electronic ones. Moreover, it is based on the validity of Eq. 2.17, i.e. that trapping is described by one exponential term with one time constant only. This requires τ_{eff} to be independent of both the position inside the detector and the bias voltage. It relies on a uniform trap density and constant occupation. Moreover, detrapping effects, i.e. the release of trapped carriers back to their respective band, are neglected. If such an approach provides a reasonable description of trapping will be discussed further in Sec. 5.4.3.

The CCM was applied to the measured current pulses of the detectors shown in Fig. 5.13 except for EPI-ST DO $150\mu m$ irradiated by $4 \times 10^{15} cm^{-2}$ because that diode could not be measured above depletion. The following difficulties and uncertainties have occurred. On the one hand it was already mentioned that the time resolution is still quite limited due to finite rise and fall times. It was tried to improve the resolution by deconvolution according to Eq. 4.4, but as already pointed out, this resulted only in a small rise time improvement. Moreover, in some cases the signal shape was distorted and noise increased due to the deconvolution. Another problem was the shape at the end of the pulse. Sometimes a kind of shoulder was seen, probably due to a bad back contact. In many cases this could be solved by remounting and measuring again, but e.g. for ST $1 \times 10^{14} cm^{-2}$ and $4 \times 10^{15} cm^{-2}$ it is still apparent. Moreover, in nearly all cases there is a small bump around $5.5 - 6 ns$ of unknown origin, possibly a baseline oscillation or reflection. Unfortunately, this is exactly the region that is especially enhanced by the exponential correction so that small distortions due to noise and baseline oscillations are exaggerated (see e.g. Fig. 5.15 a)). Thus, the result for τ_{eff} strongly depends on the integration time window, whether a cutoff is being made to exclude such effects and on the cutoff level. Additionally, there is a significant sensitivity on the fitting range in which the slope of $Q(U)$ is determined.

In order to study the level of uncertainty, for each analysis always a variety of different methods has been tried out, e.g. with or without deconvolution or cutoff and for different cutoff levels, integration time windows and fitting ranges. The results presented in Tab. 5.7 are after deconvolution and a cutoff directly at the end of the pulse and for a fitting range that is reasonably away from the depletion voltage, i.e. at least $30V$ above. The denoted

	EPI-ST $150\mu m$			EPI-DO $150\mu m$		
denoted fluence Φ_{eq} $[cm^{-2}]$	α-normalised fluence Φ_{eq} $[cm^{-2}]$	$\tau_{eff,lit}$ $[ns]$	τ_{eff} $[ns]$	α-normalised fluence Φ_{eq} $[cm^{-2}]$	$\tau_{eff,lit}$ $[ns]$	τ_{eff} $[ns]$
1×10^{14}	6.9×10^{13}	28.3	-	1.2×10^{14}	16.0	18.5 ± 7.0
3×10^{14}	3.8×10^{14}	5.1	4.4 ± 1.3	1.8×10^{14}	10.7	13.4 ± 4.0
1×10^{15}	9.9×10^{14}	2.0	1.8 ± 0.2	9.8×10^{14}	2.0	2.6 ± 0.6
4×10^{15}	3.1×10^{15}	0.6	0.7 ± 0.2	-	-	-

Table 5.7: The effective trapping time constant τ_{eff} as obtained with the CCM. For comparison values from the literature $\tau_{eff,lit}$ are shown according to [Kra01] (extrapolated). Note that the α-normalised fluences used here differ substantially from the denoted ones from Al activation.

error was estimated according to the variations in τ_{eff} when using other methods. It turned out that the results were very inaccurate for the lowest measured fluence, probably because due to the low level of trapping the $Q(U)$ curve is already very flat as measured. Thus, it was not possible to determine τ_{eff} for ST $1 \times 10^{14} cm^{-2}$ and the result for the DO diode is still very uncertain at this fluence. The most stable results could be obtained for $1 \times 10^{15} cm^{-2}$. For the ST $4 \times 10^{15} cm^{-2}$ diode, the question arises whether it makes sense to perform a correction with a τ_{eff} that is in the same range as the rise time of the signal, i.e. the time resolution, and only about one third of the charge collection time. However, it turned out that the determined τ_{eff} is quite stable and in a range that is expected.

Tab. 5.7 also includes the expected values $\tau_{eff,lit}$ from the literature according to [Kra01]. There it had been found out that the trapping probability, i.e. the inverse trapping time constant $\frac{1}{\tau_{eff}}$, is proportional to the fluence (see Sec. 3.4) with the trapping-related damage parameter $\beta_{e,lit}$ or $\beta_{h,lit}$ as proportionality constant (values are listed in Tab. 5.8). However, it should be mentioned that those measurements had been done on the one hand only for FZ and DOFZ material and on the other hand only up to a fluence of $2 \times 10^{14} cm^{-2}$ (later the linearity was confirmed up to $9 \times 10^{14} cm^{-2}$ by [Krs04]). Therefore, the reference values $\tau_{eff,lit}$ shown

	β_e $[10^{-16} cm^2 ns^{-1}]$	β_h $[10^{-16} cm^2 ns^{-1}]$
EPI-ST $150\mu m$	5.4 ± 0.5	-
EPI-DO $150\mu m$	4.0 ± 0.7	-
EPI $150\mu m$ combined	4.9 ± 0.4	-
FZ (β_{lit})	5.1	6.5

Table 5.8: The trapping-related damage parameter β at room temperature. The values for EPI material were obtained from the weighted linear fits in Fig. 5.16, the values for FZ ($T = 294K$) are taken from [Kra01].

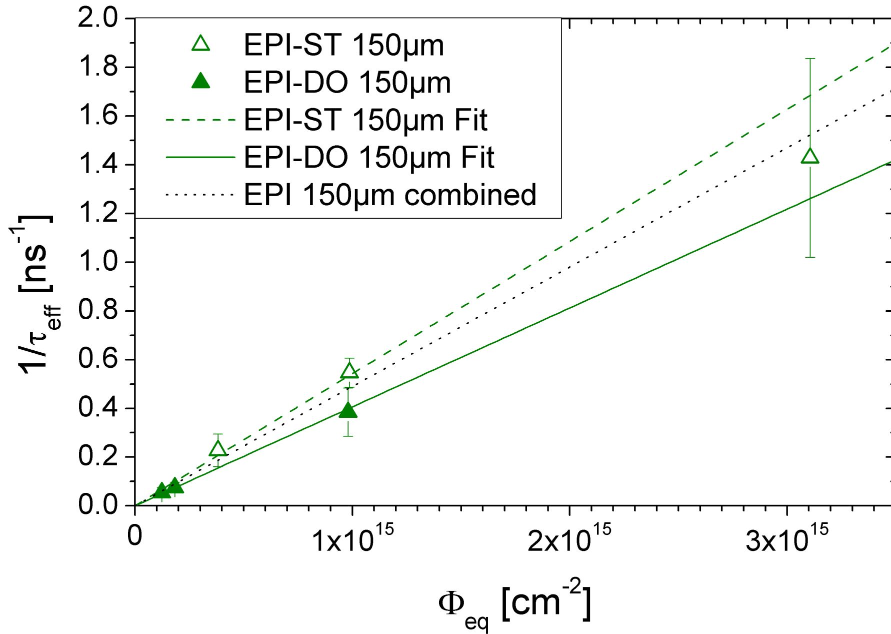

Figure 5.16: The trapping probability $\frac{1}{\tau_{eff}}$ as a function of fluence including error-weighted linear fits. As fluence the α-normalised values were taken.

here are linear extrapolations using $\beta_{e,lit}$. It was of high interest to investigate whether the trapping time constants for EPI material are the same as for FZ and if at such high fluences a linear relation still holds. It can be seen that the results for EPI diodes found here agree within the errors with $\tau_{eff,lit}$. Fig. 5.16 shows the trapping probability as a function of fluence. Apparently, a linear fit gives a good description of the data. A weighted fit that combines both ST and DO yields a trapping-related damage parameter $\beta_e = (4.9 \pm 0.4) \times 10^{-16} cm^2 ns^{-1}$ that agrees well with the value $\beta_e = 5.1 \times 10^{-16} cm^2 ns^{-1}$ from [Kra01] for FZ material. If fitted separately, β_e for DO is approximately 25% lower than for ST (see Tab. 5.8). However, as all single data points agree within the errors with the combined fit, this difference is not statistically significant, especially as there are only three data points each. Thus, also here it would be desirable to have more intermediate fluence steps, which are already planned to be provided by the next irradiation campaign.

To conclude, neither a difference between EPI and FZ material with regard to τ_{eff} nor a deviation from linearity in this high fluence range could be observed.

Electric Field Distribution - Double Peak Effect

As explained in Sec. 4.5, from the shape of the current signals conclusions regarding the electric field distribution inside the space charge region can be drawn. All curves show the electron signal after front injection. From looking at the measured pulse shapes in Fig. 5.13 it seems that no space charge sign inversion has occurred because the maximum of the peak is at the beginning, i.e. at the p^+ front side, and the signal decreases as the electrons drift towards the rear contact. This is in agreement with the results from the U_{dep} annealing curves presented in Sec. 5.3. However, for a reliable conclusion one has to consider that the signal is affected by trapping most strongly at later times so that after a correction the pulse shape might look different. Fig. 5.14 displays the signals after correcting for trapping with $\tau_{eff,lit}$. The signal curves for DO still clearly show the behaviour of non-inverted diodes. But for ST the slope of the curve is flatter, although still negative for $1 \times 10^{14} cm^{-2}$ and $3 \times 10^{14} cm^{-2}$. However, for $1 \times 10^{15} cm^{-2}$ there tendentially appears to be even a slight increase of the signal, whereas for $4 \times 10^{15} cm^{-2}$ a strong rise is observed. This seems to hint at a space charge sign inversion, which would be in contrast to the findings from the U_{dep} annealing behaviour. But as already mentioned in the last section, it is doubtful if a correction gives reliable results in the case of τ_{eff} being in the same region as the signal rise time.

It can be clearly seen that at high fluences the signal does not decrease monotonically anymore, especially near to the depletion voltage. Instead, a double peak structure is visible, i.e. a re-increase at the end of the pulse, which is even more pronounced after correcting for trapping. This has been already observed before and can be explained by the formation of a so-called *double junction*. In the following a brief overview on the theory of its formation is given, which can be found in more detail in [Ere02]: Due to the high level of reverse currents at high fluences there is a large number of free charge carriers inside the space charge region. Although the overall current density is constant throughout the detector, this is different when looking separately at the electron and hole current density, respectively. From the continuity equation it follows that the current density near the p^+ contact is dominated by holes and near the n^+ contact by electrons. Therefore, as a high current density implies a high charge carrier density, there is a large number of free electrons at the back side, which leads locally to an enhanced occupation of deep defect levels with electrons. Thus, if enough acceptors are occupied, this might eventually over-compensate the originally positive space charge in this

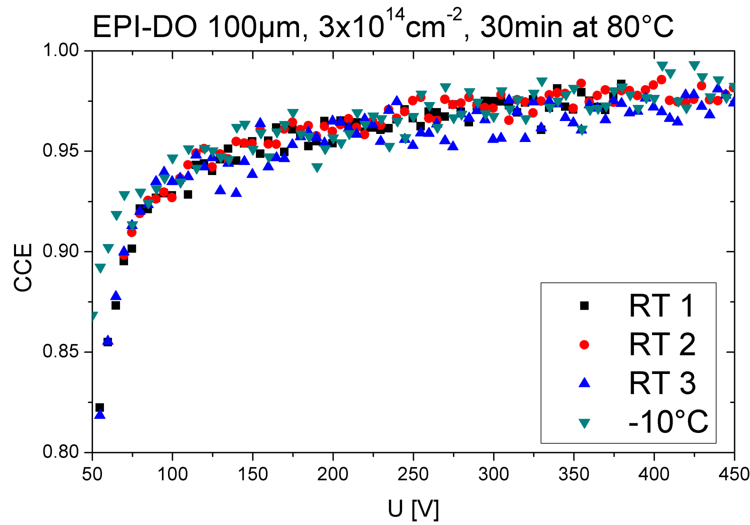

Figure 5.17: Different CCE measurements for the same detector at different temperatures show both a good reproducibility and temperature independence. The different measurements at room temperature (RT) were all done on different days after demounting and remounting of the sample.

region, leading to a locally limited type inversion. Consequently, in addition to the regular p-n junction at the front side, a second p-n junction forms near the back side. This implies that the electric field distribution deviates from the linear behaviour of an ideal abrupt junction diode and exhibits the double peak structure seen here.

5.4.2 CCE Measurements with α-TCT

Charge collection efficiency measurements were performed using $5.8 MeV$ α-particles. The efficiency was obtained by integrating the TCT current pulse in order to get the collected charge Q, followed by dividing it through the collected charge Q_0 of an unirradiated detector of the same material type. As only the integrated charge is considered, no time resolution of the current signal is required so that big diodes of all thicknesses could be used.

As measurements of the highly irradiated detectors could be only performed at -10°C due to their large currents, it was checked before for lower irradiated diodes which could be examined at both 20°C and -10°C that measurements at both temperatures result in a comparable CCE. The temperature dependence of mobility (rises with decreasing temperature in the considered range) and τ_{eff} (decreases with decreasing temperature [Kra01]) are obviously such that the enhanced trapping probability at lower temperature is compensated by a faster drift, resulting in an approximately constant CCE. This effect was also observed before by [Kra05] and is important to know with respect to the application at the LHC and SLHC because there the Si detectors will be operated at about -7°C to -10°C. Fig. 5.17 shows different measurements for the same diode at both temperatures, which indicate that the temperature independence and reproducibility of charge collection measurements is reasonably good. Moreover, for the determination of the precision of Q_0 several different unirradiated detectors of the same material and thickness were compared. Hardly any variations were found. To conclude, the estimated error for the CCE determination is supposed to be within 3 %.

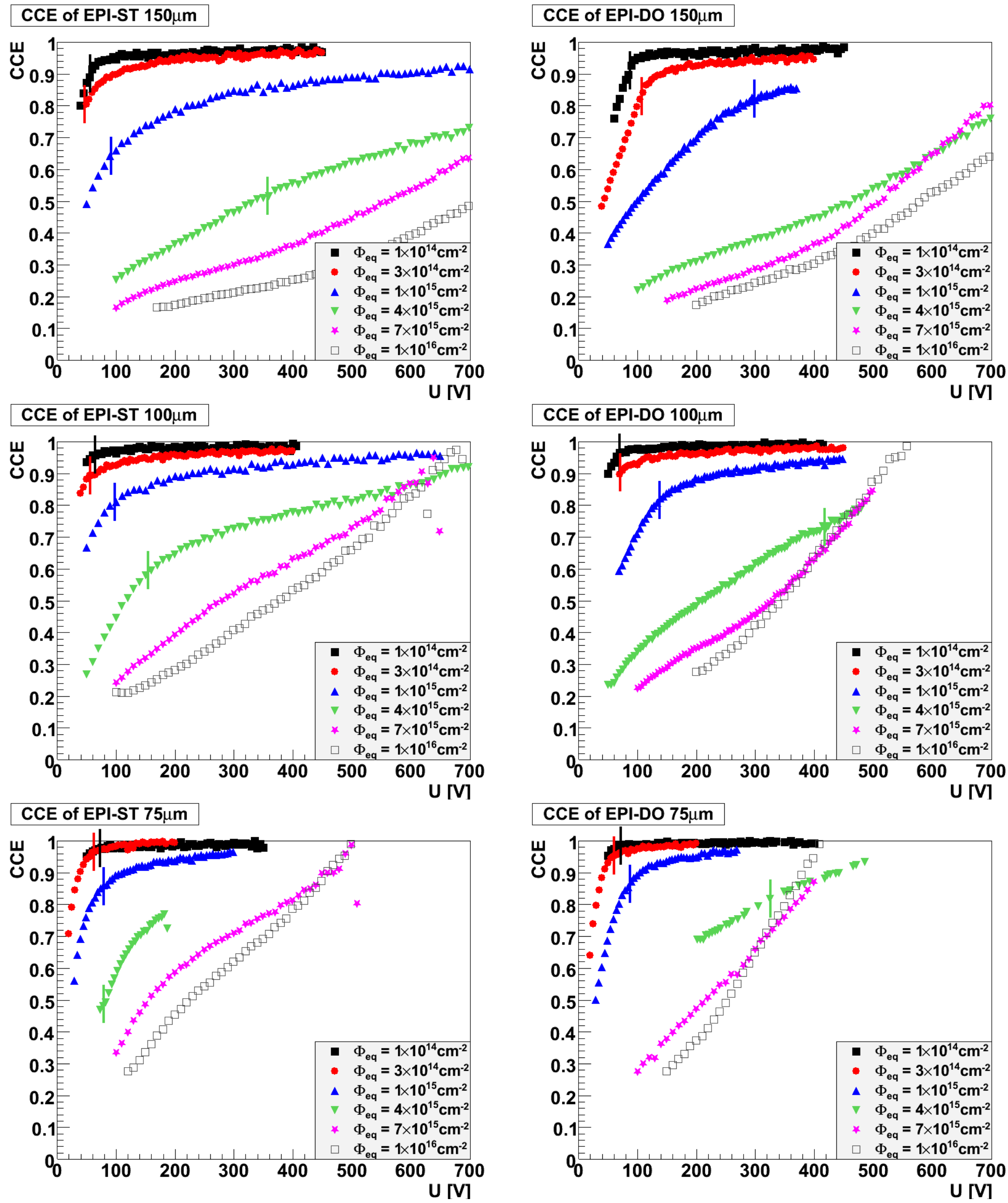

Figure 5.18: CCE as a function of bias voltage as measured with α-TCT (big diodes). The vertical lines indicate the depletion voltage as measured with CV at $10kHz$ where possible (for EPI-ST $150\mu m$ and EPI-DO $100\mu m$ at $4{\times}10^{15}cm^{-2}$ the U_{dep} as measured for the small diodes is shown). Up to a fluence of $4 \times 10^{15}cm^{-2}$ the measurements were done at $30min$ at 80°C annealing for $150\mu m$ and $100\mu m$ and at $60min$ at 80°C for $75\mu m$. For higher fluences the measurements were done without annealing step. Up to $1 \times 10^{15}cm^{-2}$ the CCE was measured at room temperature, whereas for the higher irradiated diodes measurements could be only performed during cooling at -10°C.

Fig. 5.18 shows the results for each material type at different fluences. First of all, it can be seen that the CCE grows monotonically with respect to the applied bias voltage even above U_{dep}. This is easy to understand because the increasing drift velocity results in a faster charge collection so that less trapping occurs. However, one would expect a saturation effect at high voltages due to the saturating drift velocity. Whereas this seems to be the case at low fluences, it is obviously violated at high fluences, where some of the detectors even show an increasing slope. Moreover, it is remarkable that sometimes the CCE of the two highest fluences crosses the curves of lower irradiated diodes. In some cases their CCE even surpasses 1, going up to 1.3, which cannot be seen properly in Fig. 5.18 because the y-axis terminates before. This cannot be explained merely by a possible reduction of trapping at high fluences, but requires the introduction of charge amplifying effects. It is assumed that due to the high depletion voltage at such large fluences the electric field inside the detector is so high that avalanche effects are triggered. Of course it would be highly desirable to exploit such internal amplification effects that compensate for or even exceed the trapping-related charge loss. But it is not clear yet whether it can be well-controlled and if it does not have an adverse impact on the position resolution in segmented detectors. However, besides amplification there are also other not well-understood effects, which will be investigated further in the next section when comparing the measured CCE curves to simulations.

At a given voltage, the charge collection efficiency is decreasing with increasing fluence (except for the above-mentioned not completely understood deviations at high fluences and voltages) because more trapping centres are introduced by radiation. In order to compare the efficiency as a function of fluence for the different materials, the CCE at a fixed voltage ($350V$) is shown in Fig. 5.19. $350V$ was chosen because this is a typical voltage used for operation in particle physics experiments. Moreover, most of the detectors could still be measured successfully at this voltage, were fully depleted and the CCE at low fluences has already saturated. However, this is not true for all of the detectors. For example the EPI-ST $75\mu m$ detector at $4 \times 10^{15} cm^{-2}$ could be measured only up to $190V$ before micro discharges occurred (see Sec. 4.5.1), but has not at all reached saturation yet. Its value displayed in Fig. 5.19, which is the value at the largest measurable voltage, is therefore probably much lower than the real one at $350V$.

It can be clearly seen that the CCE is highest for $75\mu m$, followed by $100\mu m$, and lowest for $150\mu m$. This is as expected because the charge collection times are much lower for thinner detectors, on the one hand due to the higher electric field leading to a higher drift velocity and on the other hand simply because of the smaller drift distance.

Although there are sometimes small differences at a certain fluence between ST and DO material (which can be in some cases explained by the fact that the DO diodes are not yet fully depleted at $350V$ in contrast to the ST detectors, e.g. for $150\mu m$ and $100\mu m$ at $4 \times 10^{15} cm^{-2}$), no systematic effect can be observed. Thus, the difference in τ_{eff} between ST and DO as found in the last section cannot be confirmed and can probably be attributed to a statistical fluctuation. The CCE results rather confirm most of the previous measurements, which could not find material-related differences in trapping effects either. Therefore it is assumed that trapping of charge carriers in highly irradiated diodes is probably due to intrinsic Si defects and independent of impurities.

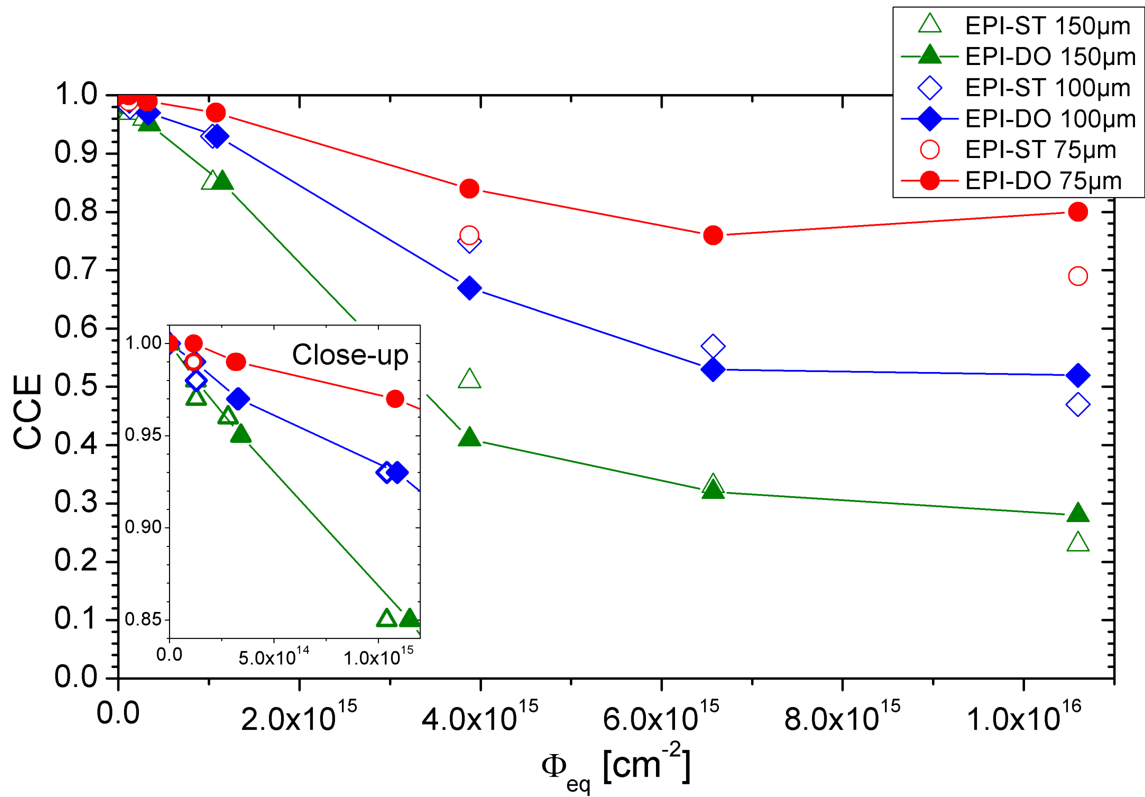

Figure 5.19: CCE at 350V where possible. If the measurements could not be done successfully up to 350V, the value at the highest measured voltage was taken.

5.4.3 Simulation of Charge Collection

It is very instructive to perform simulations that model the charge collection including trapping effects in an irradiated Si detector. On the one hand a comparison between measured and simulated data can reveal if all effects have been understood properly or if there are open questions. On the other hand a comparison or fitting of the calculated charge as a function of bias voltage to the measured curve with the trapping time constant as a free parameter could be another method to extract τ_{eff} without a time-resolved signal (see Sec. 5.4.1). Lastly, if a reliable simulation method is found, it will be possible to predict the charge collection properties for other fluences, devices and charge injection modes. This is important because in the frame of this work only simple test structures were studied and charge was only deposited by a laser or α-particles. However, what is interesting in the end is the collected charge created by a mip traversing a segmented detector that is irradiated up to high fluences. But segmented detectors behave differently compared to the here used simple pad diodes due to a more complex Ramo field. Thus, simulations are necessary to predict their performance with the help of the here found material properties.

Simulation Method

The basic mechanisms of signal formation and charge collection are described in Sec. 2.2.5. Combining Eq. 2.14 and Eq. 2.17 yields the following formula for the collected charge under

the influence of trapping if the original charge $Q_{0,x_0} = q_0 N_{0,x_0}$ is initially deposited at position x_0:

$$Q_{x_0} = \frac{Q_{0,x_0}}{d} \left[\int_{x_0}^{d} \exp\left(-\frac{t(x)}{\tau_{eff,e}}\right) dx - \int_{x_0}^{0} \exp\left(-\frac{t(x)}{\tau_{eff,h}}\right) dx \right]. \tag{5.11}$$

For the calculation of Q_{x_0} the knowledge of the inverse of the charge carrier trajectory according to Eq. 2.13 is required:

$$t(x) = \int_{x_0}^{x} \frac{1}{v_{dr}\left(E\left(x'\right)\right)} dx'. \tag{5.12}$$

Because of the electric field dependence of v_{dr} the collected charge is an implicit function of the applied bias voltage, i.e. $Q_{x_0} = Q_{x_0}(U)$. In order to calculate $t(x)$ both the electric field as a function of position inside the diode and the drift velocity as a function of electric field must be known. For the electric field $E(x)$ a linear model according to Eq. 2.6 was assumed. This formula is only valid for $U > U_{dep}$, but in the context of this work simulations were done only for depleted detectors anyway in order to avoid the peculiarities of diffusion and trapping in non-depleted regions. However, one has to emphasise that in reality significant deviations from the linear behaviour were observed, e.g. double peaks as pointed out in Sec. 5.4.1. But if the voltage is well above U_{dep} the linear assumption becomes much better (see Figs. 5.13/5.14).

If one assumes a constant drift velocity v_{dr}, Eq. 5.11 can be solved analytically as

$$Q_{x_0} = \frac{Q_{0,x_0}}{d} \left[v_{dr,e} \cdot \tau_{eff,e} \left(1 - \exp\left(-\frac{d - x_0}{v_{dr,e} \cdot \tau_{eff,e}}\right)\right) + v_{dr,h} \cdot \tau_{eff,h} \left(1 - \exp\left(-\frac{x_0}{v_{dr,h} \cdot \tau_{eff,h}}\right)\right) \right]. \tag{5.13}$$

However, this is a good approximation only in rare cases, e.g. if the field is high enough so that $v_{dr} \approx v_{sat}$. A common drift velocity parameterisation that interpolates between the linear low-field and the saturating high-field regime reads

$$v_{dr} = \frac{\mu_0 E}{\left(1 + \left(\frac{\mu_0 E}{v_{sat}}\right)^{\beta}\right)^{1/\beta}}, \tag{5.14}$$

where β is a free parameter that is sometimes set to 1 for a simpler approximation. The values for μ_0, v_{sat} and β are temperature-dependent and were taken from [Jac77][12]:

$$\begin{array}{rcllll}
\mu_{0,e} & = & 1.51 \times 10^9 \cdot T^{-2.42} \frac{cm^2}{Vs} & \Rightarrow & 1605.4 \frac{cm^2}{Vs} & \text{at } 294K \\
v_{sat,e} & = & 1.53 \times 10^9 \cdot T^{-0.87} \frac{cm}{s} & \Rightarrow & 1.09 \times 10^7 \frac{cm}{s} & \\
\beta_e & = & 2.57 \times 10^{-2} \cdot T^{0.66} & \Rightarrow & 1.09 & \\
 & & & & & \\
\mu_{0,h} & = & 1.31 \times 10^8 \cdot T^{-2.2} \frac{cm^2}{Vs} & \Rightarrow & 486.3 \frac{cm^2}{Vs} & \\
v_{sat,h} & = & 1.62 \times 10^8 \cdot T^{-0.52} \frac{cm}{s} & \Rightarrow & 0.84 \times 10^7 \frac{cm}{s} & \\
\beta_h & = & 0.46 \cdot T^{0.17} & \Rightarrow & 1.21 &
\end{array} \tag{5.15}$$

[12] In fact, [Jac77] uses another notation for the parameters. But the parameter E_C that is mentioned there transforms to the here used ones via $v_{sat} = \mu_0 E_C$.

T is the temperature in K. To be precise, these are the parameter values for the <111> crystal orientation. In [Can71] anisotropy effects were observed, which lead to a slightly lower electron drift velocity and a slightly higher hole drift velocity if the field is parallel to the <100> direction (depending on the electric field and temperature; at $300K$ maximum deviation of $\approx 15\%$). Unfortunately, a parameterisation in <100> direction has not been found in the literature. This means that only for the $75\mu m$ diodes the parameterisation is accurate. For the <100> oriented $100\mu m$ and $150\mu m$ detectors slight deviations have to be expected. If $\beta \neq 1$, Eq. 5.12 and Eq. 5.11 can only be solved numerically.

The simulation of the charge collection after front injection with a red laser is the easiest case because it can be assumed that all the charge is deposited at $x = 0$. Therefore on the one hand the hole contribution can be neglected and on the other hand Eq. 5.11 needs to be calculated only once for $x_0 = 0$.

If the charge is deposited continuously over a certain range inside the detector, which is the case for mips and α-particles, on the one hand the hole current has to be taken into account and on the other hand the total collected charge is given by the integral over the different deposition positions x_0:

$$Q_{total} = \int_0^d Q_{x_0} dx_0. \tag{5.16}$$

For the simulation this has been calculated numerically with a bin width of $1\mu m$. As initial charge distribution deposited by α-particles the SRIM results presented in Sec. 4.5.1 were used.

The charge collection efficiency can be calculated by

$$CCE = \frac{Q_{total}}{Q_{0,total}} \tag{5.17}$$

with $Q_{0,total} = \sum_{x_0} Q_{0,x_0}$ being the total deposited charge.

Simulation Results

With the simulation method presented above it was tried to reproduce the CCE as a function of bias voltage which was measured with α-particles and presented in Sec. 5.4.2. The used trapping time constants were calculated individually for each fluence with β_{lit} from Tab. 5.8. As the validity of $\beta_{e,lit}$ for EPI material has been confirmed experimentally by the CCM in this work (see Sec. 5.4.1), it is assumed that the use of $\beta_{h,lit}$ is also justified. Due to the limited penetration depth of α-particles, the influence of holes is only of minor importance anyway, especially in a $150\mu m$ detector. Thus, it is expected that the comparison between measured and simulated data offers a possibility to cross-check mainly the parameters of electron trapping.

Fig. 5.20 a) shows for the example of EPI-ST $150\mu m$ that the agreement between measurement and simulation is not very good. Although the simulation reproduces the trend that the CCE decreases with increasing fluence, it does not match the voltage-dependent behaviour well. Whereas for low fluences simulation and measurement seem to be similar at least near to the depletion voltage, this changes if going to higher voltages and to larger fluences. As already mentioned in Sec. 5.4.2 this can be explained for the very high fluences by the assumption of charge amplifying effects like avalanches. However the effect observed here is more

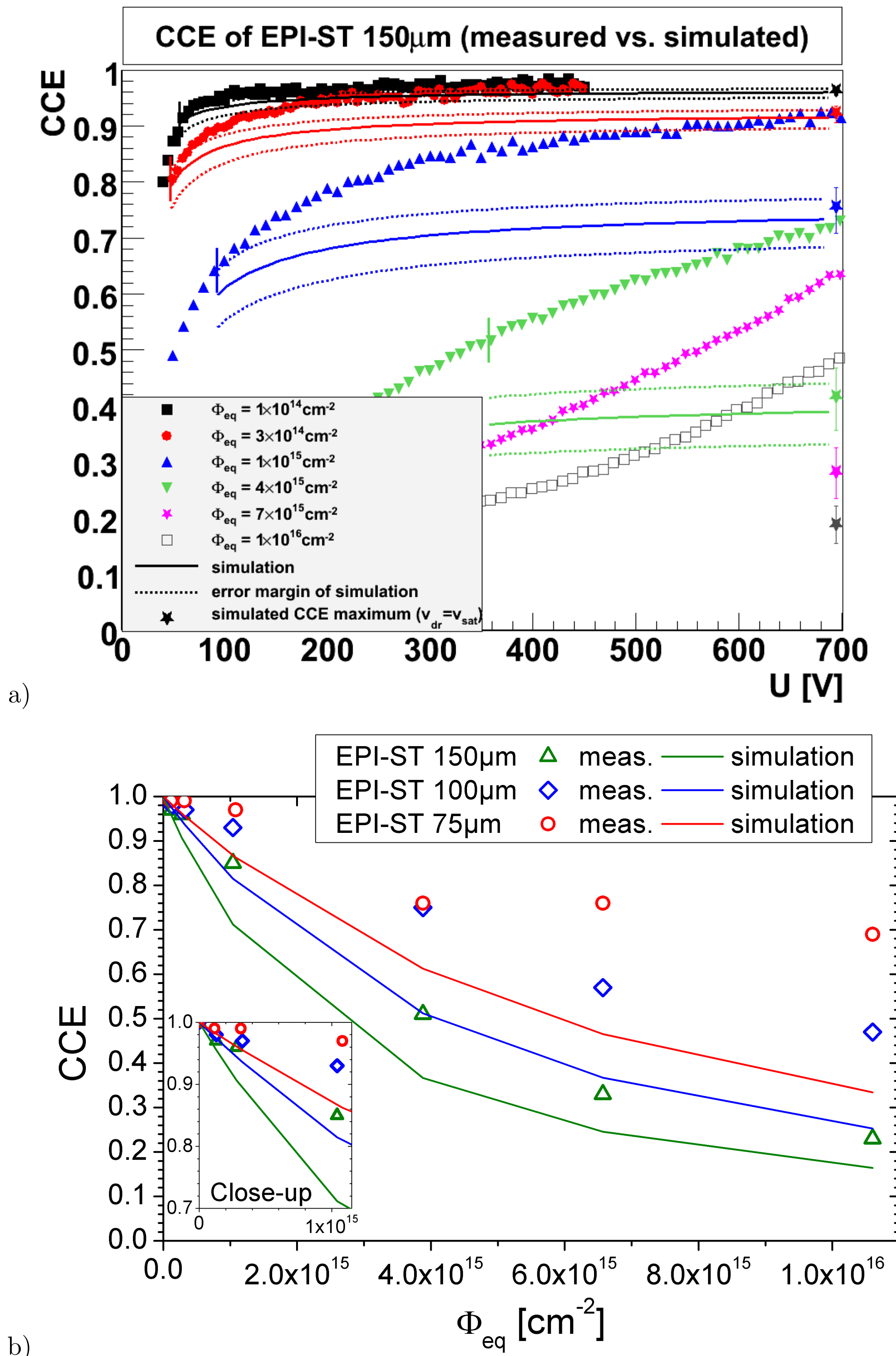

Figure 5.20: Comparison between the CCE as measured with α-particles and simulations. a) The CCE as a function of bias for EPI-ST 150μm. The error band of the simulation is due to a ±20% variation of τ_{eff}. The asterisk symbols on the right side indicate the simulated upper CCE limit for the respective fluence if $v_{dr} = v_{sat}$ is assumed. For the two highest fluences only this upper limit was calculated as the depletion voltage was unknown. b) The CCE at 350V as a function of fluence for EPI-ST at different thicknesses. For the two highest fluences the depletion voltage was not measurable and for a rough simulation set to 340V. In fact U_{dep} is expected to be higher than 350V so that the detectors are probably only partially depleted at that voltage, which would decrease the simulated CCE even more if considered.

general because also for low fluences at moderate voltages, where the electric field is unlikely to be strong enough for avalanche generation (average field at $150V$ is $< E >= 10^4 V cm^{-1}$), the measured CCE is found to be systematically higher than the simulated one.

It has to be admitted that especially Φ_{eq} has not been measured very accurately which implies also a large error for the calculated τ_{eff}, but it can be seen that allowing for a 20% error margin of τ_{eff} does not improve the situation. Variations in d and v_{dr} of 10%, which is highly over-estimated compared to the estimated error, have even less effect. One could also refer to the large model uncertainties of the simulation, which were already mentioned in the last section. Of course the linear-field assumption is only a first approximation, especially around the depletion voltage, but it should be acceptable for $U >> U_{dep}$. However, the quality of agreement between simulation and data is exactly the other way round. In order to check the influence of the drift velocity model, another parameterisation proposed by [Sel90] was tried, but the result was very similar to the one presented here. The fact that the simulation was done with a <111> drift velocity parameterisation for a <100> material cannot explain the discrepancy either. On the one hand the elctron drift velocity is lower in <100> material so that even more trapping would occur if taken into account. On the other hand, in the case of the <111> oriented $75\mu m$ thick material the simulation shows the same behaviour. Fig. 5.20 b) displays a comparison between simulated and measured CCE at $350V$ for different thicknesses.

In order to exclude all those model uncertainties as the reason for the discrepancy between simulation and measurement, the following argument is considered. The saturation drift velocity v_{sat} is the maximum velocity for charge carriers in a semiconductor. Therefore, independently of the assumed electric field model or the exact drift velocity description, there is a lower boundary for the charge collection time. Thus, assuming the charge carriers to travel with v_{sat} throughout the whole detector should give an upper limit for the CCE because in this case the least trapping occurs. This theoretical CCE maximum was calculated using Eq. 5.13 and added to Fig. 5.20 on the right side with error bars estimated from a 20% τ_{eff} variation. It can be seen that it does not improve the situation substantially.

Thus, the reason for the discrepancy has to be searched for rather in the fundamental description of trapping than in the charge transport model. It is doubtful that only one exponential term with a constant trapping time parameter as described by Eq. 2.17 can characterise all aspects of trapping well. On the one hand this formula was derived under the assumption $v_{dr} << v_{th}$ which might be violated for $v_{dr} \approx v_{sat}$. On the other hand Eq. 3.6, which relates the trapping probability to the microscopic defect properties and occupancy, contains several parameters that do not necessarily need to be constant. For example, in many other fields of physics the cross section σ is a function of velocity so that it would change with the electric field. Usually the cross section decreases as the velocity increases, which would lead to the observed reduction of trapping at high voltages. Furthermore, the occupation probability f_t might also vary. In fact, the occurrence of the double peak structure of the electric field in Sec. 5.4.1 has been explained by an inhomogeneous defect occupation density at high currents. It is reasonable to assume that such a trap filling will also affect, i.e. reduce, the trapping of signal charge carriers. Another reason for an enhanced CCE could be that detrapping effects take place already on such a short time scale.

In some cases it has been observed before that the simulated CCE underestimates the measured data systematically. For example in [Kra06] such a discrepancy was found for the CCE of neutron-irradiated diodes as measured with ^{90}Sr β-particles. Moreover, in [Bea99] it was also found impossible to obtain good fits with a constant trapping time to the CCE

obtained by both α- and β-TCT. They proposed to allow for a voltage-dependent trapping probability such that τ_{eff} increases linearly with increasing bias. As possible explanations for this phenomenon trap filling with increasing current and a velocity-dependent cross section were given. Indeed, Fig. 5.21 shows that with such an approach the measured data can be fitted well. For these fits a voltage-dependent

$$\tau_{eff,e} = \tau_0(U_{dep}) + \tau_1 \frac{(U - U_{dep})}{100V} \tag{5.18}$$

was assumed with the two fit parameters $\tau_0(U_{dep})$, i.e. the trapping time constant at depletion voltage, and τ_1, which is the change of $\tau_{eff,e}$ per $100V$. In order to keep the number of free fit parameters at a minimum, for the less important $\tau_{eff,h}$ the constant value as used before was taken and kept fixed. For the three lowest fluences of EPI-ST $150\mu m$ for which it is assumed that avalanche effects do not play a role, the following results were obtained:

$$\begin{array}{rclrclr} \tau_0(U_{dep}) & = & 22.5ns, & \tau_1 & = & 2.0ns & \text{for } 1 \times 10^{14} cm^{-2}, \\ \tau_0(U_{dep}) & = & 8.9ns, & \tau_1 & = & 4.0ns & \text{for } 3 \times 10^{14} cm^{-2}, \\ \tau_0(U_{dep}) & = & 2.4ns, & \tau_1 & = & 1.0ns & \text{for } 1 \times 10^{15} cm^{-2}. \end{array} \tag{5.19}$$

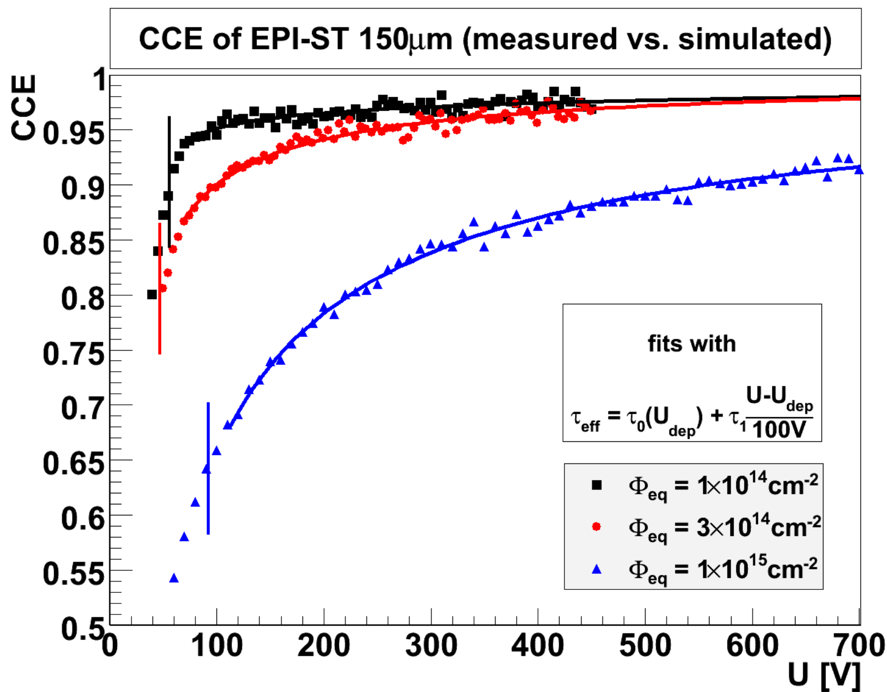

Figure 5.21: A fit to the CCE as measured with α-TCT for the three lowest fluences of EPI-ST $150\mu m$. A τ_{eff} depending linearly on the applied bias voltage was assumed.

In [Bro00], after presenting a newly found method that relies on the same trapping correction principles as the CCM, the authors of [Bea99] abandoned the idea of a voltage-dependent trapping time again. This was justified by referring to systematic effects related to the velocity - electric field parameterisation, deviations from the linear electric field or plasma effects[13]. However, the first two arguments were already ruled out in the discussion above and plasma

[13]One speaks of a *plasma* inside a semiconductor if the density of injected free charge carriers exceeds the space charge density locally so that the electric field is altered.

effects are not very convincing either. There are two contrary effects how a plasma could influence the trapping. On the one hand the carrier density might be so large that a local trap filling by a part of the charge prevents the remaining fraction from further capture. But on the other hand the enormous charge density significantly lowers the external electric field due to screening so that the charge collection is delayed, leading to enhanced trapping, which is believed to be the predominant effect. But also the fact that the fitting of $Q(U)$ after electron injection by red laser light failed and the above cited mismatching between simulation and data after β-particle penetration show that plasma effects cannot be the only reason because plasma is not expected to play a role in these cases.

Moreover, the fact that the CCM works in the case of assuming a uniform trapping time constant does not automatically exclude a variable trapping time because it was checked here that the CCM gives reasonable results also in the case of a voltage-dependent τ_{eff}. This was done by modifying the CCM in such a way that the measured current pulse shape was not corrected anymore with a uniform τ_{eff}, but with the voltage-dependent τ_{eff} from Eq. 5.18. In this first try, τ_1 was kept fixed with the fitting results from Eq. 5.19 in order to use the same evaluation procedure of the CCM as before, which works only if one parameter is varied. This method was applied to the pulse shapes of EPI-ST 150μm for $3 \times 10^{14} cm^{-2}$ and $1 \times 10^{15} cm^{-2}$. It turned out that also in this case of assuming a voltage-dependent τ_{eff} a flat slope of $Q(U)$ could be achieved for a certain $\tau_0(U_{dep})$. The extracted values for $\tau_0(U_{dep})$ agree within 30 % with the ones from Eq. 5.19.

It should be emphasised that the ideas presented here about a modified description of the trapping time are only first tentative considerations that were made in order to explain the mismatching between simulated and measured CCE. Especially the here considered model of a linear voltage-dependent trapping time is only a first ad-hoc parameterisation. In reality, a variable τ_{eff} would be probably not voltage- but rather electric-field or current-dependent. Moreover, it was only tested for a few special cases here. Unfortunately, it was not possible to study this phenomenon in more detail in the frame of this work. Further investigations in the future are highly desirable. Especially additional measurements with β-particles for the same diodes could be of interest. On the one hand, due to their different penetration behaviour the discrepancy between measured data and simulation could be tested independently, as well as the results obtained above with a voltage-dependent τ_{eff}. On the other hand, such measurements are needed in order to predict the total charge collection of a mip signal because, as it turned out here, simulations are not very reliable. Still, the question has to be answered which thickness will provide the largest total collected charge at high fluences. The investigations in this work clearly show that the charge collection efficiency is greatly improved by using a thinner material[14]. In this sense thin detectors are very radiaton hard also concerning trapping because a smaller fraction of the originally deposited charge is lost. But at the same time this initially deposited charge is also reduced if considering a mip because it is proportional to the thickness. Previous simulations and measurements have questioned whether the improvement in CCE at large fluences for thin diodes can completely compensate for the charge deposition loss [Kra06b], especially in segmented detectors, but it should be checked how it behaves for the thicknesses and high fluences investigated in this work.

[14]To be precise, one would expect a CCE value for mips that differs a bit from the one for α-particles due to the different penetration behaviour, but the thickness dependence should be the same.

Chapter 6

Summary and Conclusions

The aim of this work was the investigation of radiation damage in proton-irradiated epitaxial silicon diodes as a function of fluence, annealing time, thickness and impurity concentration. This was done in the framework of the international research collaboration RD50 that strives for the development of radiation hard detectors surviving at SLHC fluences of up to $1.6 \times 10^{16} cm^{-2}$. Pad diodes of $75 \mu m$, $100 \mu m$ and $150 \mu m$ thickness and of both standard and oxygen-enriched n-type material were studied. The initial doping concentration with phosphorus varied between $2.6 \times 10^{13} cm^{-3}$ for $75 \mu m$ and $8 \times 10^{12} cm^{-3}$ for $150 \mu m$ to realise a similar initial depletion voltage of about $100 - 150V$. The oxygen concentration of EPI-ST materials exhibited a clear inhomogeneity in SIMS measurements, its average value decreased from $9.3 \times 10^{16} cm^{-3}$ for $75 \mu m$ to $4.5 \times 10^{16} cm^{-3}$ for $150 \mu m$. Homogeneity was improved after oxygenation with increased concentration levels of $6 \times 10^{17} cm^{-3}$ for $75 \mu m$ and $1.4 \times 10^{17} cm^{-3}$ for $150 \mu m$. Irradiation was performed at CERN with $24 GeV/c$ protons in an equivalent fluence range between $10^{14} cm^{-2}$ and $10^{16} cm^{-2}$, which is expected at the SLHC. Isothermal annealing experiments were done at 80°C. The results that were obtained in this work will be summarised in the following.

CV/IV measurements

All samples were characterised by standard current-voltage and capacitance-voltage measurements at $10 kHz$ and room temperature. However, it turned out that these methods were limited at fluences above $4 \times 10^{15} cm^{-2}$ due to large reverse currents and the increase in depletion voltage leading to possible diode breakthrough.

The shape of the CV and IV characteristics differs between EPI-ST and EPI-DO material as for the first one, the slope of the curves is observed to be more inhomogeneous. This hints at a non-uniform N_{eff} distribution. Reasons could be a possible inhomogeneous defect distribution arising from non-uniform impurity concentrations and/or a non-constant defect occupation. This shows that the standard method of evaluating N_{eff} that is only based on U_{dep}, i.e. only on the kink of the curves at full depletion, is limited and probably not capable of describing all aspects of radiation damage in detail. Future investigations should try to develop methods that take into account the shape of the whole range of the CV curve. However, for an overview analysis the present-day approach is still considered to be a good approximation and was therefore used in this work.

Reverse Current

As in all investigations before, the volume-normalised reverse current was found to increase linearly with fluence, independently of the oxygen concentration and thickness. The overall current-related damage parameter after $8min$ annealing at 80°C was determined as $\alpha = (3.9 \pm 0.1) \times 10^{-17} Acm^{-1}$ if the less reliably measured data points at high fluences were excluded, which agrees very well with the reference value of $\alpha = 4.0 \times 10^{-17} Acm^{-1}$ found by [Mol99]. However, it turned out that the individual values scattered substantially around the mean value. As the current determination was considered to be accurately enough at low fluences and the fluence proportionality was expected to be reliable, this was explained by fluence fluctuations. Therefore, it was decided to correct the fluence determined by Al activation individually for each diode using the reference damage parameter α. For all following evaluations these so-called α-normalised values were taken, except for the highest measurable fluence of $4 \times 10^{15} cm^{-2}$.

The annealing behaviour of the reverse current showed the expected monotonic decrease. The $75\mu m$ diodes were annealed up to very long times so that their annealing curves with respect to the damage parameter α could be fitted with the model proposed by [Mol99], which is the sum of an exponential first-order decay, a constant and a logarithmic term. No difference between ST and DO material and between different fluences was found except at large fluences, which was explained by self-annealing effects and diode breakthrough. The results were similar to the ones of [Mol99] except for the time constant τ_1 that was found to be twice as high, but similar to the one of [Sch03]. However, due to the logarithmic term in the formula, the model was found to fail at very short and long annealing times. An alternative parameterisation consisting of the sum of two first-order and one second-order term was proposed and it was shown that it fits the data better, although a real second-order process would demand another behaviour of its time constant.

Depletion Voltage and Effective Doping Concentration

The U_{dep} annealing behaviour can be decomposed into a short-term annealing dominated by acceptor decay, a constant stable damage and a long-term annealing attributed to acceptor introduction. Therefore, the measured annealing curves, which were characterised by an increase in U_{dep} up to a maximum around $8min$ before decreasing again, indicated that no space charge sign inversion had occurred during irradiation for any of the investigated diodes up to fluences of $4 \times 10^{15} cm^{-2}$. To give a first estimate of the stable damage, the depletion voltages at $8min$, i.e. at the approximate maximum of the curves, were analysed as a function of fluence. All diodes showed a decrease of U_{dep} at low fluences, explained by donor removal, before rising again roughly linearly at larger fluence values, which was attributed to predominant donor introduction.

To analyse this in more detail, the values for ΔN_{eff} at $8min$, as calculated from the depletion voltage, were fitted with a function that describes incomplete donor removal and a fluence-proportional introduction of space charge. Too little data points in sensitive regions of the fit made a reliable quantitative determination of the fit parameters difficult, but the overall trend was clear: A negative value for g_C indicated predominant radiation-induced donor introduction, which was always higher for EPI-DO than for EPI-ST. This was explained by the involvement of oxygen in both the creation of shallow donors and the suppression of acceptor-like defects. The removal constant c was observed to decline with oxygen concentration, which

was ascribed to the suppression of VP formation, which is responsible for donor removal, by the competitive creation of VO. The donor removal was found to be incomplete with the removable fraction in the range between 56% and 88%. More intermediate data points will be provided by the upcoming irradiation campaign.

The big $75\mu m$ diodes were annealed up to long times and the time dependence of ΔN_{eff} could be fitted according to the Hamburg model with the sum of a first-order exponential decay describing the short-term annealing, a constant stable damage component and a long-term annealing part consisting of one first- and one second-order process. Due to seven free parameters the fit turned out to be unstable if no constraints were made. Self-annealing effects and type inversion during annealing introduced further difficulties for the highly irradiated diodes. At low fluences the short-term annealing time constant τ_A was found to be around $2min$ similarly to previous results, but its increase at higher fluences, which shifts the minimum in N_{eff} to later annealing times, is not yet understood. The fluence dependence of the stable damage component N_C was fitted with the same function as ΔN_{eff} at $8min$ and similar results were found. The long-term introduction rate g_Y, i.e. the linear slope of the total long-term annealing amplitude $N_{Y,total}$ as a function of fluence, was found to be positive reflecting acceptor introduction. The value for EPI-DO ($g_Y = 0.0564 \pm 0.0008$) was lower than for EPI-ST ($g_Y = 0.0638 \pm 0.0006$), which explains the fact that EPI-DO diodes type-invert later than EPI-ST ones. The fluence respectively concentration dependence of the time constants $\tau_{Y,1}$ and $\tau_{Y,2}$ confirm the assumption of a first- and second-order process, respectively.

Charge Collection and Trapping

A new TCT setup using a fast $670nm$ laser pulse, a $2.5GHz$ oscilloscope and small-area diodes with a reduced detector capacitance made the reduction of the measured signal rise time from $1.3ns$ to $0.6ns$ for $150\mu m$ diodes possible, which allowed time-resolved measurements of the electron current signal. Thus, the determination of the effective electron trapping time constant τ_{eff} using the charge correction method was possible and values very similar to those of FZ material were obtained. The trapping probability $\frac{1}{\tau_{eff}}$ was observed to increase linearly with fluence with the trapping-related damage parameter $\beta_e = (4.9 \pm 0.4) \times 10^{-16} cm^2 ns^{-1}$ at room temperature, which agrees very well with the results of [Kra01] for FZ diodes. If analysed separately, β_e was found to be around 25% lower for EPI-DO than for EPI-ST, but this can be a statistical fluctuation due to a large uncertainty of the method and a little amount of available data points.

The TCT pulse shapes confirmed that no space charge sign inversion had occurred during irradiation. The corrected shapes for highly irradiated EPI-ST diodes that might lead to a different conclusion are probably misleading due to corrections with trapping times in the same range as the signal rise time. At high fluences a double peak structure was observed, i.e. a deviation from the linear electric field due to the formation of a second junction at the back contact. This is an already well-known effect for other materials, which is explained by a non-uniform occupation of radiation-induced defects at high currents.

Charge collection efficiency measured with $5.8MeV$ α-particles showed an increase with voltage due to reduced trapping at higher drift velocities. Whereas the CCE of lower fluences exhibited an almost saturating behaviour, the CCE of highly irradiated diodes, which could only be measured under cooling, increased more rapidly at higher voltages, probably due to avalanche effects. At a fixed voltage the CCE was found to decrease as a function of fluence

due to enhanced radiation-induced introduction of trapping centres. The CCE of thinner diodes was always above the one of thicker material at the same fluence and voltage due to a reduced drift distance and a higher electric field. No significant difference between ST and DO material was found, which confirms previous observations and the assumption that trapping is related to intrinsic defects in Si.

Simulations systematically resulted in a significantly lower CCE than the measured data. Model uncertainties related to the drift velocity - electric field parameterisation and linear-field approximation could be excluded as the reason because also if $v_{dr} = v_{sat}$ is assumed throughout the whole detector, the findings remained unchanged. Plasma effects are unlikely and cannot be the only reason as similar problems have occurred in previous experiments with β-particles. It was found that a parameterisation assuming a voltage-dependent τ_{eff} as proposed by [Bea99] could fit the data curve well. Possible explanations include detrapping effects, a velocity-dependent cross section or trap filling at high currents so that in an improved model, τ_{eff} should be better parameterised as electric-field or current-dependent. A modified charge correction method worked also with a voltage-dependent τ_{eff}.

Conclusions

Epitaxial material again revealed a superior radiation tolerance after proton irradiation at high fluences. No type inversion took place during irradiation due to a high oxygen level. However, in contrast to thinner epitaxial diodes the medium thick ones investigated here could only be measured up to $4 \times 10^{15} cm^{-2}$ before the depletion voltage increased too much. It can be concluded that regarding the depletion voltage it is favourable to have a lowest possible thickness and a not too high oxygen concentration in EPI diodes, but one should consider that these two parameters are related to a certain extent.

A very interesting feature of EPI diodes, which could nevertheless allow the use of such medium thick detectors at highest fluences, is the alternating behaviour of donor introduction during irradiation contrasted to acceptor generation during long-term annealing. For the SLHC an operating scenario of cooling during run time on the one hand and room temperature storage during maintenance periods on the other hand might be found that keeps the depletion voltage at a moderate level during the whole operation period. A CERN scenario experiment to clarify this point would be desirable.

Concerning the reverse current and trapping, defect engineering has not provided a solution yet, probably because the responsible defects are intrinsic so that they do not depend on impurity concentrations. Further microscopic studies are needed to reveal the nature of these defects, which might lead the way to possible solutions. However, also these problems are mitigated in EPI material because the reverse current decreases and the CCE rises for thinner detectors. But it still needs to be clarified in further experiments if the total signal in the diodes investigated here is large enough at high fluences and not too much reduced due to less charge deposition by mips compared to thicker detectors.

In the end, the overall signal-to-noise ratio is the ultimate factor determining the operability. Epitaxial detectors of medium thickness are promising candidates for detectors keeping a manageable SNR up to highest fluences.

Appendix A

Investigated Detectors

Material/ Size	Device Label	$N_{eff,0}$ $[10^{12} cm^{-3}]$	d $[\mu m]$	Al activat. Φ_p $[10^{14} cm^{-2}]$	Al activat. Φ_{eq} $[10^{14} cm^{-2}]$	α-normal. Φ_{eq} $[10^{14} cm^{-2}]$	Investigation Methods
EPI-ST 150μm							
BIG 1	261636-13-25	8.8	148.6	unirrad.	-	-	CV/IV, α-TCT(RT,-10°C), L1-TCT
	261636-13-49	9.0	146.8	unirrad.	-	-	CV/IV, α-TCT(RT)
	261636-13-09	9.0	149.2	1.66	1.03	1.28	CV/IV, α-TCT(RT), L1-TCT
	261636-13-19	8.9	147.3	4.88	3.03	2.81	CV/IV, α-TCT(RT), L1-TCT
	261636-13-10	9.0	148.8	17.30	10.70	10.39	CV/IV, α-TCT(RT,-10°C), L1-TCT
	261636-13-58	8.8	146.2	62.50	38.80	-	CV/IV failed, α-TCT(-10°C)
	261636-13-08	9.1	149.0	106.00	65.70	-	CV/IV failed, α-TCT(-10°C)
	261636-13-11	9.1	147.8	171.00	106.00	-	CV/IV failed, α-TCT(-10°C)
BIG 2	261636-13-16	8.9	148.7	1.66	1.03	1.28	CV/IV
	261636-13-57	9.1	146.3	4.88	3.03	2.66	CV/IV
	261636-13-52	8.4	146.2	17.30	10.70	10.12	CV/IV
SMALL	261636-13-23-4			unirrad.	-	-	CV/IV, α-TCT(RT), L2-TCT
	261636-13-56-4	8.9	151.8	1.66	1.03	0.69	CV/IV, α-TCT(RT), L2-TCT
	261636-13-48-4	8.4	154.6	4.88	3.03	3.81	CV/IV, α-TCT(RT), L2-TCT
	261636-13-39-1	8.4	155.2	17.30	10.70	9.87	CV/IV, α-TCT(RT), L2-TCT
	261636-13-39-4	8.3	154.0	62.50	38.80	30.33	CV/IV, α-TCT(RT), L2-TCT
EPI-DO 150μm							
BIG 1	261636-9-36	7.9	150.8	unirrad.	-	-	CV/IV, α-TCT(RT)
	261636-9-51	7.7	150.8	unirrad.	-	-	CV/IV, α-TCT(RT,-10°C)
	261636-9-17	8.2	152.5	1.66	1.03	1.27	CV/IV, α-TCT(RT), L1-TCT
	261636-9-16	8.2	152.6	4.88	3.03	3.42	CV/IV, α-TCT(RT), L1-TCT
	261636-9-42	7.9	151.2	17.30	10.70	11.47	CV/IV, α-TCT(RT,-10°C), L1-TCT
	261636-9-07	8.7	151.5	62.50	38.80	-	CV/IV failed, α-TCT(-10°C)
	261636-9-44	7.7	150.6	106.00	65.70	-	CV/IV failed, α-TCT(-10°C)
	261636-9-18	8.2	152.0	171.00	106.00	-	CV/IV failed, α-TCT(-10°C)
BIG 2	261636-9-35	7.9	151.2	1.66	1.03	1.20	CV/IV
	261636-9-49	8.1	151.4	17.30	10.70	10.79	CV/IV
SMALL	261636-9-39-4			unirrad.	-	-	CV/IV, α-TCT(RT), L2-TCT
	261636-9-23-4	8.1	154.7	1.66	1.03	1.23	CV/IV, α-TCT(RT), L2-TCT
	261636-9-23-2	8.1	154.3	4.88	3.03	1.83	CV/IV, α-TCT(RT), L2-TCT
	261636-9-06-3	9.1	148.5	17.30	10.70	9.80	CV/IV, α-TCT(RT), L2-TCT
	261636-9-14-1	8.5	152.8	62.50	38.80	-	CV/IV failed, L2-TCT

Material/ Size	Device Label	$N_{eff,0}$ [$10^{12}cm^{-3}$]	d [μm]	Al activat. Φ_p [$10^{14}cm^{-2}$]	Al activat. Φ_{eq} [$10^{14}cm^{-2}$]	α-normal. Φ_{eq} [$10^{14}cm^{-2}$]	Investigation Methods
EPI-ST 100μm							
BIG	261636-5-25	15.0	102.8	unirrad.	-	-	CV/IV, α-TCT(RT,-10°C)
	261636-5-24	15.0	102.9	1.66	1.03	1.28	CV/IV, α-TCT(RT), L1-TCT
	261636-5-11	15.3	101.8	4.88	3.03	3.26	CV/IV, α-TCT(RT), L1-TCT
	261636-5-15	15.0	102.8	17.30	10.70	10.43	CV/IV, α-TCT(RT,-10°C), L1-TCT
	261636-5-42	15.0	101.6	62.50	38.80	40.27	CV/IV, α-TCT(RT,-10°C), L1-TCT
	261636-5-09	15.0	103.1	106.00	65.70	-	CV/IV failed, α-TCT(-10°C)
	261636-5-08	15.0	102.9	171.00	106.00	-	CV/IV failed, α-TCT(-10°C)
SMALL	261636-5-39-2	14.8	102.9	1.66	1.03	1.28	CV/IV
	261636-5-39-4	14.7	101.8	4.88	3.03	3.26	CV/IV
	261636-5-48-2	14.9	102.8	17.30	10.70	10.43	CV/IV
	261636-5-56-1	15.2	101.6	62.50	38.80	40.27	CV/IV
EPI-DO 100μm							
BIG	261636-1-35	14.9	99.3	unirrad.	-	-	CV/IV, α-TCT(RT,-10°C)
	261636-1-53	14.7	97.5	1.66	1.03	1.20	CV/IV, α-TCT(RT), L1-TCT
	261636-1-24	15.1	100.7	4.88	3.03	3.31	CV/IV, α-TCT(RT,-10°C), L1-TCT
	261636-1-40	15.1	99.8	17.30	10.70	10.86	CV/IV, α-TCT(RT,-10°C), L1-TCT
	261636-1-15	15.1	100.8	62.50	38.80	-	CV/IV failed, α-TCT(-10°C)
	261636-1-16	15.1	100.9	106.00	65.70	-	CV/IV failed, α-TCT(-10°C)
	261636-1-58	15.2	97.9	171.00	106.00	-	CV/IV failed, α-TCT(-10°C)
SMALL	261636-1-06-2	16.2	98.3	1.66	1.03	1.16	CV/IV
	261636-1-14-1	15.3	100.6	4.88	3.03	1.92	CV/IV
	261636-1-14-2	15.1	100.9	17.30	10.70	9.90	CV/IV
	261636-1-23-1	14.8	101.7	62.50	38.80	33.40	CV/IV
EPI-ST 75μm							
BIG	8364-03-53	25.8	74.5	unirrad.	-	-	CV/IV, α-TCT(RT,-10°C)
	8364-03-42	25.1	74.5	1.66	1.03	1.16	CV/IV, α-TCT(RT), L1-TCT
	8364-03-43	25.1	74.7	4.88	3.03	3.14	CV/IV, α-TCT(RT), L1-TCT
	8364-03-44	25.3	74.6	17.30	10.70	10.76	CV/IV, α-TCT(RT), L1-TCT
	8364-03-46	29.1	72.6	62.50	38.80	43.58	CV/IV, α-TCT(RT), L1-TCT
	8364-03-49	27.1	73.6	106.00	65.70	-	CV/IV failed, α-TCT(-10°C)
	8364-03-50	26.1	74.2	171.00	106.00	-	CV/IV failed, α-TCT(-10°C)
SMALL	8364-03-37-1	25.3	75.0	1.66	1.03	1.16	CV/IV
	8364-03-37-2	26.0	74.8	4.88	3.03	3.14	CV/IV
	8364-03-37-3	25.3	75.0	17.30	10.70	10.76	CV/IV
	8364-03-37-4	26.0	74.7	62.50	38.80	43.58	CV/IV
EPI-DO 75μm							
BIG	8364-07-25	24.6	71.1	unirrad.	-	-	CV/IV, α-TCT(RT,-10°C)
	8364-07-49	26.5	70.8	1.66	1.03	1.16	CV/IV, α-TCT(RT), L1-TCT
	8364-07-46	29.0	71.0	1.02	0.63	2.43	CV/IV, α-TCT(RT), L1-TCT
	8364-07-50	25.7	71.8	4.88	3.03	3.23	CV/IV, α-TCT(RT), L1-TCT
	8364-07-51	25.2	72.6	17.30	10.70	10.76	CV/IV, α-TCT(RT), L1-TCT
	8364-07-52	25.2	72.9	62.50	38.80	51.92	CV/IV, α-TCT(RT), L1-TCT
	8364-07-53	25.4	72.9	106.00	65.70	-	CV/IV failed, α-TCT(-10°C)
	8364-07-58	27.0	71.9	171.00	106.00	-	CV/IV failed, α-TCT(-10°C)
SMALL	8364-06-37-2	26.4	72.4	1.66	1.03	1.36	CV/IV
	8364-06-45-1	25.2	73.0	17.30	10.70	10.91	CV/IV
	8364-06-45-3	26.1	71.9	62.50	38.80	57.49	CV/IV

Table A.1: A list of the detectors investigated in this work. $N_{eff,0}$ is calculated from $U_{dep,0}$ and d from $C_{end,0}$. The proton fluence Φ_p is listed as measured by Al activation, the corresponding equivalent fluence Φ_{eq} was calculated using the hardness factor $\kappa = 0.62$. The α-normalised fluence shows the value re-determined via $\alpha = 4.0 \times 10^{-17} Acm^{-1}$ (see Sec. 5.2.1). Remarks concerning the investigation methods: *CV/IV failed* means that due to the measurement problems explained in Sec. 4.4 no U_{dep} and I_{dep} values could be obtained. The measurement temperature of TCT with α-particles is denoted in brackets (RT = room temperature). *L1-TCT* means TCT with 670nm laser light using the old setup, *L2-TCT* refers to measurements with the new setup (see Sec. 4.5.2).

List of Figures

1.1 Simulation of SLHC equivalent fluences as a function of beam line distance. . 2

2.1 Principle of a semiconductor detector. 5

2.2 Schematic figure of the formation of a p-n junction. 6

2.3 Schematic figure of a one-sided abrupt p^+-n junction. 7

3.1 Monte Carlo simulation of a cascade caused by a PKA. 14

3.2 Displacement energy cross section for different particle types. 15

3.3 Schematic representation of some point defects. 17

3.4 Effects of defect levels in the band gap on electrical properties. 17

4.1 Oxygen concentration depth profiles (SIMS measurements). 25

4.2 Schematic top view and cross section of the used pad diodes. 26

4.3 Equivalent circuit representing a reverse-biased detector. 27

4.4 CV and an IV characteristics and the determination of U_{dep} and I_{dep}. 29

4.5 a) TCT principle. b) Creation of e-h pairs as a function of detector depth for different TCT methods. 30

4.6 a) Electric field distribution. b) Electron TCT signal example. c) Hole TCT signal example. 31

4.7 α-TCT setup including a close-up of the detector mounting. 32

4.8 An example of an α-TCT signal. 33

4.9 The equivalent circuit of detector and TCT setup. 34

4.10 The new TCT setup with a 70ps laser, a $2.5GHz$ oscilloscope and a mounting for small diodes. 34

4.11 Comparison of 670nm laser-TCT signals taken with different setups for an unirradiated EPI-ST $150\mu m$ diode. 35

5.1 CV and IV characteristics for an EPI-ST and EPI-DO detector. 39

5.2 The reverse current normalised to the detector volume as a function of equivalent fluence after $8min$ annealing at 80°C. 40

5.3 The individual current damage parameter α as a function of Φ_{eq}. 41

5.4 Annealing behaviour of the normalised current I_{dep}/V at different fluences. . 42
5.5 Annealing behaviour of the current damage constant α for EPI-ST 75μm (a) and EPI-DO 75μm (b). 43
5.6 U_{dep} annealing curves at different fluences. 46
5.7 Depletion voltage after 8min at 80°C annealing. 47
5.8 The radiation-induced change in the effective doping concentration at 8min at 80°C as a function of fluence (corresponds approximately to the stable damage component). 49
5.9 The results from the fit to $\Delta N_{eff,C}(\Phi_{eq})$. 50
5.10 The ΔN_{eff} annealing curves for EPI-ST 75μm and EPI-DO 75μm. 52
5.11 Hamburg model fit results for EPI 75μm. 55
5.12 Extrapolation of depletion voltage up to $1.6 \times 10^{16} cm^{-2}$. 57
5.13 TCT current pulses as measured at room temperature after front injection with 670nm laser light for EPI-ST 150μm and EPI-DO 150μm without amplifier (30min at 80°C). 59
5.14 TCT current pulses corrected for trapping using $\tau = \tau_{eff,lit}$ according to [Kra01]. 60
5.15 The principle of the charge correction method. 61
5.16 The trapping probability $\frac{1}{\tau_{eff}}$ as a function of fluence. 63
5.17 Different CCE measurements for the same detector at different temperatures show both a good reproducibility and temperature independence. 65
5.18 CCE as a function of bias voltage as measured with α-TCT (big diodes). . . . 66
5.19 CCE at 350V. 68
5.20 Comparison between the CCE as measured with α-particles and simulations. 71
5.21 A fit to the CCE as measured with α-TCT for the three lowest fluences of EPI-ST 150μm. A τ_{eff} depending linearly on the applied bias voltage was assumed. 73

List of Tables

4.1 Properties of the used materials (average values). 24

4.2 The denoted proton fluence, the corresponding equivalent fluence, its simplified notation and irradiation duration. 27

5.1 The current damage parameter α after $8min$ annealing at 80°C for different materials and geometries. 42

5.2 Current annealing parameters extracted from the fit according to Eq. 5.1. . . 44

5.3 Current annealing parameters extracted from the fit according to Eq. 5.2. . . 45

5.4 The results from a weighted fit to $\Delta N_{eff,C}(\Phi_{eq})$. 50

5.5 Fit results of the annealing curves at 80°C for EPI-ST $75\mu m$ and EPI-DO $75\mu m$. 54

5.6 Stable damage parameters for EPI-ST $75\mu m$ and EPI-DO $75\mu m$. 54

5.7 The effective trapping time constant τ_{eff} as obtained with the CCM. 62

5.8 The trapping-related damage parameter β at room temperature. 63

A.1 A list of the detectors investigated in this work. 80

Bibliography

[Bea99] L. Beattie et al. *Carrier lifetimes in heavily irradiated silicon diodes.* Nuclear Instruments and Methods in Physics Research A 421 (1999), 502-511, 1999.

[Bro00] T.J. Brodbeck et al. *A new method of carrier trapping time measurement.* Nuclear Instruments and Methods in Physics Research A 455 (2000), 645-655, 2000.

[Can71] C. Canali et al. *Drift velocity of electrons and holes and associated anisotropic effects in silicon.* J. Phys. Chem. Solids Vol. 32, 1707-1720, 1971.

[CiS] CiS Institut für Mikrosensorik GmbH, Erfurt, Germany.

[Dab89] W. Dabrowski, K. Korbel. *Effects of deep imperfection levels on the capacitance of semiconductor detectors.* Nuclear Instruments and Methods in Physics Research A 276 (1989), 270-279, 1989.

[Dez97] B. Dezillie. *Radiation hardness studies of epitaxial silicon particle detectors for applications at the CERN Large Hadron Collider.* PhD thesis, University Joseph Fourier-Grenoble 1, 1997.

[Ere02] V. Eremin, E. Verbitskaya, Z. Li. *The origin of double peak electric field distribution in heavily irradiated silicon detectors.* Nuclear Instruments and Methods in Physics Research A 476 (2002), 556-564, 2002.

[Fre05] E. Fretwurst et. al. *Recent advancements in the development of radiation hard semiconductor detectors for S-LHC.* Nuclear Instruments and Methods in Physics Research, A 552 (2005), 7-19, 2005.

[Fre07] E. Fretwurst et al. *Radiation damage studies on MCz and standard and oxygen enriched epitaxial silicon devices.* Nuclear Instruments and Methods in Physics Research A 583 (2007), 58-63, 2007.

[Ger96] J. Gerhardt. *Charakterisierung strahleninduzierter Defekte in Silizium-Detektoren mit Hilfe des TCT-Verfahrens.* Diplomarbeit, Universität Hamburg, 1996.

[Gia02] F. Gianotti et al. *Physics potential and experimental challenges of the LHC luminosity upgrade.* CERN-TH/2002-078, hep-ph/02004087, April 2002.

[Gos59] B.R. Gossick. *Disordered Regions in Semiconductors Bombarded by Fast Neutrons.* J. Appl. Phys. Vol. 30, 1959.

[Hön03] F. Hönniger. *Strahlentoleranz von Cz-Silizium-Detektoren.* Diplomarbeit, Universität Hamburg, 2003.

[Huh02] M. Huhtinen. *Simulation of non-ionising energy loss an defect formation in silicon.* Nuclear Instruments and Methods in Physics Research, A 491 (2002), 194-215, 2002.

[ITME] Institute of Electronic Materials Technology (ITME), Warsaw, Poland.

[Jac77] C. Jacobini et al. *A review of some charge transport properties of silicon.* Solid-State Electronics, Vol. 20, 77-89, 1977.

[Jun07] A. Junkes. *Investigation of electrically active defects induced in silicon diodes after low doses of electron and neutron irradiation.* Diplomarbeit, Universität Hamburg, 2007.

[Koc07] K. Koch. *Strahlenhärte von epitaktischen, Floatzone- und MagneticCzochralski-Siliziumdioden nach Neutronenbestrahlung.* Diplomarbeit, Universität Hamburg, 2007.

[Kra01] G. Kramberger. *Signal development in irradiated silicon detectors.* Doctoral Thesis, University of Ljubljana, 2001.

[Kra03] G. Kramberger, D. Contarato, E. Fretwurst, F. Hönniger, G. Lindström, I. Pintilie, R. Röder, A. Schramm, J. Stahl. *Superior radiation tolerance of thin epitaxial silicon diodes.* Nuclear Instruments and Methods in Physics Research A 515 (2003), 665-670, 2003.

[Kra05] G. Kramberger, V. Cindro, I. Dolenc, E. Fretwurst, G. Lindström, I. Mandic, M. Mikuž, M. Zavrtanik. *Charge collection properties of heavily irradiated epitaxial silicon detectors.* Nuclear Instruments and Methods in Physics Research A 554 (2005), 212-219, 2005.

[Kra06] G. Kramberger. *Recent CCE measurements with neutron irradiated epi-Si pad detectors.* 8th RD50 Workshop, Prague, 27th June 2006.

[Kra06b] G. Kramberger, D. Contarato. *How to achieve highest charge collection efficiency in heavily irradiated position-sensitive silicon detector.* Nuclear Instruments and Methods in Physics Research A 560 (2006), 98-102, 2006.

[Kra07] G. Kramberger. *Recent results from CERN RD50 collaboration.* Nuclear Instruments and Methods in Physics Research A 583 (2007), 49-57, 2007.

[Krs04] Olaf Krasel. *Charge Collection in Irradiated Silicon-Detectors.* PhD Thesis, University of Dortmund, 2004.

[Laz87] M.S. Lazo, D.M. Woodall und P.J. McDaniel. *Silicon and silicon dioxide neutron damage functions.* In. Proc. Fast Burt React. Workshop, 1986, Sandia National Laboratories, 1987. [Tech.Rep.] SAND, SAND87-0098 Vol.1, 1987.

[Lin80] V.A.J. van Lint, T.M. Flanagan, R.E. Leadon, J.A. Naber, V.C. Rogers. *Mechanisms of Radiation Effects in Electronic Materials.* John Wiley & Sons, 1980.

[Lin06a] G. Lindström, E. Fretwurst, F. Hönniger, G. Kramberger, M. Möller-Ivens, I. Pintilie, A. Schramm. *Radiation tolerance of epitaxial silicon detectors at very large proton fluences.* Nuclear Instruments and Methods in Physics research, A 556 (2006), 451-458, 2006.

[Lin06b] G. Lindström, I. Dolenc, E. Fretwurst, F. Hönniger, G. Kramberger, M. Moll, E. Nossarzewska, I. Pintilie, R. Röder. *Epitaxial silicon detectors at extreme hadron fluences.* Nuclear Instruments and Methods in Physics research, A 568 (2006), 66-71, 2006.

[Lin06c] G. Lindström. *Radiation Tolerance of Silicon Detectors - The Challenge for Applications in Future High Energy Physics Experiments.* 1st WODEAN meetin, Hamburg, 24th August 2006.

[Mol95] M. Moll. *Temperungsexperimente an strahlengeschädigten Silizium-Detektoren.* Diplomarbeit, Universität Hamburg, 1995.

[Mol99] M. Moll. *Radiation Damage in Silicon Particle Detectors.* PhD Thesis, University of Hamburg, 1999.

[Pin03] I. Pintilie et al. *Second order generation of point defects in gamma-irradiated float-zone silicon, an explanation for type inversion.* Appl. Phys. Let. Vol. 82, 2003.

[Pin05] I. Pintilie, M. Buda, E. Fretwurst, F. Hönniger, G. Lindström, J. Stahl. *Radiation-induced donor generation in epitaxial and Cz diodes.* Nuclear Instruments and Methods in Physics Research A 552 (2005) 56-60, 2005.

[PIrS] M.Glaser. Online information about irradiation session P1-2007 available at http://irradiation.web.cern.ch/irradiation/Dosimeter/Set_P1_2007.htm .

[RD50] RD50 R&D Proposal. *DEVELOPMENT OF RADIATION HARD SEMICONDUCTOR DEVICES FOR VERY HIGH LUMINOSITY COLLIDERS.* CERN-LHCC 2002-003/P6, 15th February 2002.

[RD50-07] *RD50 Status Report 2007 - Radiation hard semiconductor devices for very high luminosity colliders.* CERN-LHCC-2008-001 and LHCC-RD-015, January 2008.

[Sch03] A. Schramm. *Strahlenhärte von epitaktischen Siliziumdetektoren.* Diplomarbeit, Universität Hamburg, 2003.

[Sel90] S. Selberherr et al. *The evolution of the MINIMOS mobility model.* Solid-State Electronics Vol. 33, No. 11, 1425-1436, 1990.

[Shi90] Y. Shi, D.X.Shen, F.M. Wu, K.J. Cheng. *A numerical study of cluster center formation in neutron-irradiated silicon.* J. Appl. Phys. Vol. 67, 1990.

[SIMS] SIMS laboratory. Physics Institute of the Polish Academy of Science, Warsaw, Poland.

[Smi83] L.S. Smirnow. *A survey of semiconductor radiation techniques.* MIR Publishers Moscow, 1983.

[SRIM] J.F. Ziegler. *SRIM-2008. The Stopping and Range of Ions in Matter.* 2008. www.srim.org .

[Sze85] S.M. Sze. *SEMICONDUCTOR DEVICES Physics and Technology.* John Wiley & Sons, 1985.

[Sze07] S.M. Sze, Kwok K. Ng. *Physics of semiconductor devices.* John Wiley & Sons, 3rd edition, 2007.

[Spi05] H. Spieler. *Semiconductor Detector Systems.* Oxford University Press, 2005.

[Sta04] J. Stahl. *Defect Characterization in High-Purity Silicon after γ- and Hadron Irradiation.* PhD Thesis, University of Hamburg, 2004.

[WODEAN] E. Fretwurst et al. *The WODEAN project - outline and present status.* 11th RD50 Workshop, CERN, 12th November 2007.

[Wun92] R. Wunstorf. *Systematische Untersuchung zur Strahlenresistenz von Silizium-Detektoren für die Verwendung in Hochenergiephysik-Experimenten.* Dissertation, Universität Hamburg, 1992.

Acknowledgements

I would like to thank everyone who contributed to this work and supported me during the last interesting, challenging, frustrating, rewarding and exciting year and beyond.

I am grateful to Prof. Dr. Robert Klanner for his friendly supervision of my work and his confidence. Also many thanks to Prof. Dr. Caren Hagner for giving the second reference.

I am deeply indebted to Dr. Eckhart Fretwurst who always supported me with amazing patience, kindliness and experienced advice and who was never bothered with my countless questions. I am also very thankful to Prof. Dr. Gunnar Lindström and Dr. Doris Eckstein for their numerous helpful comments, discussions and encouragement.

Special thanks to Peter Buhmann for a lot of useful help in the lab and with the measurements and for always good mood. Also to Uwe Pein for his support, and all the best for his health. I am as well grateful to Julian Becker for letting me touch his brand new Mercedes TCT and for the innumerable updates of the Labview programmes. Also many thanks to Alex Junkes for some figures, interesting talks and cheering me up.

Of course I wish to thank the whole group, it was a not only physics-related pleasure to work, talk and fight for the microwave with you, especially Marie Kristin Bock, Jörn Schwandt, Friederike Januschek, Hanno Perrey, Maike Tormählen, Ioana Pintilie, Volodymyr Khomenkov, Ajay Srivastava, Georg Steinbrück, Matthias Schröder, Sergei Bobrovskyi and Thorben Theed.

I am grateful to the RD50 collaboration for letting me participate in this exciting international research, especially to Maurice Glaser for performing the irradiation and to Gregor Kramberger for the ROOT files and his hospitality when I dropped by in Ljubljana.

I am happy about the experience with the Schülerlabor physik.begreifen team who showed me how great it is to share one's passion of physics, especially with children.

Natürlich möchte ich mich auch bei allen meinen Freunden bedanken für die Aufmunterung und die dringend notwendige Abwechslung mit erfrischend nicht-physikalischen Momenten (es waren wenige in den vergangenen Monaten, aber dafür umso wichtigere). Dafür bin ich besonders Norina, Friede, Steffen, Gosia, Sabine, Jan, Andy, Daniel und Moppel dankbar. Ich danke der europäischen Studentenorganisation AEGEE für grenzüberschreitende Erfahrungen und Freundschaft und dem CLUB feat. Yves für kulturelle Glanzpunkte, heimliche Hochzeiten und die Rettung des Regenwaldes.

Und zu guter Letzt möchte ich ganz besonders meiner Familie dafür danken, dass sie immer für mich da war, insbesondere meinen Eltern für grenzenlose Unterstützung während meines Studiums and mein Leben lang, meinen Großeltern sowie meiner Schwester Britta, meiner Tante Sigrid und meiner kleinen, langsam größer werdenden, Cousine Pia.

Hiermit versichere ich, dass ich diese Arbeit selbstständig verfasst und keine anderen als die angegebenen Quellen und Hilfsmittel verwendet habe. Mit einer späteren Ausleihe meiner Arbeit bin ich einverstanden.

Jörn Lange
Hamburg, den 1.10.2008